

## ABSTRACT

ZHU, PEI. From Liquid to Solid: Advanced Composite Separator/Electrolyte Structural Designs for High-Performance Lithium-Sulfur Batteries. (Under the direction of Dr. Xiangwu Zhang).

Elemental sulfur (S) has been considered as a promising cathode material for next-generation high-capacity lithium batteries because S is nontoxic and is abundant in the earth's crust. More importantly, S has a high theoretical capacity of 1675 mAh g<sup>-1</sup>, corresponding to a significantly increased energy density of 2567 Wh kg<sup>-1</sup> for lithium-sulfur (Li-S) batteries, which is almost one magnitude higher than that of the state-of-the-art lithium-ion batteries (LIBs). However, the insulating nature of S and the polysulfide shuttle effects in the S cathode, as well as the safety concerns of the lithium anode in liquid electrolytes are still the main challenges that limit the practical application of today's Li-S batteries.

To improve the electrochemical performance and enable safe operation, structural designs of S cathode are firstly carried out in liquid electrolyte Li-S batteries, where various materials including carbon-based materials, metal oxides and conducting polymers are intensively studied. With those efforts, the electrochemical performance of liquid electrolyte Li-S batteries could be largely improved to some extent with enhanced S utilization. However, it seems that it's still technically impossible to comprehensively avoid the polysulfide shuttle and, the safety problem originating from the flammable organic solvents in liquid electrolyte has not been solved.

Replacing the liquid electrolyte with solid electrolyte to develop all-solid-state Li-S batteries (ASSLSBs) provides "game-changing" opportunities for the realization of traditional liquid Li-S batteries as it can totally avoid the polysulfide shuttle and suppress the lithium dendrite formation. However, the reported electrochemical performance of ASSLSBs is still not comparable with the conventional liquid electrolyte Li-S cells in terms of S utilization and rate performance. Poor performance of ASSLSBs mainly comes from the challenges listed below: *i)*

slow Li ion diffusion and low ionic conductivity in solid electrolytes at room temperature; *ii*) ineffective contact and unstable solid-solid electrolyte/electrode interface.

In this dissertation, to address these challenges arisen from the traditional liquid electrolyte and solid electrolyte Li-S batteries, novel separators/electrolytes were designed and applied. Besides, the corresponding mechanisms of improved electrochemical performances were also studied and discussed.

For the liquid electrolyte Li-S batteries, studies were focused on the materials selection and novel structure designs of separators. We firstly selected reduced graphene oxide (rGO) as the polysulfide inhibitor and studied the different reduction degrees of rGOs on the electrochemical performance of Li-S batteries. Then we designed a novel bi-functional double-layer polyvinylidene fluoride (PVDF) based nanofiber membrane separator for Li-S batteries. The top rGO incorporated PVDF nanofiber layer with good electrical conductivity serves as the polysulfide inhibitor, while the porous PVDF nanofiber framework in both rGO-PVDF and PVDF layers keeps the structure integrity of the separator.

For the ASSLSBs, the studies were focused on the novel structural designs of solid electrolyte and S cathode. We firstly developed a one-dimensional (1D)  $\text{Li}_{0.33}\text{La}_{0.557}\text{TiO}_3$  (LLTO) ceramic nanofibers incorporated polyethylene oxide (PEO) based composite solid polymer electrolyte (PEO/LLTO) for ASSLSBs. The as-prepared PEO/LLTO electrolyte exhibited good mechanical strength, high ionic conductivity at room temperature ( $2.4 \times 10^{-4} \text{ S cm}^{-1}$ ), large electrochemical stability window (5 V vs. Li/Li<sup>+</sup>) and excellent lithium dendrite suppression. Then we integrated the composite solid polymer electrolyte with three-dimensional (3D) carbon nanofiber/S (CNF/S) cathode to obtain a novel bilayer framework with balanced electrical/ionic conductivity for room-temperature ASSLSBs. As a result of the benefits of the novel bilayer

structure design, the resultant ASSLSBs could deliver a stable cycling performance at room temperature with high Coulombic efficiency over 99%.

In summary, this dissertation provides a general strategy in dealing with the multiple challenges from both liquid and solid electrolyte Li-S batteries by structural designs of separators and electrolytes, which are necessary for the accelerated development of Li-S batteries in the field of research and industrialization.

© Copyright 2018 by Pei Zhu

All Rights Reserved

From Liquid to Solid: Advanced Composite Separator/Electrolyte Structural Designs for High-  
Performance Lithium-Sulfur Batteries

by  
Pei Zhu

A dissertation submitted to the Graduate Faculty of  
North Carolina State University  
in partial fulfillment of the  
requirements for the degree of  
Doctor of Philosophy

Fiber and Polymer Science

Raleigh, North Carolina

2018

APPROVED BY:

---

Dr. Xiangwu Zhang  
Committee Chair

---

Dr. Wei Gao

---

Dr. Philip D. Bradford

---

Dr. Veronica Augustyn

## **DEDICATION**

*To my beloved parents, brother and friends,*

*Without their continuous encouragement, this is impossible to be accomplished.*

*I appreciate to have you all in my life.*

## **BIOGRAPHY**

Pei Zhu was born in Wenling, Zhejiang Province, China. She received her Bachelor degree in Light-Chemical Engineering and Master degree in Textile Chemistry both from Zhejiang Sci-Tech University (China). Then she started to pursue her Ph.D. in Fiber and Polymer Science under the direction of Dr. Xiangwu Zhang at North Carolina State University in August 2015.

## ACKNOWLEDGMENTS

Here I would like to thank all of my committee members, Dr. Xiangwu Zhang, Dr. Wei Gao, Dr. Philip D. Bradford and Dr. Veronica Augustyn, for all the valuable advice and time to evaluate my work. In particular, I would like to express my sincerest gratitude to my advisor, Dr. Xiangwu Zhang, for his great mentorship and thoughtful insights during my Ph.D. study. This work would not have been possible without his endless encouragement and guidance.

I would also like to thank all of my co-authors and great lab members in Dr. Zhang's group, for their great help and advice.

Additionally, I also appreciate the help from Mr. Chuck Mooney, Dr. Yang Liu, Dr. Ching-Chang Chung, Mr. Fred Stevie in the Analytical Instrumentation Facility, and Ms. Judy D. Elson and Ms. Birgit Andersen in the College of Textiles at NC State University.

Moreover, I want to thank all of my friends for their encouragement during my Ph.D. study. Finally, and most importantly, I would like to express my special gratitude to my parents and my brother for their love and constant support.

## TABLE OF CONTENTS

LIST OF TABLES .....	x
LIST OF FIGURES .....	xi
<b>CHAPTER 1 OVERVIEW OF LITHIUM-SULFUR BATTERIES.....</b>	<b>1</b>
<b>1.1 Background and Operating Principles of Lithium-Sulfur Batteries .....</b>	<b>1</b>
<b>1.2 Challenges and System Limitations of Lithium-Sulfur Batteries.....</b>	<b>4</b>
1.2.1 Insulating Nature of Elemental Sulfur and its Discharge Products .....	4
1.2.2 Shuttling Effect of Discharge Intermediate – Polysulfides.....	5
1.2.3 Large Volume Change of Sulfur Cathode .....	5
1.2.4 Safety Issues.....	6
<b>1.3 Recent Advances in Separators of Traditional Liquid Lithium-Sulfur Batteries .....</b>	<b>6</b>
1.3.1 Modification of Traditional Separators.....	7
1.3.2 Novel Separators for Lithium-Sulfur Batteries .....	11
<b>1.4 Recent Development of All-Solid-State Lithium-Sulfur Batteries .....</b>	<b>17</b>
1.4.1 Solid Polymer Electrolytes for All-Solid-State Lithium-Sulfur Batteries .....	18
1.4.2 Solid State Electrolytes Enabled All-Solid-State Lithium-Sulfur Batteries .....	31
<b>CHAPTER 2 RESEARCH OBJECTIVES .....</b>	<b>35</b>
<b>2.1 Reduced Graphene Oxide Modified Glassfiber Separator for Li-S Batteries .....</b>	<b>35</b>
<b>2.2 A Novel Bi-functional Double Layer rGO-PVDF/PVDF Nanofiber Membrane for High-Performance Lithium-Sulfur Batteries .....</b>	<b>36</b>
<b>2.3 <math>\text{Li}_{0.33}\text{La}_{0.557}\text{TiO}_3</math> Ceramic Nanofiber-Enhanced Polyethylene Oxide-based Composite Polymer Electrolyte for All-Solid-State Lithium Batteries.....</b>	<b>36</b>

<b>2.4 Flexible Electrolyte-Cathode Bilayer Framework with Stabilized Interface for Room-Temperature All-Solid-State Lithium-Sulfur Batteries.....</b>	<b>37</b>
--	-----------

**CHAPTER 3 REDUCED GRAPHENE OXIDE MODIFIED GLASSFIBER**

<b>SEPARATOR FOR LITHIUM-SULFUR BATTERIES .....</b>	<b>39</b>
---	-----------

<b>3.1 Introduction.....</b>	<b>40</b>
------------------------------	-----------

<b>3.2 Experimental .....</b>	<b>43</b>
-------------------------------	-----------

3.2.1 Preparation of rGO Coated Separators .....	43
--	----

3.2.2 Structure Characterization .....	43
--	----

3.2.3 Electrode Fabrication and Cell Assembly.....	44
--	----

3.2.4 Electrochemical Performance Characterization.....	44
---	----

3.2.5 Polysulfide Diffusion Test .....	45
--	----

<b>3.3 Results and Discussion.....</b>	<b>45</b>
--	-----------

3.3.1 Morphology and Structure Characterization.....	45
--	----

3.3.2 Electrochemical Performance of Li-S Cells .....	49
---	----

3.3.3 Evaluation of Polysulfides Rejection.....	59
---	----

<b>3.4 Conclusion .....</b>	<b>62</b>
-----------------------------	-----------

**CHAPTER 4 A NOVEL BI-FUNCTIONAL DOUBLE-LAYER rGO-PVDF/PVDF**

**NANOFIBER MEMBRANE FOR HIGH-PERFORMANCE LITHIUM-SULFUR**

<b>BATTERIES. ....</b>	<b>63</b>
------------------------	-----------

<b>4.1 Introduction.....</b>	<b>64</b>
------------------------------	-----------

<b>4.2 Experimental .....</b>	<b>67</b>
-------------------------------	-----------

4.2.1 Membrane Preparation.....	67
---------------------------------	----

4.2.2 Membrane Structure Characterization .....	68
4.2.3 Thermal Performance Evaluation .....	69
4.2.4 Sulfur Electrode Fabrication and Cell Assembly.....	69
4.2.5 Electrochemical performance characterization .....	70
<b>4.3 Results and Discussion.....</b>	<b>71</b>
4.3.1 Morphology and Structure Characterization.....	71
4.3.2 Thermal Stability Measurement.....	79
4.3.3 Electrochemical Evaluation .....	80
4.3.4 Lithium Ion Diffusion Coefficients .....	85
4.3.4 Rate Capabilities and Cycle Performance.....	87
4.3.5 Evaluation of polysulfide Rejection-Surface Morphology of Cycled Separators/ Li Metal Anode and EIS Curves .....	90
<b>4.4 Conclusion .....</b>	<b>96</b>
 <b>CHAPTER 5 <math>\text{Li}_{0.33}\text{La}_{0.557}\text{TiO}_3</math> CERAMIC NANOFIBER-ENHANCED</b>	
<b>POLY(ETHYLENE OXIDE)-BASED COMPOSITE POLYMER ELECTROLYTE</b>	
<b>FOR ALL-SOLID-STATE LITHIUM BATTERIES .....</b>	
<b>5.1 Introduction.....</b>	<b>98</b>
<b>5.2 Experimental .....</b>	<b>101</b>
5.2.1 Synthesis of LLTO Nanofibers .....	101
5.2.2 Synthesis of LLTO nanofiber filled solid composite polymer electrolyte. ....	101
5.2.3 Structure Characterization .....	102
5.2.4 Electrochemical performance characterization .....	102

<b>5.3 Results and Discussion.....</b>	<b>104</b>
5.3.1 Morphology and Structure Characterization of LLTO Nanofibers .....	104
5.3.2 Preparation and Characterization of Solid Composite Electrolyte. ....	109
5.3.3 Ionic Conductivity Measurement of Solid Composite Electrolyte.. ....	114
5.3.4 Activation Energy Calculation.....	118
5.3.5 Electrochemical Stability Window .....	119
5.3.6 Voltage Profiles of Symmetric Li Cell .....	120
<b>5.4 Conclusion .....</b>	<b>122</b>
 <b>CHAPTER 6 FEXIBLE ELECTROLYTE-CATHODE BILAYER FRAMEWORK WITH STABILIZED INTERFACE FOR ROOM-TEMPERATURE ALL-SOLID- STATE LITHIUM-SULFUR BATTERIES .....</b>	 <b>123</b>
<b>6.1 Introduction.....</b>	<b>125</b>
<b>6.2 Experimental .....</b>	<b>128</b>
6.2.1 PEO/LLTO solid electrolyte preparation.....	128
6.2.2 CNF/S-PEO/LLTO Bilayer Framework Preparation.....	128
6.2.3 Structure Characterization .....	129
6.2.4 Electrochemcial Characterization .....	130
<b>6.3 Results and Disscussion .....</b>	<b>131</b>
6.3.1 Fabrication and Characterization of Novel CNF/S-PEO/LLTO Bilayer Structure ...	131
6.3.2 Interfacial Stability of PEO/LLTO Solid Polymer Electrolyte/Li Metal .....	143
6.3.3 Electrochemical Performance of ASSLSBs with CNF/S-PEO/LLTO .....	147
<b>6.4 Conclusion .....</b>	<b>150</b>

**CHAPTER 7 RECOMMENDED FUTURE WORK ..... 151**

**REFERENCES..... 153**

## LIST OF TABLES

<b>Table 3-1</b> Elemental Analysis of rGO-1 and rGO-2. ....	46
<b>Table 4-1</b> Porosity and electrolyte uptake parameters for PP, PVDF, rGO-PVDF/PVDF-1 and rGO-PVDF/PVDF-2 separators. ....	75
<b>Table 4-2</b> Elemental analysis and electrical conductivity results of rGO. ....	78
<b>Table 5-1</b> Comparison between our research and the reported work in literature. ....	113
<b>Table 5-2</b> Activation energies of solid composite electrolytes with different LLTO concentrations below 60 °C. ....	118

## LIST OF FIGURES

<b>Figure 1.1</b>	A typical structure of Li-S batteries. ....	3
<b>Figure 1.2</b>	Voltage profiles of Li-S cell. <sup>1</sup> .....	4
<b>Figure 1.3</b>	(a) Schematic configuration of Li-S cells with coated PP separators. Photographs of (b) bare PP separator and (c) super P coated separator. SEM images of (d) pristine separator and (e) super P coated separator. <sup>14</sup> .....	9
<b>Figure 1.4</b>	Cycling performance of Li-S cells with different materials coating on separators. <sup>14</sup> .	9
<b>Figure 1.5</b>	Schematic configurations of different Li-S batteries. <sup>16</sup> .....	10
<b>Figure 1.6</b>	Cycling performance of Li-S cell with ion-selective membrane. <sup>16</sup> .....	11
<b>Figure 1.7</b>	(a) Schematic cell configuration of Li-S cell with hybrid separator. (b) Cycling performance of Li-S cell with the hybrid separators. <sup>17-18</sup> .....	13
<b>Figure 1.8</b>	Schematic illustration of Li-S cell with (a) PP and (b) GF separator, showing the excellent ability of GF in blocking polysulfides. (c) Rate capabilities of Li-S cell with GF separator. <sup>19</sup> .....	14
<b>Figure 1.9</b>	Schematic illustration of the Li-S cell with PAN/GO separator. <sup>24</sup> .....	16
<b>Figure 1.10</b>	Schematic illustration of polyoxazole nanofiber membrane. <sup>25</sup> .....	17
<b>Figure 1.11</b>	Chemical structures of extensively studied polymers for solid electrolytes. <sup>31</sup> .....	20
<b>Figure 1.12</b>	(a) Li ion motion in a PEO polymer host. (b) Mechanisms of Li-ion transfer in crystalline domains of polymer matrix. <sup>37-38</sup> .....	21
<b>Figure 1.13</b>	Schematic model of these two liquids in PEO/PMMA electrolyte system. <sup>41</sup> .....	25
<b>Figure 1.14</b>	Chemical structure of triblock copolymer of P(STFSILi)-PEO-P(STFSILi). <sup>42</sup> .....	26
<b>Figure 1.15</b>	(a) Plots of conductivity at various temperatures of several P(STFSILi)-PEO- P(STFSILi). (b) Mechanical performance of copolymer P(STFSILi)-PEO-	

P(STFSILi) with 31% P(STFSILi) at 40 °C. (c) Electrochemical stability window tested at 80 °C. <sup>42</sup> .....	27
<b>Figure 1.16</b> Chemical structure of crosslinked PE/PEO electrolyte with the LiTFSI salt. <sup>43</sup> .....	28
<b>Figure 1.17</b> Schematic illustration of the procedure of in-situ synthesis and the interaction mechanisms between SiO <sub>2</sub> nanoparticles and PEO chains. <sup>50</sup> .....	30
<b>Figure 1.18</b> Schematic of 3D LLZO/PEO solid composite electrolyte. <sup>32</sup> .....	31
<b>Figure 1.19</b> Schematic illustration of the one-pot synthesis of the mixed conducting Li <sub>2</sub> S cathode. <sup>27</sup> .....	34
<b>Figure 3.1</b> Plain-view SEM images and corresponding C and O mapping of (a, c, e) GF/rGO-1, and (b, d, f) GF/rGO-2 separators. Cross-sectional SEM images of (g) GF/rGO-1, (h) GF/rGO-2 separators. ....	47
<b>Figure 3.2</b> (a) XRD patterns and (b) N <sub>2</sub> isothermal adsorption curves of rGO-1 and rGO-2. XPS spectra of (c) rGO-1 and (d) rGO-2.....	49
<b>Figure 3.3</b> (a) EIS curves of fresh Li-S cells with GF, GF/rGO-1 and GF/rGO-2 separators. CV curves of Li-S cells with (b) GF, (c) GF/rGO-1 and (d) GF/rGO-2 separators at a scan rate of 0.1 mV s <sup>-1</sup> .....	51
<b>Figure 3.4</b> Discharge-charge profiles of Li-S cells with (a) GF, (b) GF/rGO-1 and (c) GF/rGO-2 separators tested with electrolyte without the LiNO <sub>3</sub> additive.....	53
<b>Figure 3.5</b> (a) Cycle performance of Li-S cells with GF, GF/rGO-1 and GF/rGO-2 separators tested with electrolyte without LiNO <sub>3</sub> additive, (b) Coulombic efficiencies of Li-S cells with GF, GF/rGO-1 and GF/rGO-2 separators tested with/without the LiNO <sub>3</sub> additive. ....	55

<b>Figure 3.6</b> (a) Cycling performance of the Li-S cells with GF, GF/rGO-1 and GF/rGO-2 separators with LiNO <sub>3</sub> additive at current density of 0.2C. (b) Rate capabilities of the Li-S cells with GF, GF/rGO-1 and GF/rGO-2 separators with LiNO <sub>3</sub> additive.....	58
<b>Figure 3.7</b> SEM images of the cycled separators towards Li anode: (a) GF, (b) GF/rGO-1, (c) GF/rGO-2. Corresponding S mapping (d, e, f) of (a), (b) and (c), respectively.....	60
<b>Figure 3.8</b> Photo images of (a) blank electrolyte and (b) polysulfide diffusion model with GF, GF/rGO-1 and GF/rGO-2 separators after 30 min. ....	61
<b>Figure 4.1</b> SEM images of (a, b) PP membrane, (c, d) PVDF nanofiber membrane, (e) rGO-PVDF nanofiber composite membrane, and (f) rGO powder. ....	72
<b>Figure 4.2</b> Cross-sectional FESEM images of double-layer rGO-PVDF/PVDF separators with clear demonstration of rGO-PVDF and PVDF membrane layers: (a) rGO-PVDF/PVDF-1; (b) rGO-PVDF/PVDF-2. ....	74
<b>Figure 4.3</b> (a) Nitrogen adsorption-desorption isotherms of rGO powders. (b) BJH pore-size distributions of rGO powders. ....	75
<b>Figure 4.4</b> (a) XRD patterns and (b) FTIR spectra of the rGO powder, and PVDF, rGO-PVDF/PVDF-1 and rGO-PVDF/PVDF-2 nanofiber separators. ....	77
<b>Figure 4.5</b> Photographs of PP, PVDF, rGO-PVDF/PVDF-1 and rGO-PVDF/PVDF-2 separators (a) before and (b) after thermal treatment (dried after thermal treatment in liquid electrolyte at 80 °C for 24 h).....	79
<b>Figure 4.6</b> Nyquist plots of Li-S cells with PP, PVDF, rGO-PVDF/PVDF-1 and rGO-PVDF/PVDF-2 separators before cycling. ....	80

<b>Figure 4.7</b> Galvanic discharge-charge curves of Li-S cells with (a) PP, (b) PVDF, (c) rGO-PVDF/PVDF-1 and (d) rGO-PVDF/PVDF-2 separators. (e) Schematic illustration of bifunctional double-layer rGO-PVDF/PVDF membrane separator. ....	81
<b>Figure 4.8</b> CV curves of Li-S cells with (a) PP, (b) PVDF, (c) rGO-PVDF/PVDF-1 and (d) rGO-PVDF/PVDF-2 separators. ....	83
<b>Figure 4.9</b> CV curves at scan rates of 0.1, 0.2 and 0.3 mV s <sup>-1</sup> of Li-S cells with (a) PP, (b) PVDF, (c) rGO-PVDF/PVDF-1 and (d) rGO-PVDF/PVDF-2 separators. ....	84
<b>Figure 4.10</b> Plots of CV peak currents: peak A refers to the cathode reaction of S <sub>8</sub> to Li <sub>2</sub> S <sub>4</sub> ; peak B refers to the cathodic reaction of Li <sub>2</sub> S <sub>4</sub> to Li <sub>2</sub> S; and peak C refers to the anodic reaction of Li <sub>2</sub> S to S <sub>8</sub> . ....	86
<b>Figure 4.11</b> (a) Rate capabilities of Li-S cells with PP, PVDF, rGO-PVDF/PVDF-1 and rGO-PVDF/PVDF-2 separators at current densities of 0.2C, 0.5C, 1C, 2C and 0.2C, respectively. (b) Cycling performance of Li-S cells with PP, PVDF, rGO-PVDF/PVDF-1 and rGO-PVDF/PVDF-2. ....	89
<b>Figure 4.12</b> SEM images of (a, c) PP and (b, d) rGO-PVDF/PVDF-2 separators towards Li metal side after 200 cycles at 1C, and (e, f) corresponding S mappings of (a) and (b), respectively. ....	91
<b>Figure 4.13</b> SEM images of (a) PP and (b) rGO-PVDF/PVDF-2 separators towards Li metal side after 100 cycles at 1C. ....	92
<b>Figure 4.14</b> SEM images of Li metal anode surface with (a) PP and (b) rGO-PVDF/PVDF-2 separators after 200 cycles at 1C, (c, d) corresponding S mapping of (a, b), respectively. ....	93

<b>Figure 4.15</b> Nyquist plots of Li-S cells with PP and rGO-PVDF/PVDF-2 separators before and after 200 cycles at 1C.....	95
<b>Figure 5.1</b> SEM images of as-spun precursor nanofibers (a), LLTO nanofibers after calcination at (b) 700 °C, (c) 800 °C and (d) 900 °C for 2h. ....	105
<b>Figure 5.2</b> Diameter distributions and average diameters of (a) as-spun precursor nanofibers, (b) LLTO nanofibers calcined at 700 °C for 2h and (c) LLTO nanofibers calcined at 800 °C for 2h, and (d) LLTO nanofibers calcined at 900°C for 2h. ....	106
<b>Figure 5.3</b> (a) TGA curves of as-spun precursor nanofibers. (b) XRD patterns of the LLTO nanofibers calcined at 700, 800 and 900 °C for 2h.....	107
<b>Figure 5.4</b> (a, b) TEM images of LLTO nanofibers (800 °C) in different magnifications. (c) Corresponding selected area electron diffraction (SAED) patterns. (d) High-resolution TEM (HRTEM) image of an individual LLTO nanofiber.....	109
<b>Figure 5.5</b> (a) EIS curve of LLTO plate at room temperature. (b) XRD patterns of the PEO/LiTFSI/LLTO solid composite electrolytes with different LLTO nanofiber contents. (c) XRD patterns of the PEO/LiTFSI/LLTO solid composite electrolytes without and with 15 wt.% LLTO nanofiber/particle, showing the influence of LLTO morphology on the crystalline phase of PEO. ....	111
<b>Figure 5.6</b> SEM images of (a) PEO/LiTFSI, (b) PEO/LiTFSI/LLTO 10 wt.%, (c) PEO/LiTFSI/LLTO 15 wt.%, and (d) PEO/LiTFSI/LLTO 20 wt.% solid electrolytes... ..	112
<b>Figure 5.7</b> (a) EIS results of the PEO/LiTFSI/LLTO solid composite electrolytes with different LLTO nanofiber contents at room temperature (Inset is the individual EIS figure for the PEO/LiTFSI/LLTO 15%). (b) Ionic conductivities of the	

PEO/LiTFSI/LLTO solid composite electrolytes with different LLTO nanofiber contents at room temperature. ....	116
<b>Figure 5.8</b> (a) Arrhenius plots of the PEO/LiTFSI/LLTO solid composite electrolytes with different LLTO contents. (b) EIS result of the PEO/LiTFSI/LLTO particle solid composite electrolyte with 15% LLTO particles at room temperature. (c) Arrhenius plot of the PEO/LiTFSI/LLTO particle solid composite electrolyte with 15% LLTO particles. ....	117
<b>Figure 5.9</b> Linear Sweep voltammetry curve of PEO/LiTFSI and PEO/LiTFSI/LLTO 15 wt.% solid composite electrolytes. ....	120
<b>Figure 5.10</b> Voltage profile of the continued lithium plating/stripping cycling of PEO/LiTFSI/LLTO 15 wt.% solid electrolyte tested at a current density of 0.5 mA cm <sup>-2</sup> at 25 °C (Insert: voltage profiles of PEO/LiTFSI/LLTO 15 wt.% solid electrolyte tested at 710 - 720 h). ....	121
<b>Figure 6.1</b> Schematic illustration of the novel 1D LLTO nanofiber enhanced composite CNF/S-PEO/LLTO cathode structure design: the top thin PEO/LLTO solid polymer electrolyte layer acts as the Li ion conductor that ensures the fast facial ion transport between cathode and anode while the incorporation of ceramic LLTO also improves the interfacial stability; the bottom PEO filled 3D CNF/S layer with intimate triple-phase contact of electrical conductive current collector (CNF), active material (S) and solid polymer electrolyte (PEO) provides a balanced dual-conductive architecture for continuous electron/ion transfer. The entire bi-layer structure can be placed on the top of the anode surface to form a full Li-S cell without the use of additional electrolyte or separator layer. ....	131

<b>Figure 6.2</b> (a) SEM image of CNFs. Diameter distributions and average fiber diameters of (b) CNFs and (c) CNF/S.....	133
<b>Figure 6.3</b> N <sub>2</sub> isothermal adsorption curves of CNF (inserted: corresponding pore size distribution curve).....	134
<b>Figure 6.4</b> SEM images of (a) CNF/S, (b) PEO/LLTO solid polymer electrolyte. (c) High resolution SEM image of PEO/LLTO solid polymer electrolyte with clearly seen LLTO structure. ....	135
<b>Figure 6.5</b> Cross-sectional SEM images of (d) CNF/S-PEO/LLTO bilayer framework and (e) high magnification bilayer framework with clearly seen PEO/LLTO solid polymer electrolyte (thickness of 15 ± 5 μm). (f) Stress-strain curves of CNF, CNF-PEO and CNF-PEO/LLTO (inserted: photo images of CNF/S-PEO/LLTO electrode with bended structure, showing good flexibility) and (g) EDS mapping of the cross-section of CNF/S-PEO/LLTO bi-layer framework (e). .....	137
<b>Figure 6.6</b> (a) HRTEM image of single CNF, (b) CNF/S, (c) CNF/S-PEO/LLTO (LLTO nanofiber attached on PEO coated CNF/S) and (d) LLTO nanofibers with a lattice spacing of 0.27 nm. ....	138
<b>Figure 6.7</b> (a) STEM images of one representative CNF/S-PEO/LLTO nanofiber and corresponding elemental mapping of (b) C, (c) S, (d) O, (e) Ti and (f) La. ....	139
<b>Figure 6.8</b> (a) XRD patterns of CNFs, CNF/S and CNF/S-PEO/LLTO. (b) DSC curves of PEO and PEO/LLTO solid electrolytes.....	141
<b>Figure 6.9</b> (a) EIS results of PEO and PEO/LLTO solid polymer electrolytes tested at room temperature. (b) Arrhenius plots of PEO and PEO/LLTO solid electrolytes. (c) Electrochemical stability window of PEO/LLTO solid electrolyte. ....	143

**Figure 6.10** Voltage profiles of Li plating/stripping cycling with a current density of 0.5 mA cm<sup>-2</sup> at RT (inserted: voltage profiles of PEO and PEO/LLTO tested at 201-203 cycles-left; voltage profile of PEO/LLTO at 990-1000 cycles-right) ..... 145

**Figure 6.11** SEM images of the surface of Li anodes from symmetric Li cells, (a) Li/PEO/Li and (b) Li/(PEO/LLTO)/Li, after 1000 h testing at a current density of 0.5 mA cm<sup>-2</sup> at room temperature. .... 146

**Figure 6.12** (a) Cycling performance of ASSLSBs with CNF/S-PEO/LLTO electrode tested at 0.05 C with a sulfur loading of 1.27 mg cm<sup>-2</sup>. (b) Charge/discharge curves and (c) rate capabilities of cell with CNF/S-PEO/LLTO tested at various current densities ..... 148

## CHAPTER 1            OVERVIEW OF LITHIUM-SULFUR BATTERIES

### 1.1 Background and Operating Principles of Lithium-Sulfur Batteries

The increasing use of fossil fuels has inevitably caused environmental pollution issues. People are trying to seek for clean and sustainable energy options. Therefore, clean energy like solar and wind has attracted numerous attention. However, as the solar and wind energy need to be stored before they can be utilized, it is crucial for the development of efficient and effective electrical storage systems.<sup>1,2</sup> Rechargeable batteries are one of the most viable options of the energy storage systems.

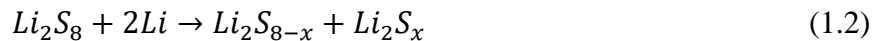
Lithium-ion batteries (LIBs), with its high energy and power density, has been widely used in people's daily life since its commercialization in 1991.<sup>3</sup> Tremendous progress has been achieved in portable electronic devices such as cellphones, laptops, etc. Besides, lithium cobalt oxides and graphite have been the dominate electrode materials in LIBs for almost two decades, because of their relatively high energy/power density and stable cycling performance.<sup>2</sup> To improve the energy density of LIBs, advanced composite electrodes like silicon-based anode materials have received intensive research attention nowadays as they have much higher capacities than traditional electrode materials. However, due to the continuously increasing demand for high-energy density batteries in large-scale applications like e-bikes and electrical vehicles (EVs), LIBs finally reach their bottleneck, which is because of the inherent chemistry limitations of those simple insertion-compound electrodes.<sup>4</sup> Therefore, materials that can accommodate more electrons and ions would be the prioritized choice for the further increase in energy density of rechargeable batteries.<sup>1</sup>

With this perspective, elemental sulfur (S), one of the most abundant element in earth's crust, is a perspective electrode material candidate as it has a high theoretical capacity of 1675 mAh g<sup>-1</sup>, which is nearly one magnitude higher than those of the insertion-compound electrodes of LIBs.<sup>1, 5-6</sup> Figure 1.1 shows the structure of a typical lithium-sulfur battery, which consists of S cathode, lithium metal anode and the separator/electrolyte between them. As S is in the charged state, the cell starts with the discharge reaction, in which Li metal is oxidized and produces Li ions with electrons at the negative electrode. The as-generated Li ions in the negative side can diffuse through the electrolyte internally to the positive electrode while the electrons travel by the external electrical circuit to the positive electrode. The elemental S undergoes multistep electrochemical reactions to form lithium sulfides by accepting Li ions and electrons in the positive electrode during discharge and this process can be divided into 4 regions as listed below.<sup>1-2, 5-6</sup>

Region 1: A solid-liquid reduction from S to long-chain Li<sub>2</sub>S<sub>8</sub>.



Region 2: A liquid-liquid reduction from long-chain Li<sub>2</sub>S<sub>8</sub> to low-order polysulfides (Li<sub>2</sub>S<sub>x</sub>, 4 ≤ x ≤ 8).



Region 3: A liquid-solid reduction from low-order Li<sub>2</sub>S<sub>x</sub> to solid state Li<sub>2</sub>S<sub>2</sub> or Li<sub>2</sub>S.



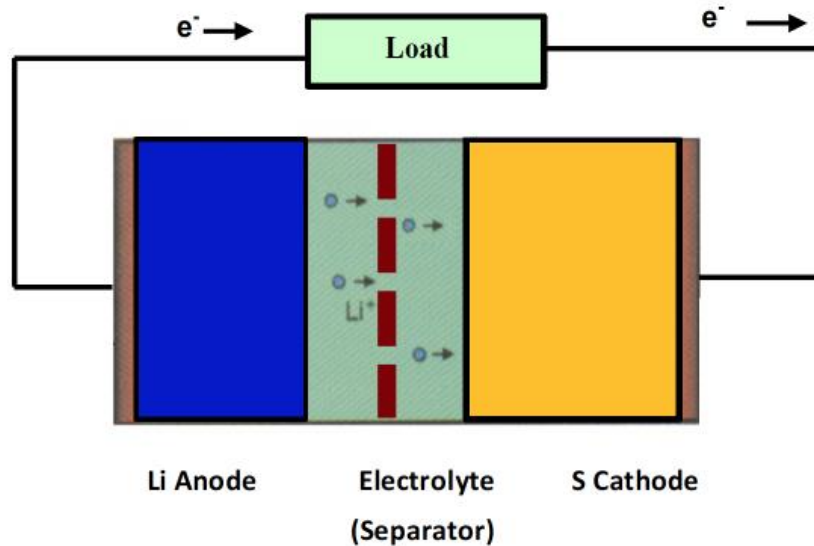
Region 4: A solid-solid reduction from  $\text{Li}_2\text{S}_2$  to  $\text{Li}_2\text{S}$ .



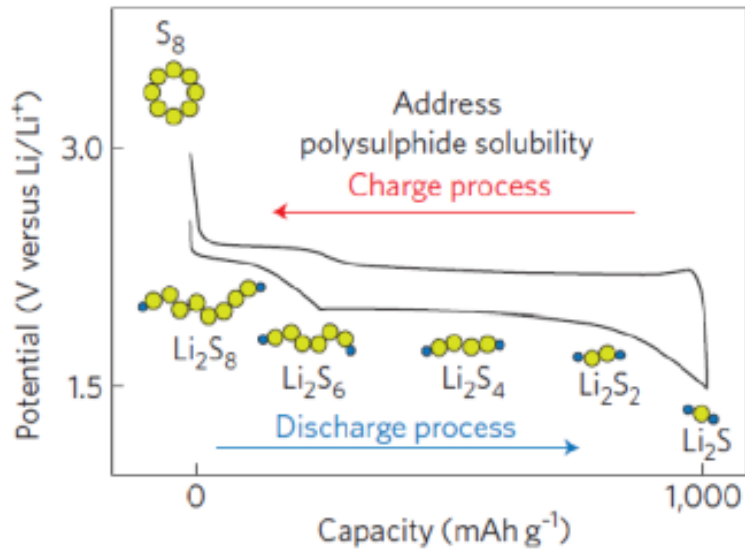
In contrast, during the charge process, oxidation reaction happens that lithium sulfides are oxidized to polysulfides and finally to S. Thus, the overall redox reaction could be concluded as:



Figure 1.2 indicates the voltage profiles of a Li-S cell. The average voltage for Li-S cell is around 2.15 V with respect to  $\text{Li}^+/\text{Li}$ .<sup>1</sup>



**Figure 1.1** A typical structure of Li-S batteries.



**Figure 1.2** Voltage profiles of Li-S cell.<sup>1</sup>

## 1.2 Challenges and System Limitations of Lithium-Sulfur Batteries

There are key challenges and system limitations that need to be addressed before the practical application of Li-S cells. In general, the Li-S cells suffer from rapid capacity fading and the practical capacity/cycle life are usually lower than expected.<sup>1-2, 5</sup>

### 1.2.1 Insulating Nature of Elemental Sulfur and its Discharge Products

The poor electrical and ionic conductivity of S and its discharge products, *i.e.* polysulfides and lithium sulfides, remain to be the most challenging issue that hinders the practical application of Li-S batteries.<sup>1, 5</sup> The electrical conductivity of S at 25 °C is  $5 \times 10^{-30} \text{ S cm}^{-1}$  that it cannot be utilized in cathode without conductive additives.<sup>2</sup> To increase the electrical conductivity and

enhance the active material utilization, carbon-based materials and conducting polymers are applied to combine S in cathode structure designs.<sup>7-9</sup> However, even though the electrical conductivity of S cathode could be improved to some degree, the ionic conductivity remains to be low.<sup>10-11</sup>

### 1.2.2 Shuttling Effect of Discharge Intermediate – Polysulfides

The use of organic liquid electrolyte in traditional Li-S batteries leads to another prominent challenge, which is the shuttling performance of discharge intermediate – polysulfides. Since the polysulfides is highly soluble in organic electrolyte, it can diffuse through the separator reaching lithium metal anode and reacts with the Li, forming short-chain polysulfides with lithium sulfide (Li<sub>2</sub>S) deposition. Then the short chain polysulfides can diffuse back to the cathode side and be re-oxidized, thus leading the loss of active material, corrosion of Li anode and low Coulombic efficiency.<sup>2, 5-6</sup>

### 1.2.3 Large Volume Change of Sulfur Cathode

The diffusion of S related species could lead to the redistribution of active materials in S cathode, which greatly affects the cycling performance of Li-S cells. Besides, as the density of S and lithium sulfides are 2.07 and 1.66 g cm<sup>-3</sup>, respectively, the large volume expansion originating from the density difference during charge/discharge process destroys the structure integrity of the S cathode, which could lead to active material detachment from the conductive matrix.<sup>12</sup>

#### 1.2.4 Safety Issues

Aside from the problems from redox reaction, safety is another important concern that needs to be addressed before the practical application of Li-S batteries. So far, it has been recognized that the electrolyte consists of bis(trifluoromethane)sulfonamide lithium salt (LiTFSI) and lithium nitrite ( $\text{LiNO}_3$ ) in the mixture solvent of 1,3-dioxolane (DOL)/1,2-dimethoxymethane (DME) (1:1 by volume) is the most efficient liquid electrolyte for Li-S batteries.<sup>11, 13</sup> However, the safety issues originating from the low flashing/boiling point of the organic DOL (flashing point:  $-2\text{ }^\circ\text{C}$ ; boiling point:  $75\text{ }^\circ\text{C}$ )/DME (flashing point:  $-18\text{ }^\circ\text{C}$ ; boiling point:  $42\text{ }^\circ\text{C}$ ) solvent remains to be a big problem, which leads to the inflammability and electrochemical instability of Li-S batteries and severely restricts the practical applications which need higher operating temperatures.<sup>13</sup>

### 1.3 Recent Advances in Separators of Traditional Liquid Lithium-Sulfur Batteries

Since the electrical conductivity of S is relatively low ( $5 \times 10^{-30}\text{ S cm}^{-1}$ ), in traditional liquid Li-S cells, conducting materials such as carbon-based materials and conducting polymers are always used to improve the electrical conductivity of S. For example, the structural design of S cathode is one of the strategies to improve the electrical conductivity of S and to reduce the shuttling effect of polysulfides, in which S is always combined with/without micro-/mesopores and functional groups (e.g., oxygen containing groups, nitrogen groups, etc.).<sup>7-8</sup> It is claimed that because of the relatively high electrical conductivity and the physical/chemical interactions, *i.e.*, the relatively closed environment of carbon frameworks and the interactions between the negatively-charged S-related species and the functional groups in carbon materials, the active material

utilization/polysulfides diffusion could be significantly improved/minimized, thus leading to stable cycling performance of Li-S cells. Although progressive improvements have been achieved, it is still technically impossible to comprehensively avoid the polysulfide shuttling in Li-S cells with high S concentrations.

In addition to the structure designs of S cathodes, coating the separators with functional layers/inserting effective layers between cathode and anode (interlayers) could be another effective approach to minimizing the shuttling of polysulfides and improve the active material utilization.<sup>6</sup>

<sup>14</sup> It is well known that the separator also plays a crucial role in batteries. The conventional role of separators is to separate the cathode and the anode to prevent the electrical short circuit while helping transport ions. However, in addition to the traditional role, the coated separators/interlayers could also play a crucial role in relieving the polysulfide diffusion by controlling the negatively-charged S-related species. In this respect, the electrochemical performance of Li-S cells will be largely enhanced with those separator modifications.

In this chapter, the recent advances in the development of separators in traditional liquid Li-S cells are reviewed and discussed. The materials which are used as functional layers are also reviewed in this chapter correspondingly based on the type and morphology.

### 1.3.1 Modification of Traditional Separators

Compared with the intensive studies on the structure design of S cathode, few researchers have focused on the separator part for Li-S batteries. Typically, as mentioned above, an ideal separator

for Li-S batteries should not only have good ionic conductivity (high electrolyte uptake) but also should help mitigate the diffusion of polysulfides.<sup>15</sup> Microporous polypropylene (PP) membrane is the most commonly used separator for Li-S battery because of its good chemical stability and mechanical strength. However, the relatively low ionic conductivity and poor performance in trapping polysulfides of PP separator hinder the electrochemical performance of Li-S cells.<sup>15</sup>

With the aim of addressing the poor performance of PP separator, Yao *et al.* first tried to coat PP separator with different conductive materials: carbon-based materials that have large surface area and high electrical conductivity; and, metal oxides which have strong binding energy with the negatively-charged polysulfides.<sup>14</sup> The thickness of the coating layers is around 1  $\mu\text{m}$ . Figure 1.3 shows the schematic configuration of a Li-S cell with coated separators. It is seen that the functional layers are inserted between the S cathode and separator, acting as a second current collector that offer multiple conducting sites for the trapping and reutilization of polysulfides, which greatly minimized the internal resistance of the cell and significantly improved the active material utilization. Figure 1.4 indicates the cycling performance of Li-S cells with different coating materials. It's obvious that the conductive carbons, including super P, ketjen carbon and multi-wall carbon nanotube (MWCNT) demonstrates better performance than metal oxides (aluminum oxides -  $\text{Al}_2\text{O}_3$ ) and titanium oxides -  $\text{TiO}_2$ ), which is probably because of the higher electrical conductivity of carbon materials that offer adequate conductive sites for the polysulfide trapping.

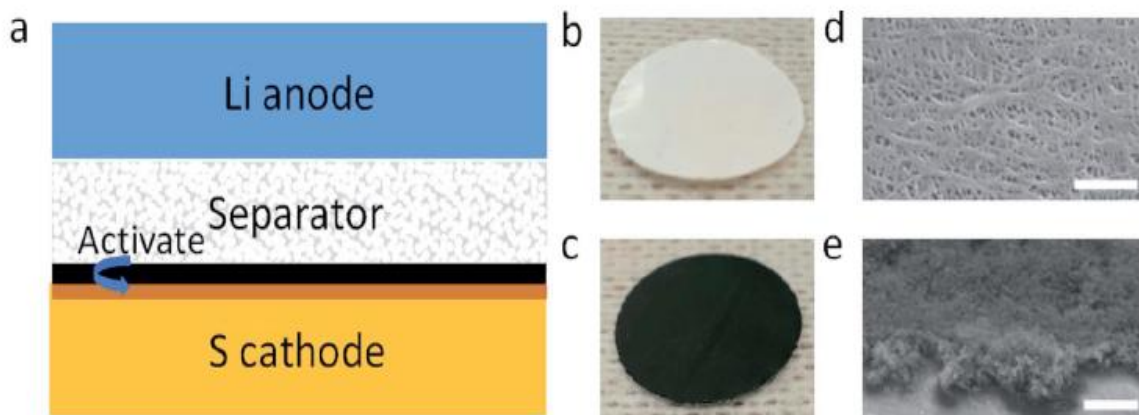


**Figure 1.3** (a) Schematic configuration of Li-S cells with coated PP separators. Photographs of (b) bare PP separator and (c) super P coated separator. SEM images of (d) pristine separator and (e) super P coated separator.<sup>14</sup>

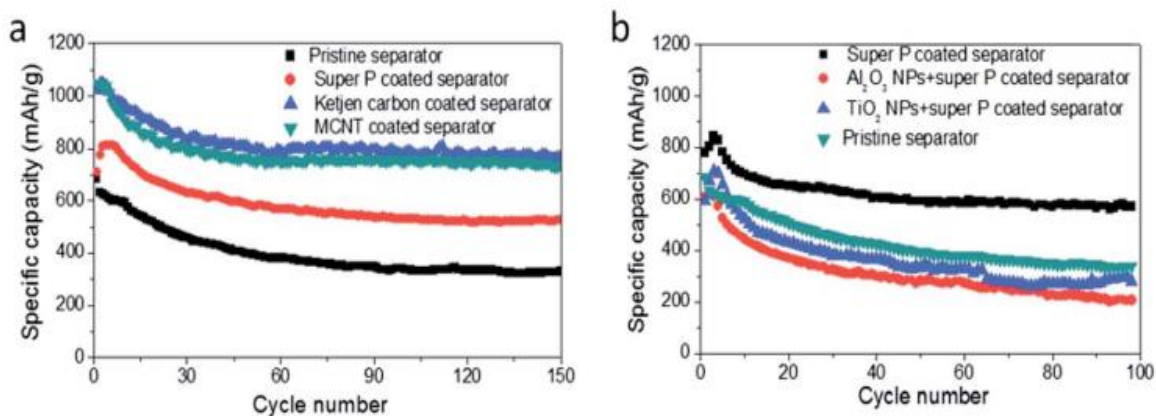


**Figure 1.4** Cycling performance of Li-S cells with different material coatings on separators.<sup>14</sup>

In addition to the conducting carbonous materials and metal oxides, ion selective Nafion® membrane is also selected to coat PP separator.<sup>16</sup> The sulfonate-ended perfluoroalkyl ether groups in Nafion® membrane only allow for the ion hopping of positively charged species, like Li<sup>+</sup>, while rejects hopping of negatively charged species, such as S-related species (S<sub>n</sub><sup>2-</sup>). Figure 1.5 indicates

the schematic configuration of this effective Li-S cell structure design. For the routine membrane, the polysulfides can diffuse freely between the S cathode and Li anode. On the contrary, for the separator with this ion-selective membrane, the negatively-charged polysulfides is largely restricted between the S cathode and the ion selective membrane, because of the electrostatic force between sulfite anion groups and polysulfides, thus the cycling stability of Li-S cell is significantly improved with a low cyclic capacity decay of 0.08% per cycle over 500 cycles as shown in Figure 1.6.

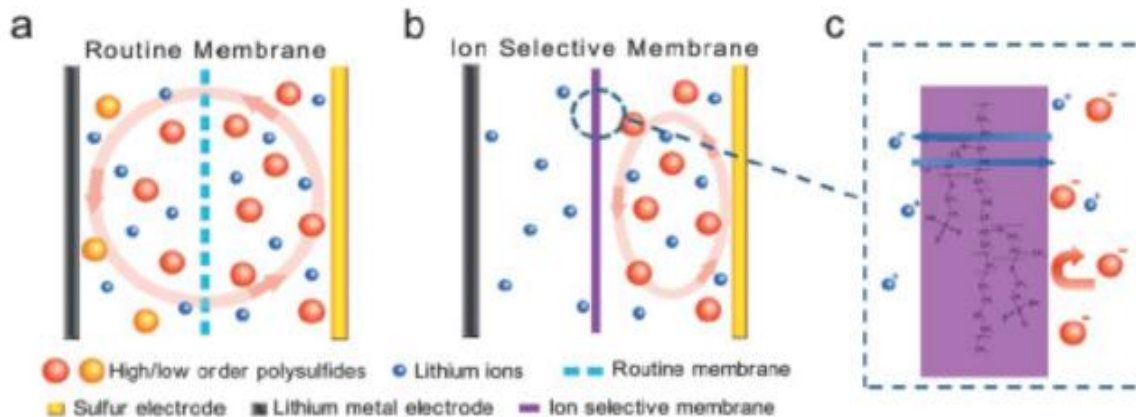


**Figure 1.5** Schematic configurations of different Li-S batteries.<sup>16</sup>

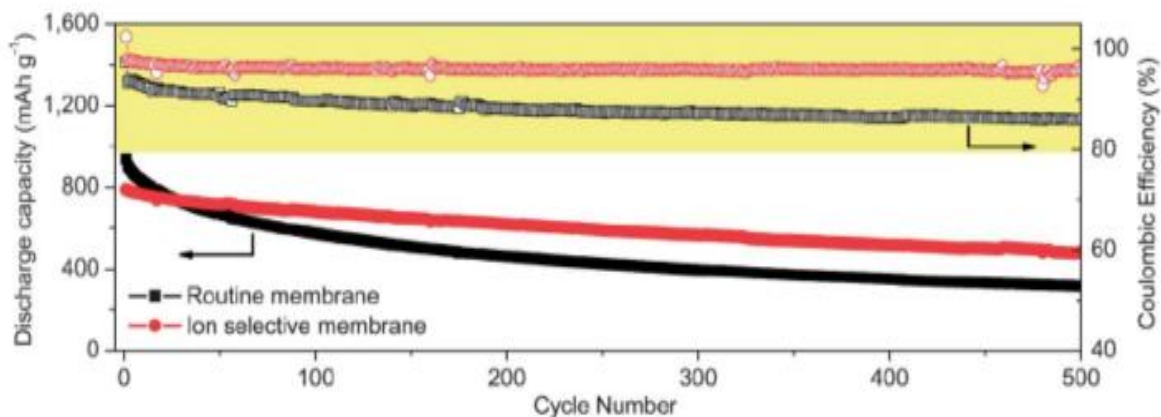


**Figure 1.6** Cycling performance of Li-S cell with ion-selective membrane.<sup>16</sup>

### 1.3.2 Novel Separators for Lithium-Sulfur Batteries

Although considerable breakthroughs have been made with those coated separators with carbonous materials, metal oxides and ion-selective polymers, the rate capabilities of Li-S cells are still not ideal. In general, the PP separator suffers from poor electrolyte wettability and low porosity, which will increase the cell internal resistance and finally lead to the sluggish reaction kinetics of Li-S batteries. Besides, since the melting temperature of PP separator is usually low, the large thermal shrinkage when operating at high temperatures may induce internal short circuit as well as severe safety problems like explosion. Therefore, it is essential to explore novel separators with porous structure, high electrolyte uptake and excellent thermal stability.

### 1.3.2.1 Ceramic Glass Fiber (GF) Membrane Separator

Commercial glass fiber membrane is made from borosilicate.<sup>17</sup> Compared to microporous PP membrane, it has highly porous structure, good thermal stability and excellent electrolyte wettability. These features make GF membrane quite suitable for use as separators in Li-S batteries.

Wang *et al.* first designed a hybrid separator composed of a GF membrane and a microporous PP membrane for Li-S batteries.<sup>17-18</sup> Figure 1.7a indicates the schematic cell configuration of this new design, where GF membrane is inserted between the S cathode and the PP membrane. This unique cell configuration has many advantages: *i*) highly porous structure of GF can result in high electrolyte intake and thus leading to a high ionic conductivity of the electrolyte soaked GF separator, which is favorable for the rapid electron transfer; *ii*) the highly porous structure can also cause high polysulfides intake and slow down the rapid diffusion of polysulfides to Li metal anode; and, *iii*) the excellent thermal stability of GF separator, which comes from the intrinsic thermal resistance of borosilicate, is beneficial for the safe operation of Li-S cells in high temperature atmosphere. As a result of the aforementioned benefits of GF membrane, the Li-S cell with this hybrid separator could deliver a stable cycling performance up to 500 cycles (as showed in Figure 1.7b) with excellent rate capabilities.

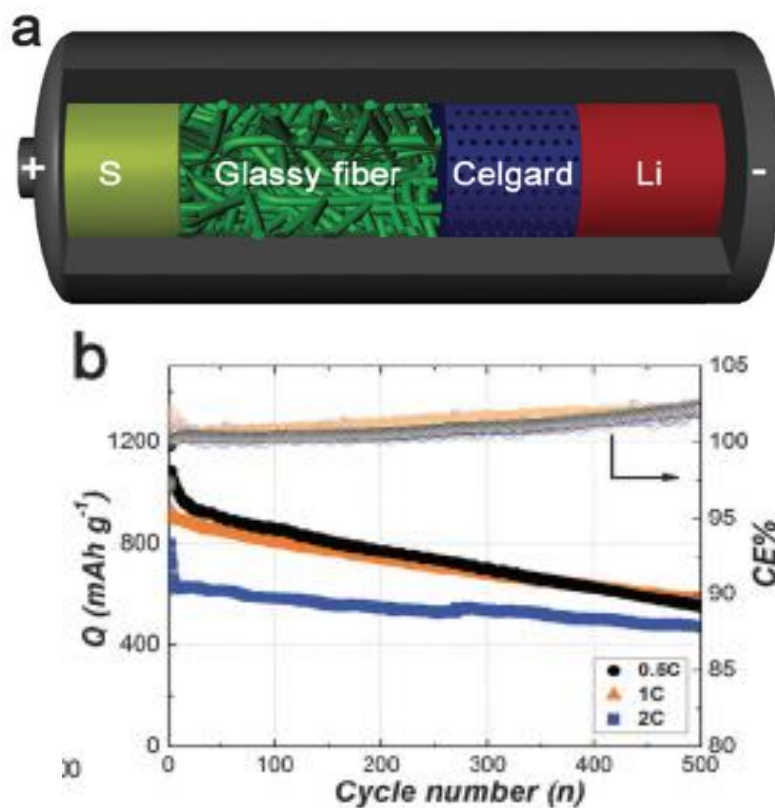


**Figure 1.7** (a) Schematic cell configuration of Li-S cell with hybrid separator. (b) Cycling performance of Li-S cell with the hybrid separators.<sup>17-18</sup>

Inspired by this hybrid separator design of the combination of GF and PP separator, Zhu *et al.* directly used GF membrane as separator for Li-S batteries.<sup>19</sup> The Li-S cell with GF separator can remain a high reversible capacity of 617 mAh g<sup>-1</sup> after 100 cycles, which are almost 42% higher than the cell with traditional PP separator. The excellent electrochemical performance of Li-S cell with GF separator is coming from the super porous structure which guarantees high electrolyte uptake and mitigates the diffusion of polysulfides to the Li metal anode side. Figure 1.8a and b show the schematic illustration of the cells with PP and GF separators. In addition, significantly enhanced rate capabilities can be achieved in Li-S cell with GF separator (Figure 1.8c). Compared with cell with PP separator, which only remained a capacity of 111 mAh g<sup>-1</sup> at 2 C (1-piece PP),

the cell with GF separator showed a high reversible capacity of 262 mAh g<sup>-1</sup> at 2 C, revealing the fast-redox reaction in cell with GF separator.

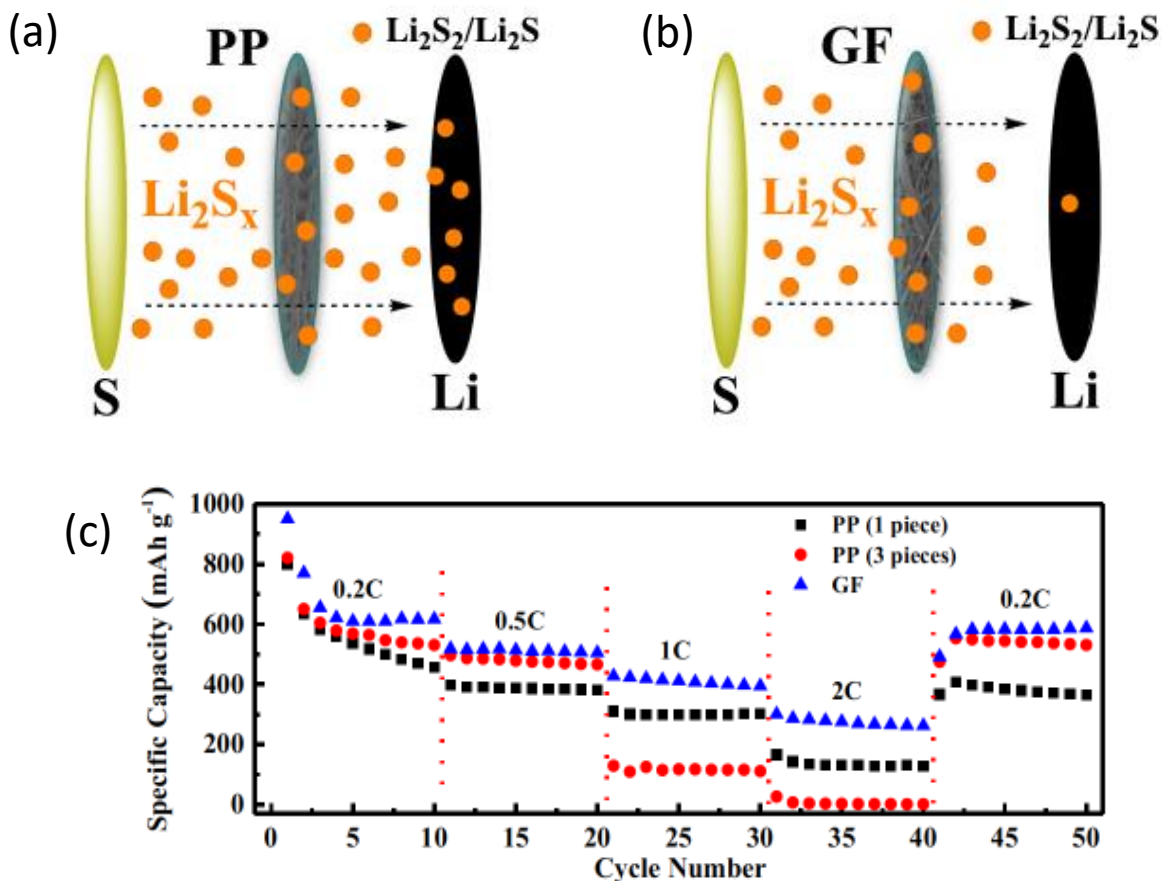


**Figure 1.8** Schematic illustration of Li-S cell with (a) PP and (b) GF separator, showing the excellent ability of GF in blocking polysulfides. (c) Rate capabilities of Li-S cell with GF separator.<sup>19</sup>

However, even though the improved electrochemical performance with enhanced thermal stability could be achieved in Li-S cells when using GF as separators, the geometric and volumetric energy density of Li-S cells are often lowed as the GF membrane has a thickness of around 260 μm.

Therefore, it is urgent to seek for separators with appropriate thickness and good electrochemical performance.

### 1.3.2.2 Electrospun Nanofiber Separators

Recently, electro-spun nanofiber membranes have gained much attention as an alternative approach to replace the traditional PP membrane due to its easy processibility and controllable morphology/size.<sup>20-23</sup> Electrospinning is the main technique that use to produce nanofibers. In addition, the as-produced nanofiber membrane usually has a high specific surface area to volume ratio, which could produce sufficient reaction sites for the dissolved polysulfides while at the same time, the empty space between the nanofibers can also accommodate the volume change during cycling.

Zhu *et al.* fabricated a highly porous polyacrylonitrile/graphene oxide (PAN/GO) nanofiber membrane separator for Li-S batteries.<sup>24</sup> Compared to traditional PP separator, this newly designed composite nanofiber membrane has highly porous structure, better thermal stability and abundant  $-C\equiv N$  groups (from PAN polymer)/oxygen-containing groups (from GO), which can offer higher electrolyte uptake for rapid electron transfer and better polysulfide rejection for stable cycling performance (because of the electrostatic force between the negatively charged S related species and functional groups). Figure 1.9 shows the schematic model and mechanism of the PAN/GO membrane. Therefore, as a result of the superior functionalities of this effective composite PAN/GO nanofiber membrane separator, the Li-S cell with PAN/GO separator can deliver a stable

cycling performance over 100 cycles with a reversible capacity of 597 mAh g<sup>-1</sup>, which is 38% higher than cell with PP separator.

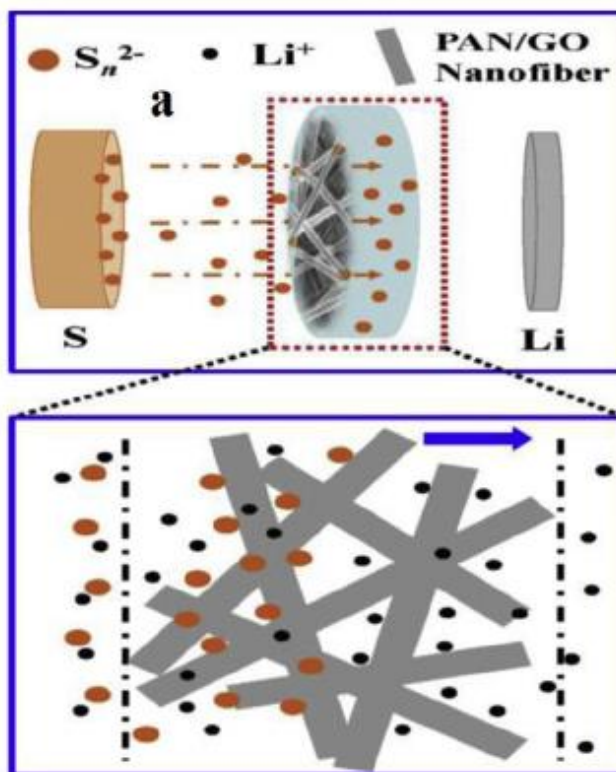


**Figure 1.9** Schematic illustration of the Li-S cell with PAN/GO separator.<sup>24</sup>

Hao *et al.* prepared an extra strong polyoxazole nanofiber membrane to be used as separator in batteries.<sup>25</sup> The high modulus polymeric nanofibers can be processed to prepare flexible and strong membrane separator, which can prevent the lithium dendrites growth/penetration and meet the safe operation requirement of Li-S batteries. In addition, those membranes can withstand a high temperature up to 600 °C with a low ionic resistance during cycling. Moreover, the abundant oxygen (O-) and nitrogen (N-) containing functional groups in the membrane can also help trap the polysulfides from diffusing (due to the electrostatic force between the O-/N- functional groups

and the polysulfides), thus the overall electrochemical performance of Li-S cells is significantly enhanced. Figure 1.10 indicates the schematic of this strong/effective polyoxazole nanofiber membrane.

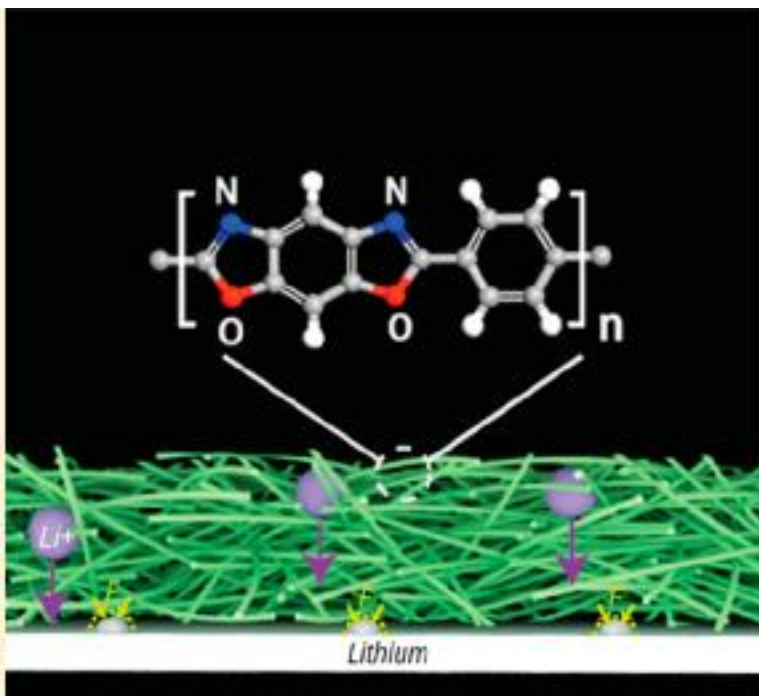


**Figure 1.10** Schematic illustration of polyoxazole nanofiber membrane.<sup>25</sup>

#### **1.4 Recent Development of All-Solid-State Lithium-Sulfur Batteries**

During the past few years, most researches have been focused on the liquid electrolyte Li-S batteries to address the problems raised from nonconductive nature of S, polysulfides shuttling and large volume change of S during repeated charge-discharge process.<sup>1-3</sup> Although intensive progresses have been achieved by the incorporation of carbon-based materials,<sup>7, 24</sup> conducting

polymers<sup>10</sup> and metal oxides<sup>26</sup> in S cathode structure design/separator modification, it is still technically impossible to comprehensively avoid the polysulfide shuttle in traditional liquid electrolyte Li-S cells.<sup>11</sup> Besides, the safety issues coming from the flammable organic solvent as well as the formed lithium dendrites during repeated cycling are another two main safety obstacles that restrict the development of traditional Li-S cells, despite the merits of high ionic conductivity and excellent wetting ability of liquid electrolyte.<sup>26</sup>

Replacing the liquid electrolyte with solid electrolyte provides “game-changing” opportunities for the practical application of Li-S batteries as it can lead to consistent improvements in electrochemical performance of Li-S cells with safe operation. However, the crucial challenges from solid electrolyte as well as the poor contact of solid-solid interfaces between electrode and solid electrolyte remain to be tough tasks in all-solid-state Li-S batteries (ASSLSBs).<sup>13, 27-28</sup>

In this chapter, the recent developments in solid electrolytes and electrodes for all-solid-state Li-S batteries are reviewed and discussed.

## 1.4.1 Solid Polymer Electrolytes for All-Solid-State Lithium-Sulfur Batteries

### 1.4.1.1 Brief Introduction of Solid Polymer Electrolytes

Solid electrolytes with ionic conductivity comparable to that of liquid electrolyte are promising alternatives to these conventional liquid electrolytes in safe rechargeable Li-S batteries. A good solid electrolyte must have a high ionic conductivity at room temperature, a wide electrochemical stability window (up to 5V vs. Li/Li<sup>+</sup>) and excellent compatibility with metallic lithium.<sup>11, 29-</sup>

<sup>30</sup>Among all types of solid electrolytes, solid polymer electrolytes (SPEs) have gained much research attention because of the advantages listed below: *i*) good mechanical strength of SPEs effectively mitigates the dendrite penetration; *ii*) the potentially high electrochemical stability window enlarges the operation voltage of cells; *iii*) the solid state nature of SPEs fundamentally avoids the polysulfide diffusion and lithium dendrite formation; and *iv*) the easy processibility, good flexibility and low flammability characteristics of SPEs also contribute to the fabrication of flexible and safe ASSLSBs.<sup>31-32</sup>

In SPEs, various polymers such as polyacrylonitrile (PAN),<sup>33</sup> poly(ethylene oxide) (PEO),<sup>34</sup> poly(vinylidene fluoride) (PVDF)<sup>35</sup> and poly(methyl methacrylate) (PMMA)<sup>34</sup> are usually blended with Li salts. Figure 1.11 indicates the chemical structures of the extensively studied polymer matrix for solid electrolytes.<sup>31</sup> Among all of them, PEO based solid polymer electrolytes are intensively studied.<sup>32-33, 36</sup> However, the relatively low ionic conductivity of PEO based SPEs at room temperature (usually around  $10^{-6} - 10^{-8}$  S cm<sup>-1</sup>), severely hinders their application in ASSLSBs.<sup>32-33</sup> Hence, efforts should be made to fabricate highly ionic conductive SPEs.

### Polymer matrices

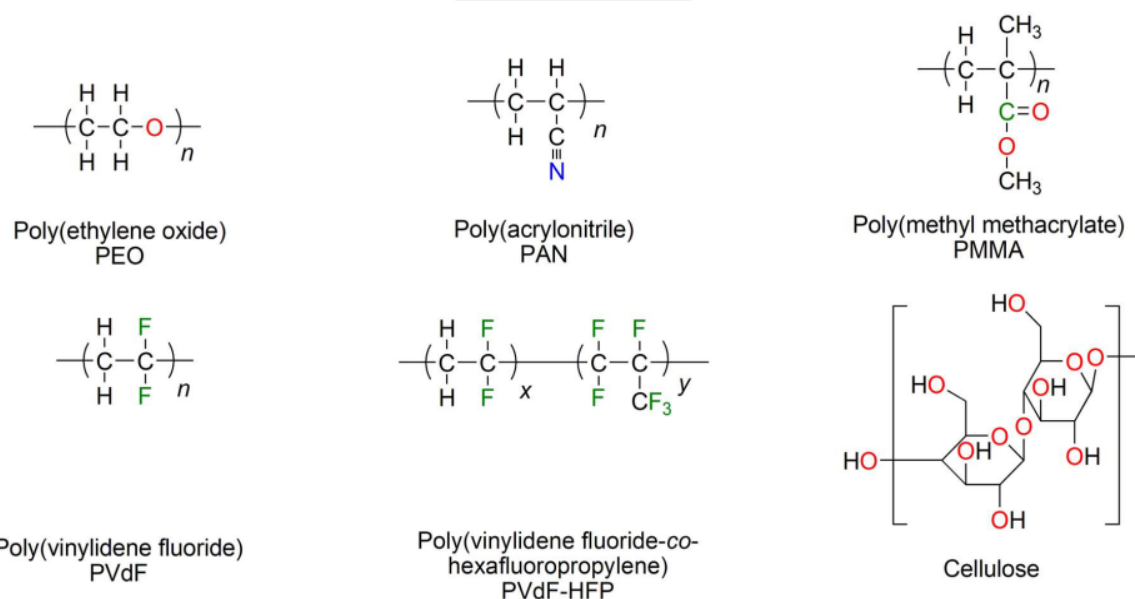


**Figure 1.11** Chemical structures of extensively studied polymers for solid electrolytes.<sup>31</sup>

#### 1.4.1.2 Mechanism of Ionic Transport in Solid Polymer Electrolytes

In SPEs, the ion transport is mainly related to the segmental motion of polymer chains above glass transition temperature.<sup>37</sup> Basically, the segmental motion of chains can create free volumes for the hopping of lithium ions, which are in coordinating with the polar groups. Lithium ions can hop from one site to another coordinating site according to the segmental motion of polymer chains, thus the long-distance transport of ions is realized by continuous hopping under electrical field. Besides, the dissociation ability of the lithium salt in polymer matrix can also be used to determine the number of free ions, which is another crucial affecting factor in ion transport.<sup>30, 37</sup>

In addition, when it comes to the PEO based solid polymer electrolytes, as PEO contains ether coordination sites, the dissociation of Li salts can be promoted; while the flexible macromolecular

structure of PEO can also assist ionic transport. The ionic motion of a lithium ion in a PEO host is displayed in Figure 1.12a.<sup>38</sup> On the contrary, the existence of crystalline domains in PEO polymer matrix severely restricts the ion transfer at room temperature because of the low level of segmental motions, as showed in Figure 1.12b.<sup>37</sup> To get a high level of segmental mobility, PEO based SPEs is always operated above the melting temperature, where the ionic conductivity strongly increase because of the increased free volume for ion transfer. However, at those temperatures, PEO loses its dimensional stability and becomes a viscous liquid, which is not ideal for the blocking of Li dendrites.<sup>37-38</sup>

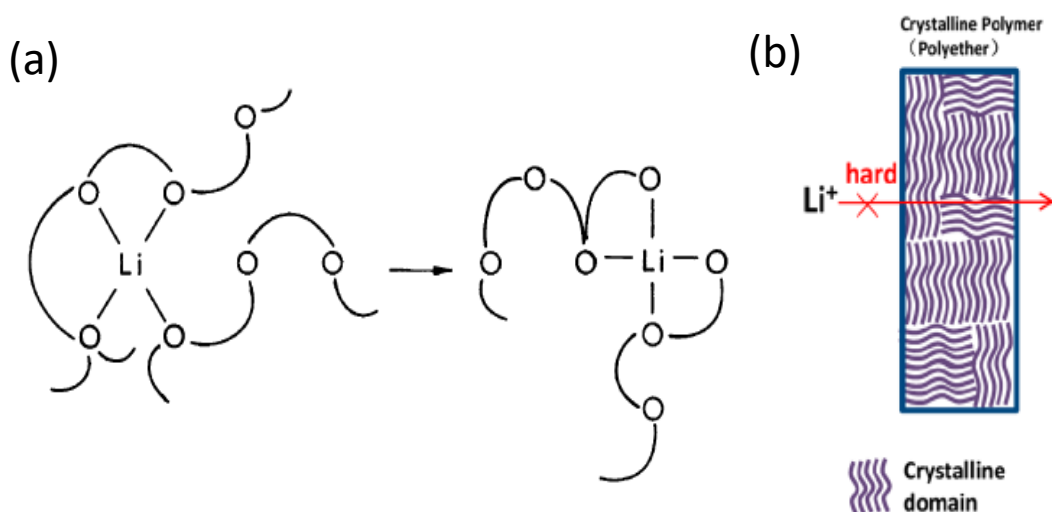


**Figure 1.12** (a) Li ion motion in a PEO polymer host. (b) Mechanisms of Li-ion transfer in crystalline domains of polymer matrix.<sup>37-38</sup>

#### 1.4.1.3 Approaches to Increase the Ionic Conductivity of PEO based SPEs

To suppress the crystallization (increase the ionic conductivity) of PEO, various approaches have been used, including: *i*) addition of plasticizers into the polymer matrix; *ii*) forming crosslinked or

blocked copolymers to change the structure of PEO; and *iii*) addition of ceramic fillers into the polymer matrix.<sup>32-33, 37-38</sup>

#### *Addition of plasticizers into the polymer matrix*

In the efforts of increasing room temperature ionic conductivity of PEO polymer electrolyte, various additives are researched. Plasticizers are low molecular weight components such as ionic liquids with large anion salts and small organic solvents such as carbonates, dimethyl and tetra(ethylene glycol) etc.<sup>37-38</sup>

Kelley *et al.* found that the adding of low molecular weight PEO into the polymer matrix can decrease the glass transition and melting temperature of the polymer while at the same time, can increase the solubility of crystalline polymer and salt composite.<sup>39</sup> Besides, Ito *et al.* used poly(ethylene glycol) (PEG) as the plasticizer in the PEO/Li salt composite and they observed that the ionic conductivity improves with the increase of PEG content, which could be ascribed to the crystallinity decrease/free volume increase in the system.<sup>40</sup>

In addition, Egashira *et al.* investigated the conduction mechanism of polymer electrolyte system consisting of PEO branched poly(methyl methacrylate) (PEO-PMMA) matrix with ionic liquids of the 1-ethyl-3-methyl imidazolium bis(trifluoromethane sulfone)imide (EMITFSI) and the hexyltrimethylammonium bis(trifluoromethane sulfone)imide (HTMATFSI).<sup>41</sup> It is found that the mobility of Li ions in SPEs is strongly affected by the type of ionic liquid that HTMATFSI contributes more in the ion conduction. Figure 1.13 shows the schematic model of these two ionic

liquids in the PEO/PMMA electrolyte system.<sup>41</sup> It is seen that the Li ions tend to be solvated strongly with the ethylene oxides and are fixed while it can act as charge carrier in electrolyte with HTMAFSI.

However, even though the crystallinity of the polymer is restricted because of the adding of small molecular/ionic liquid plasticizers, the mechanical strength as well as the electrochemical stability window are always lowered and probably that's the reason that why all the three literatures mentioned above didn't give any information about these two properties of SPEs.<sup>32-33, 37</sup> Therefore, other approaches need to be considered to improve the ionic conductivity of SPEs without the sacrifice of other merits of SPEs.

#### *Crosslinked or blocked copolymers*

To combine the properties of high ionic conductivity and good mechanical strength/large electrochemical stability window in SPEs, crosslinked polymers and blocked copolymers are studied extensively.<sup>37-38</sup>

In blocked copolymers, the most common structures are AB diblock and BAB triblock, in which A is the conductor block and B is the mechanical support block.<sup>42</sup> Generally, in PEO based blocked copolymers, the A block consists of a linear PEO block while the mechanical reinforcement block usually consists of a wide variety of polymers, such as polystyrene and poly(alkyl methacrylates).

Bouchet *et al.* reported single-ion BAB triblock copolymers as a highly efficient electrolyte for lithium-metal batteries.<sup>42</sup> Here, the polyanionic block copolymer was comprised with polystyrene segments, which acted as a mechanical support in blocked copolymer. Figure 1.14 shows the chemical structure of the as-synthesized triblock copolymers with the Li ions (donated as P(STFSILi)-PEO-P(STFSILi)). As the polyanionic blocked copolymer electrolytes (A-BCE) was combined with the well-known TFSI anion, it enabled an important delocalization of the negative charge, which could significantly increase the current fraction carried by Li ions into the PEO conducting phase, thus increasing the Li ion transference number in the solid electrolytes. Based on the [EO]/[Li] ratios, different polyanionic/polystyrene/TFSI (PSTFSI)-PEO-PSTFSI triblock copolymers were designed and the ionic conductivity, mechanical strength and electrochemical stability window were tested. The results are demonstrated in Figure 1.15. The as-synthesized P(STFSILi)-PEO-P(STFSILi) triblock copolymer with 20% P(STFSILi) exhibited an excellent ionic conductivity of  $1.3 \times 10^{-5} \text{ S cm}^{-1}$  at 60 °C with a large Li ion transference number of 0.85. Besides, significantly improved mechanical strength and an enlarged electrochemical stability window up to 5 V versus  $\text{Li}^+/\text{Li}$  were also observed, which satisfied all the requirements for high performance PEO based SPEs.

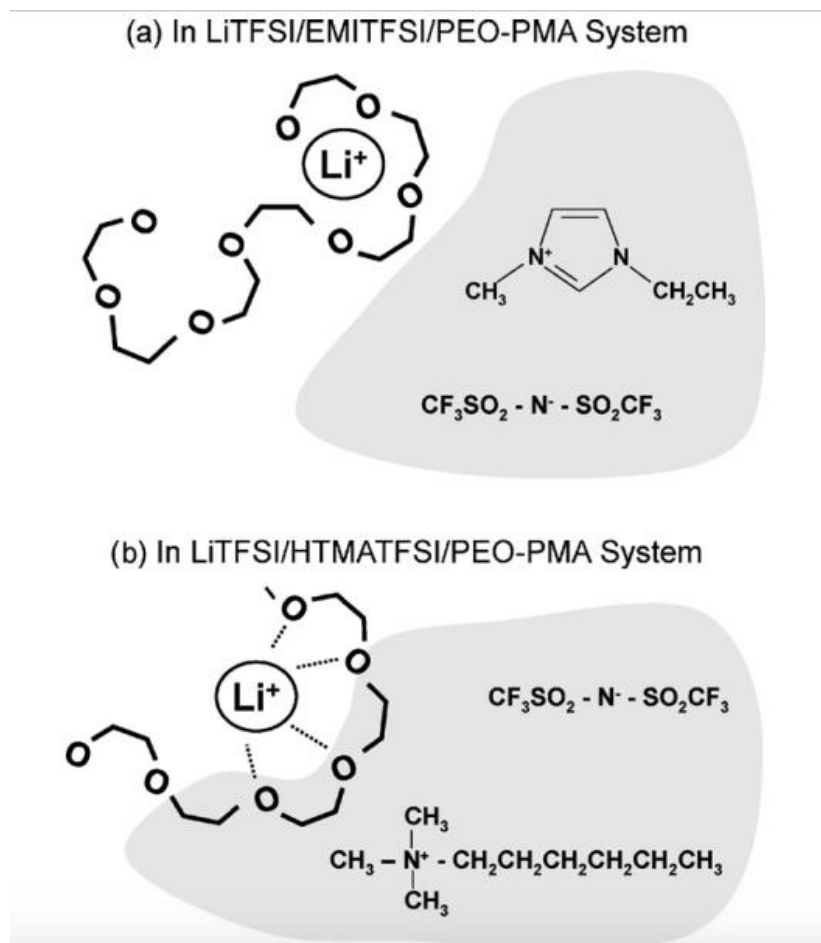


**Figure 1.13** Schematic model of these two liquids in PEO/PMMA electrolyte system.<sup>41</sup>

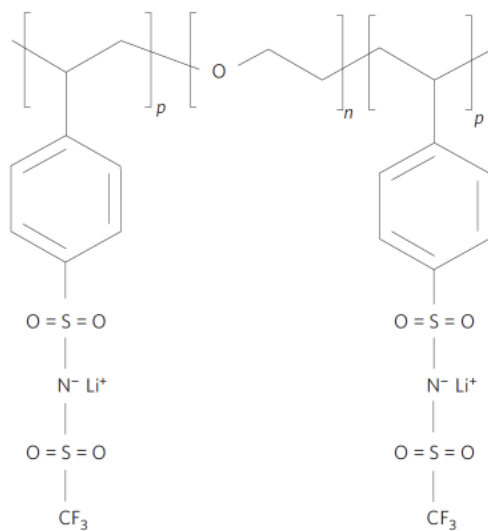


**Figure 1.14** Chemical structure of triblock copolymer of P(STFSILi)-PEO-P(STFSILi).<sup>42</sup>

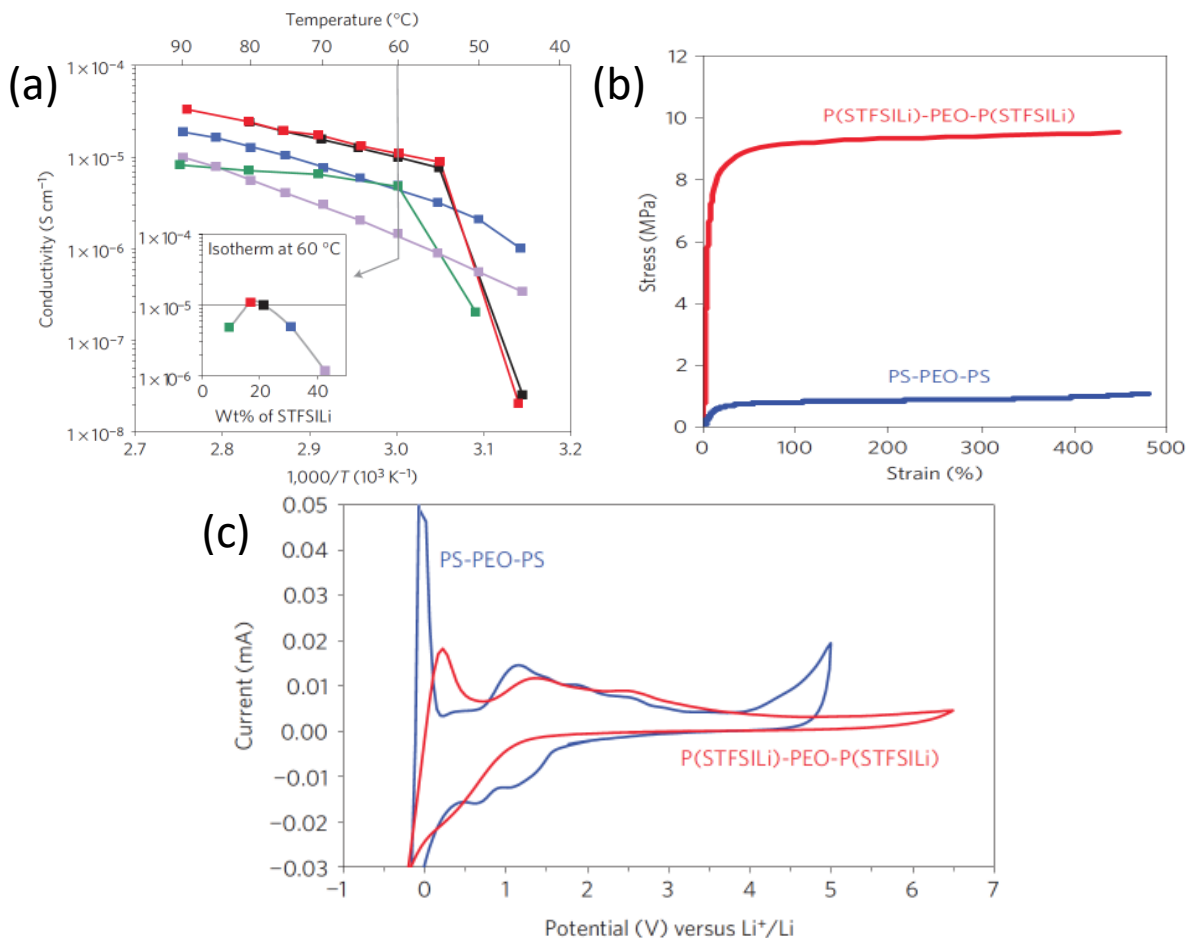


**Figure 1.15** (a) Plots of conductivity at various temperatures of several P(STFSiLi)-PEO-P(STFSiLi). (b) Mechanical performance of copolymer P(STFSiLi)-PEO-P(STFSiLi) with 31% P(STFSiLi) at 40 °C. (c) Electrochemical stability window tested at 80 °C.<sup>42</sup>

In addition, crosslinking is another way to suppress the crystallinity of polymer and improve the ionic conductivity of SPEs. Besides, it gives the polymer rubber-like characteristics, which is ideal for mechanical strength enhancement in SPEs.<sup>43</sup> Khurana *et al.* designed a cross-linked electrolyte for lithium-metal batteries, which composed of stiff semi-crystalline polyethylene (PE) chains covalently cross-linked by PEO segments. The PE backbone length between crosslinks and PEO segment lengths can significantly suppress the crystallization of PEO and improve the ionic

conductivity of SPE, thus a high ionic conductivity of above  $10^{-4}$  S  $\text{cm}^{-1}$  was obtained with exceptional dendrite growth resistance. Figure 1.16 demonstrates the chemical structure of this crosslinked PE/PEO solid polymer electrolyte with LiTFSI salt.<sup>43</sup>

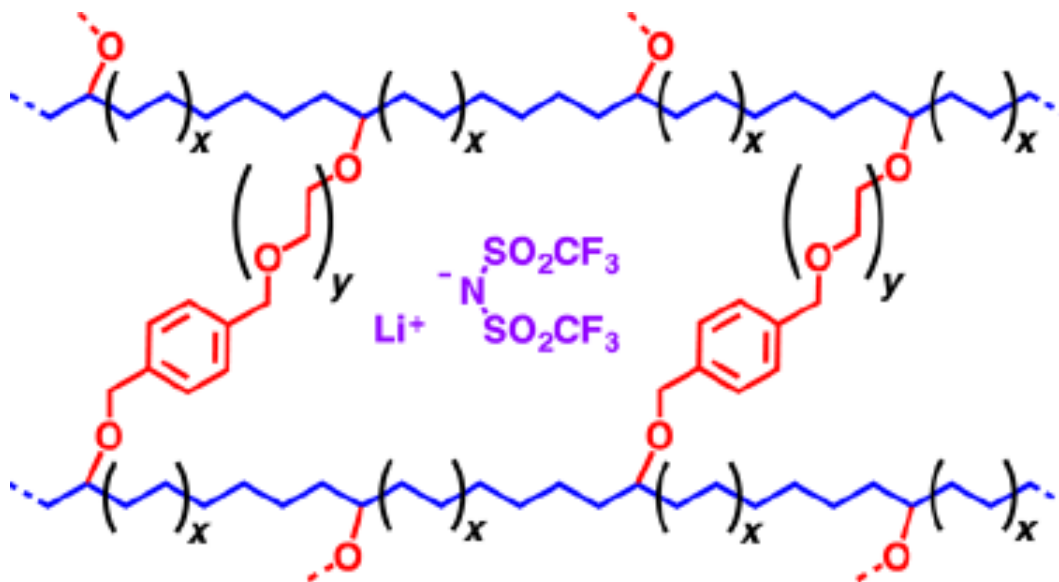


**Figure 1.16** Chemical structure of crosslinked PE/PEO electrolyte with the LiTFSI salt.<sup>43</sup>

#### *Addition of ceramic fillers*

In addition to the approach of forming crosslinked or blocked copolymers in SPEs, adding ceramic fillers into the polymer matrix is another effective approach to promote the local amorphous regions of PEO polymer while could still maintain the high mechanical strength and large electrochemical stability window of SPEs.<sup>37</sup> As has been reported in many studies, the fillers can be either non- $\text{Li}^+$ -conductive nanoparticles like  $\text{Al}_2\text{O}_3$ ,<sup>44</sup>  $\text{ZrO}_2$ ,<sup>45</sup>  $\text{SiO}_2$ ,<sup>46</sup>  $\text{TiO}_2$ <sup>47</sup> and organic polymer sphere<sup>36</sup>, or  $\text{Li}^+$ -conductive nanoparticles such as  $\text{Li}_{0.33}\text{La}_{0.557}\text{TiO}_3$  (LLTO),<sup>33</sup>  $\text{Li}_{1.3}\text{Al}_{0.3}\text{Ti}_{1.7}(\text{PO}_4)_3$  (LATP)<sup>48</sup> and  $\text{Li}_7\text{La}_3\text{Zr}_2\text{O}_{12}$  (LLZO).<sup>32</sup> Adding fillers in SPEs can

significantly contribute to the increase of ionic conductivity by increasing the amorphous region in polymer matrix and improving the conductive interface between fillers and polymers.

Das *et al.* studied the ion conduction of PEO-LiTFSI polymer electrolyte with the addition of Al<sub>2</sub>O<sub>3</sub> filler.<sup>49</sup> It is found that adding the Al<sub>2</sub>O<sub>3</sub> fillers into the PEO matrix can suppress the crystallinity of PEO and a maximum amorphous phase of PEO could be observed with a high ionic conductivity of  $\sim 3.3 \times 10^{-4} \text{ S cm}^{-1}$  when 5 wt.% Al<sub>2</sub>O<sub>3</sub> was added. Except for simply blending ceramic fillers with the polymers, Lin *et al.* introduced an *in-situ* synthesis of SiO<sub>2</sub> nanoparticles in the PEO matrix.<sup>50</sup> Much stronger chemical and mechanical interaction can be observed between the PEO polymer and SiO<sub>2</sub> nanoparticles, which consequently suppressed the crystallinity of PEO and improved the dissociation of Li salt. A high ionic conductivity of  $1.2 \times 10^{-3}$  at 60 °C and  $4.4 \times 10^{-5} \text{ S cm}^{-1}$  at 30 °C could be observed. In addition, a large electrochemical stability window up to 5.5 V verse Li<sup>+</sup>/Li was also obtained. Figure 1.17 indicates the schematic illustration of this study indicating that the crystalline nature of PEO is changed by the *in-situ* synthesis of SiO<sub>2</sub> in the polymer matrix.

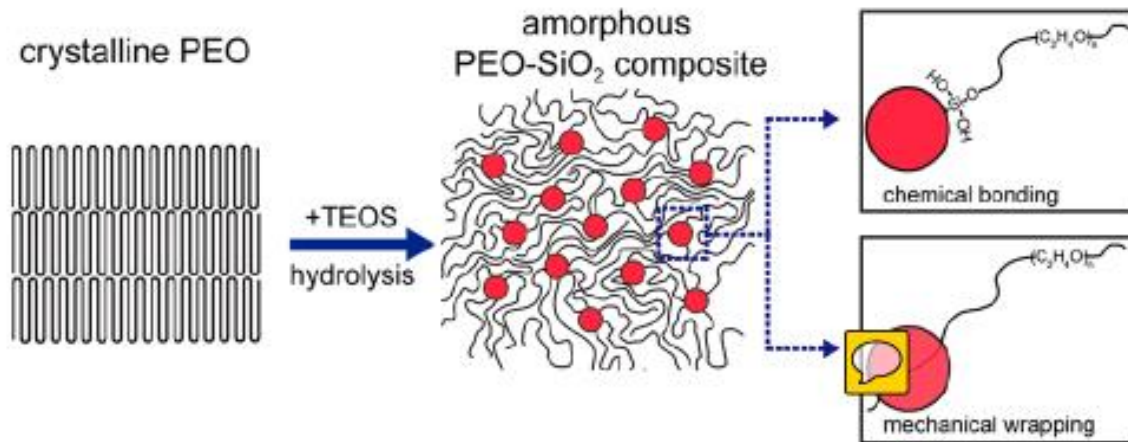


**Figure 1.17** Schematic illustration of the procedure of in-situ synthesis and the interaction mechanisms between SiO<sub>2</sub> nanoparticles and PEO chains.<sup>50</sup>

Moreover, in addition to the nanoparticle fillers which can only provide particle-particle junction in polymer matrix, 1D nanofibers with high aspect ratio can create continuous ionic transport pathways.<sup>32</sup> In this respect, Fu *et al.* developed a 3D Li<sup>+</sup>-conducting network based on the garnet-type Li<sub>6.4</sub>La<sub>3</sub>Zr<sub>2</sub>Al<sub>0.2</sub>O<sub>12</sub> (LLZO) nanofibers lithium ion conductor. The interconnected LLZO network in PEO polymer matrix can provide a continuous Li<sup>+</sup> conducting channels. Figure 1.18 indicates the schematic illustration of this design.<sup>32</sup> The incorporation of ceramic LLZO nanofibers as the filler has many advantages as it has a high ionic conductivity of around 10<sup>-3</sup> S cm<sup>-1</sup>, good chemical stability against Li metal, air and moisture. Therefore, as combined advantages of this 3D architecture, a high ionic conductivity of 2.5 × 10<sup>-4</sup> S cm<sup>-1</sup> at room temperature could be obtained with good thermal stability and effective lithium dendrites suppression.

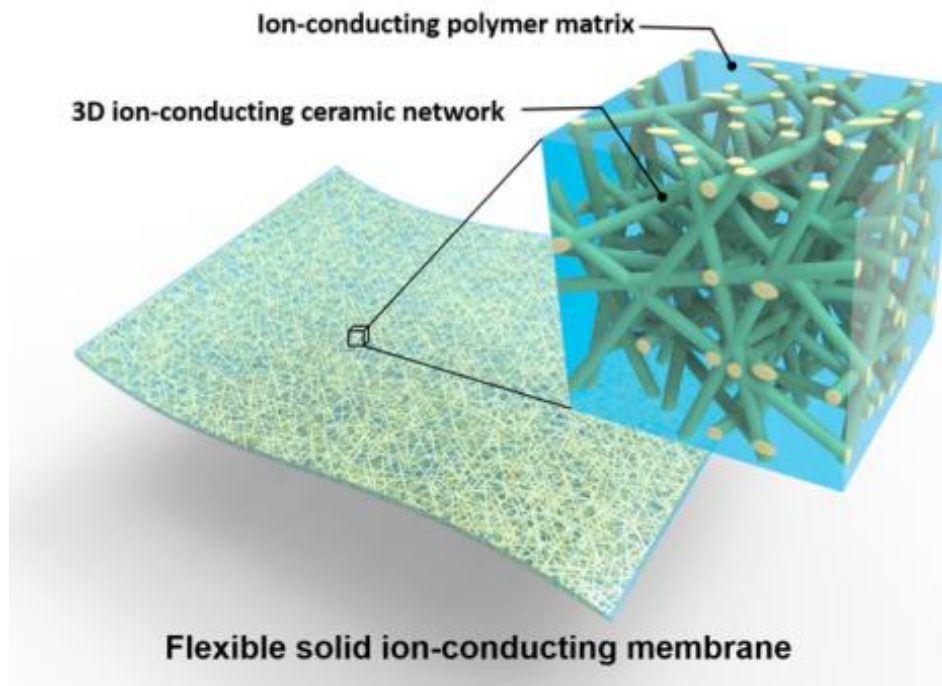


**Figure 1.18** Schematic of 3D LLZO/PEO solid composite electrolyte.<sup>32</sup>

## 1.4.2 Solid State Electrolytes Enabled All-Solid-State Lithium-Sulfur Batteries

### 1.4.2.1 Motivation for All-Solid-State Lithium-Sulfur Batteries

As has been mentioned above, the practical application of Li-S batteries is severely hindered by the polysulfide shuttle and although progressive breakthroughs have been made in S cathode structure design as well as separator modification/selection, it is still technically impossible to totally avoid the shuttle effect as the polysulfides has an excellent solubility in organic liquid electrolyte.<sup>3,29</sup> Solid electrolytes are promising to replace the traditional organic liquid electrolyte due to the ability in blocking polysulfide and lithium dendrite growth, along with the higher thermal stability, which could satisfy the demands of safe operation in Li-S batteries.<sup>31</sup> Recent

researches have been focused on integrating solid electrolyte into Li-S cells to form ASSLSBs.<sup>11</sup> The advantages of ASSLSBs lie in the improved safety by using nonflammable inorganic solid electrolyte and the increase of energy density due to the minimized polysulfide shuttle.

#### 1.4.2.2 Challenges of ASSLSBs

The reported electrochemical performance of ASSLSBs are still not comparable with the conventional liquid electrolyte Li-S cells in terms of S utilization and rate performance. The poor performance of ASSLSBs mainly comes from the challenges listed below: *i*) poor electrical and ionic conductivity of S and its discharge products; *ii*) low ionic conductivity of solid polymer electrolyte at room temperature; *iii*) ineffective contact of solid-solid interfaces; and *iv*) the volumetric expansion of S cathode during lithiation/delithiation.

#### 1.4.2.3 Approaches to Address the Problems in ASSLSBs

Inspired by the success of liquid electrolyte Li-S batteries in improving the electrical conductivity of S cathode, various conducting carbon-based materials including carbon black (C65),<sup>51</sup> carbon nanofibers (CNFs),<sup>52</sup> graphene<sup>53</sup> and mesoporous carbon<sup>54</sup> have been used in ASSLSBs. For example, Yamada *et al.* combined S with CNFs to fabricate conductive cathode for Li<sub>3</sub>PS<sub>4</sub> solid electrolyte enhanced ASSLSBs.<sup>52</sup> Owing to the good electrical conductivity provided by CNFs, the ASSLSBs could obtain a high capacity approaching the theoretical capacity of S with an excellent coulombic efficiency of 99% at initial cycles.

However, even though the capacity of ASSLSBs could be increased to some extent in the initial several cycles, the long-term cycling performance and the rate capabilities of the as-assembled cells are still not ideal in the previously mentioned study. Therefore, it seems that simply improve the electrical conductivity of the S cathode is not enough for achieving high performance ASSLSBs as the electrochemical redox reactions of active materials also requires for fast facial ion transport of  $\text{Li}^+$ . In this respect, increasing the ionic conductivity of S cathode is essential to improve the overall electrochemical performance of ASSLSBs.

Han *et al.* fabricated a mixed-conductive lithium sulfide ( $\text{Li}_2\text{S}$ ) nanocomposite by a bottom-up method for high performance ASSLSBs.<sup>27</sup> The active material  $\text{Li}_2\text{S}$  was first dissolved in ethanol solvent and was then mixed with the carbon precursor polyvinylpyrrolidone (PVP) and solid electrolyte  $\text{Li}_6\text{PS}_5\text{Cl}$  (both pre-dissolved in ethanol). Then a co-precipitation was applied to the above mixture.  $\text{Li}_2\text{S}$  nanocomposite was obtained after carbonization at high temperature. The whole experimental process is demonstrated in Figure 1.19. This novel preparation process of cathode material has incomparable advantages as it can provide a balanced electrical/ionic conductive matrix with good lithium storage capabilities for ASSLSBs. The all-solid-state Li-S cells with this homogeneous nanocomposite electrode could deliver a large reversible capacity of  $830 \text{ mAh g}^{-1}$  at  $50 \text{ mA g}^{-1}$  over 60 cycles, corresponding to a high active material utilization of 71%.

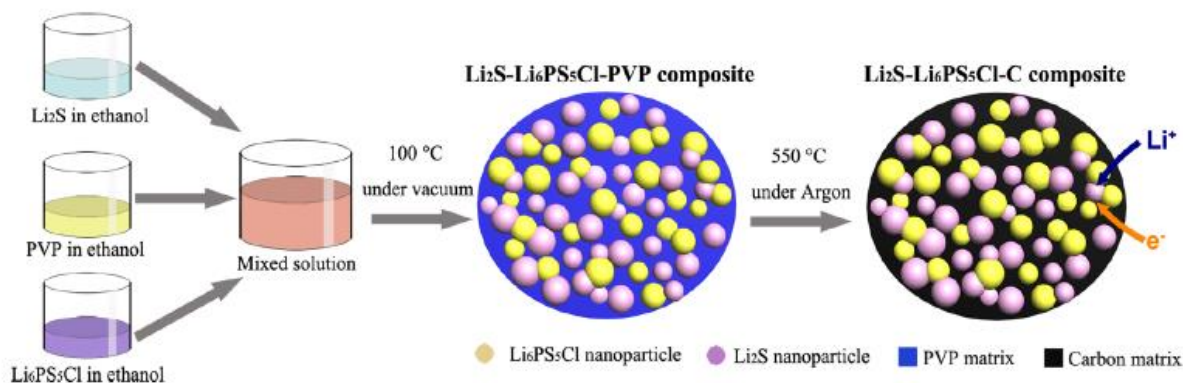


**Figure 1.19** Schematic illustration of the one-pot synthesis of the mixed conducting  $\text{Li}_2\text{S}$  cathode.<sup>27</sup>

From the above-reviewed literatures, it can be concluded that the properties of solid polymer electrolytes (*e.g.* ionic conductivity, electrochemical stability window etc.) and S cathode (balanced conductive matrix), play important potential roles in improving the electrochemical performance of ASSLSBs. Large improvements have been obtained in SPEs and S cathodes with those efforts reviewed above, which open avenues for the future developments in ASSLSBs. However, future work should still be focused on the advanced structural designs of SPEs and cathode with the aim of getting effective combinations of the high performance SPEs and dual-conductive cathodes for operation at room-temperature, which is the crucial part for the practical applications of ASSLSBs in e-bikes or EVs since the mostly reported ASSLSBs in literatures are still performing at high temperatures above 60 °C.

## **CHAPTER 2            RESEARCH OBJECTIVES**

This dissertation focuses on exploring and designing advanced separators/electrolytes for high-performance liquid/solid electrolyte Li-S batteries, with the aim of improving the electrochemical performance of Li-S cells while enabling the safe operation. The main research topics include:

### **2.1 Reduced Graphene Oxide Modified Glassfiber Separator for Lithium-Sulfur Batteries**

As we all know, the separator plays a crucial role in batteries as it separates the cathode from the anode to avoid electrical short circuit and help transport ions. In addition, as a key component relating to the safe operation in batteries, the separator should also be thermally stable with minimum dimensional change. The ideal separator for Li-S batteries should not only have all the properties mentioned above, but also help suppress the diffusion of polysulfides. Reduced graphene oxide (rGO), with its high electrical conductivity, two-dimensional (2D) wrinkled structure and appreciate oxygen containing groups, is able to reduce the internal resistance as well as to block the diffusion of polysulfides, thus enhancing the electrical performance of Li-S batteries. Here, rGOs with different reduction degrees were selected and used as the polysulfide inhibitor and were coated onto the glassfiber separators to minimize the shutting of polysulfides. The experimental results indicated that the incorporation of rGO coating with higher reduction degree largely minimized the polysulfide shutting, which was supported by the electrochemical performance of Li-S cells and further confirmed by the surface morphology study of the cycled separator. Therefore, it is demonstrated that this work opens an alternative avenue in rGO selection for high-performance Li-S batteries.

## **2.2 A Novel Bi-functional Double Layer rGO-PVDF/PVDF Nanofiber Membrane for High-Performance Lithium-Sulfur Batteries**

Electrospun nanofiber membranes have gained considerable research attention as potential separators for Li-S batteries because of their high specific surface area and high porosity, which demonstrate unparalleled advantages in electrolyte uptake and ion transport. Besides, due to its good wettability, ideal mechanical strength and excellent chemical/thermal stability, polyvinylidene fluoride (PVDF) polymer-based nanofiber membranes have been extensively studied for use in lithium-ion batteries. Here, combining the advantages of micro-porous PVDF nanofiber membranes and highly electrical conductive rGO, we introduced a novel, bi-functional double-layer rGO-PVDF/PVDF membrane for high-performance Li-S batteries. The advantages of this double-layer membrane lies in: *i*) the porous PVDF nanofiber framework in both rGO-PVDF and PVDF layer provides good thermal stability and maintains the structural integrity of the separator; and *ii*) the conductive rGO-PVDF layer serves as the polysulfide inhibitor and ensures the fast transfer of lithium ions. The electrochemical results demonstrate that this new double-layer rGO-PVDF/PVDF composite membrane separator provides a general strategy in dealing with multiple challenges in Li-S batteries.

## **2.3 $\text{Li}_{0.33}\text{La}_{0.557}\text{TiO}_3$ Ceramic Nanofiber-Enhanced Polyethylene Oxide-based Composite Polymer Electrolyte for All-Solid-State Lithium Batteries**

Although progressive improvements have been made in liquid electrolyte Li-S batteries with structural designs of cathodes and separators to suppress the diffusion of polysulfides and enhance

the electrochemical performance of Li-S batteries, it is still technically impossible to totally avoid the polysulfide diffusion. In addition, the safety problems originating from the flammable liquid electrolyte as well as the lithium dendrite formation also challenge the practical use of liquid electrolyte Li-S batteries.

Replacing the liquid electrolyte with solid electrolyte is promising for the practical application of Li-S batteries as it can lead to consistent improvements in electrochemical performance of cells with safe operation. Here, a polyethylene oxide (PEO)-based composite solid polymer electrolyte filled with one-dimensional (1D) ceramic  $\text{Li}_{0.33}\text{La}_{0.557}\text{TiO}_3$  (LLTO) nanofibers was designed and prepared. The incorporation of LLTO nanofibers in the PEO matrix has significantly decreased the crystallinity of PEO polymer, thus more amorphous region was created for the ion conduction. Besides, the 1D LLTO structure could also provide continuous/fast ionic pathways for the ion conduction. Thus, the as-prepared solid composite electrolyte showed a high ionic conductivity of  $2.4 \times 10^{-4} \text{ S cm}^{-1}$  at room temperature with a large electrochemical stability window up to 5 V vs.  $\text{Li/Li}^+$  and could satisfy most lithium-based batteries.

## **2.4 Flexible Electrolyte-Cathode Bilayer Framework with Stabilized Interface for Room-Temperature All-Solid-State Lithium-Sulfur Batteries**

All-solid-state Li-S batteries (ASSLSBs) has received intensive research attention because of their high energy density and enhanced safety, when compared to liquid electrolyte Li-S batteries. The key issues that restrict the application of ASSLSBs lie in the low ionic conductivity of solid

electrolytes, the insufficient contact between electrolyte/electrode interfaces and the poor electrical/ionic conductivity of S and its discharge products.

Here, a bilayer framework through integrating three-dimensional (3D) carbon nanofiber/sulfur (CNF/S) cathode with one-dimensional (1D) ceramic LLTO nanofiber incorporated solid electrolyte composite was prepared for room-temperature ASSLSBs. Benefiting from the novel bi-layer solid electrolyte/cathode architecture with the advantages of reduced interfacial resistance and enhanced interfacial stability between electrolyte/electrode interfaces, the formed fast and continuous long-range electron/ion transportation pathways within the 3D structure, as well as the excellent ability in polysulfide and lithium dendrite inhabitation, the ASSLSBs could be operated at RT without any liquid electrolyte addition and exhibited stable cycling performance with high Coulombic efficiency over 99% after 50 cycles.

## CHAPTER 3            REDUCED GRAPHENE OXIDE MODIFIED GLASSFIBER SEPARATOR FOR LITHIUM-SULFUR BATTERIES

### Abstract

Lithium-sulfur (Li-S) batteries are considered as a promising candidate for large-scale applications such as electrical vehicles (EVs) because of their high theoretical capacity, large energy density and low cost. However, due to the shuttling effect of polysulfides, the continuous capacity fading during cycling remains a substantial bumper for the practical use of Li-S batteries. Here, reduced graphene oxide (rGO) materials with different reduction degrees were used as the polysulfide inhibitor and were coated onto glass fiber separators to minimize the shuttling of polysulfides. The influence of reduction degree on the effort of polysulfide rejection was investigated. The incorporation of rGO coating with higher reduction degree largely minimized the polysulfide shuttling, thus the Li-S cells with separators modified with high-reduction degree rGO was able to maintain a capacity of 733 mAh g<sup>-1</sup> after 100 cycles and delivered a high capacity of 519 mAh g<sup>-1</sup> at 2C, which were 42% and 90% higher than those of cells with separators coated with low-reduction degree rGO. Therefore, it was found that rGO with higher reduction degree demonstrated better polysulfide rejection performance than rGO with lower reduction degree. This study provides a promising strategy in the rGO selection for high-performance Li-S batteries.

**Keywords:** Reduced graphene oxide; Reduction degree; Polysulfides; Lithium-sulfur battery

### 3.1 Introduction

Lithium-sulfur (Li-S) batteries have received great attention in the present scenario as an emerging energy storage systems in large scale applications like electrical vehicles (EVs) and electrical grids because of their large gravimetric energy density of  $2500 \text{ Wh kg}^{-1}$ , since sulfur (S) has an unparalleled theoretical capacity of  $1675 \text{ mAh g}^{-1}$ .<sup>1, 55-56</sup> However, the commercialization of Li-S batteries still has a long way to go because of their short cycle life, which is mainly caused by the severe shuttling effect of soluble reduction intermediate – “polysulfides” (PS).<sup>57-59</sup> The initial lithiation of S forms long-chain PS ( $\text{Li}_2\text{S}_n$ ,  $4 \leq n \leq 8$ ), which are soluble in organic electrolyte and can penetrate through the separator reaching the lithium (Li) anode side. Subsequently, the long-chain PS can further be lithiated into low-order short chain PS ( $\text{Li}_2\text{S}_n$ ,  $1 \leq n \leq 4$ ) with lithium sulfides ( $\text{Li}_2\text{S}/\text{Li}_2\text{S}_2$ ) depositing on the Li surface, which leads to continuous capacity fading and low active material utilization.<sup>5, 15</sup>

Structural design of S cathodes is one of the strategies to reduce the shuttling effect of PS, in which S is often encapsulated inside electrically-conductive carbon frameworks with/without micro-/mesopores and functional groups (e.g., oxygen containing groups, nitrogen groups, etc.).<sup>7, 60-65</sup> It is depicted that carbon frameworks act as the physical barrier to provide relatively closed environment and chemical interactions, *i.e.*, the interactions between the negatively-charged S-related species and functional groups in the carbon frameworks significantly minimize the PS diffusion, which in turn leads to improved cycling performance of Li-S cells. However, although progressive improvement has been achieved in Li-S batteries with those encapsulation methods

provided by conductive frameworks in S cathodes, it is still technically impossible to comprehensively avoid the PS diffusion in the cells with high S concentrations.

In addition to the structural design of sulfur cathodes, coating the separators with thin functional layers could be an effective approach to minimize the shuttling effect of PS. The conventional role of separators is to separate the cathode and the anode to prevent electrical short circuit while helping transport ions.<sup>6, 19, 66</sup> However, coated separators could also play a crucial role in relieving the PS migration by controlling the negatively-charged S-related species.<sup>67-68</sup> The using of graphene oxide (GO) as a coating material in Li-S batteries has been investigated since the rich functional groups in carbon framework could effectively trap the polysulfides. For example, Huang and his coworkers applied an ultra-thin graphene oxide (GO) membrane as a polysulfide shuttle inhibitor on the separator and a low capacity decay rate of 0.23% per cycle was obtained.<sup>69</sup> Zhang et al. improved the specific capacities of Li-S cell to 750 mAh g<sup>-1</sup> at 1C after 100 cycles with a GO/oxidized carbon nanotubes (O-CNT) coated separator.<sup>70</sup> Huang et al. used a highly porous GO/CNT film as an interlayer to prevent the polysulfide shuttle in Li-S batteries and a high reversible capacity of 671 mAh g<sup>-1</sup> after 300 cycles was achieved.<sup>71</sup> Shaibani et al. used a high-flux GO film to support the S cathode, the resultant Li-S cell delivered an impressive capacity retention with a high S utilization because of its highly-ordered structure as well as the inherent surface charge of the GO film.<sup>72</sup> In addition, reduced graphene oxide (rGO), which has been widely used in S cathodes and is prepared by the reduction of graphene oxide (GO), is another promising material for coating the separators since it is a two-dimensional (2D) structure material with preeminent electrical conductivity and surface-to-volume ratio.<sup>73</sup> Depending upon the degree of reduction, rGO can be obtained with various oxygen concentrations and surface areas.<sup>74</sup> It has been

reported that, the flexible and conductive rGO sheet as a current collector in S cathodes or as an interlayer could not only suppress the PS diffusion effectively, but also reduce the large volume changes of S during lithiation/de-lithiation.<sup>75-77</sup>

Therefore, having noticed the special role of the separator and the excellent functionality of rGO, in the present work, a thin rGO layer was incorporated onto the separator surface by a simple slurry coating method and the relationship between reduction degree of rGO and PS retardation was carefully explored. Results indicated that rGO with higher reduction degree is more effective in retarding the PS shuttling, which is fully supported by the electrochemical performance of Li-S cells with separators coated by rGO layers of different reduction degrees and the morphological characterization of these separators after cycling. The cells with high-reduction degree rGO-coated separator maintained a capacity of 733 mAh g<sup>-1</sup> after 100 cycles and delivered a high capacity of 519 mAh g<sup>-1</sup> at 2C, which were 42% and 90% higher than those of cells with low-reduction degree rGO-coated separator. This study demonstrates a promising strategy in the rGO selection for high performance Li-S batteries.

## 3.2 Experimental

### 3.2.1 Preparation of rGO Coated Separators

Two different rGO powders were received from Standard Graphene and their oxygen contents were 15.73% and 37.41%, respectively. They were labeled as rGO-1 and rGO-2. For the fabrication of rGO coated separators, 70 wt% rGO and 30 wt% polyvinylidene fluoride (PVDF, Solef<sup>®</sup> PVDF-5130, Solvay) were mixed together in N-methyl-2-pyrrolidone (NMP, Sigma-Aldrich), which were then casted onto the surface of the glassfiber membrane (GF, Whatman<sup>®</sup>) via doctoral blade. The as-obtained rGO coated GF separators, denoted as GF/rGO-1 and GF/rGO-2, were kept in the vacuum oven at 60 °C overnight to evaporate the solvent.

### 3.2.2 Structure Characterization

A field-emission scanning electron microscopy (FE-SEM, FEI Verios 460L, USA) with an energy dispersive X-ray spectroscopy (EDS) was used to characterize the surface and cross-sectional morphology of the rGO coated separators. X-ray diffraction (XRD) patterns of rGO-1 and rGO-2 powders were determined by Rigaku D/Max 2400 (Japan) with Cu K $\alpha$  radiation ( $\lambda=1.5418 \text{ \AA}$ ) in a 2-Theta angle of 10 to 60 degree. Brunauer-Emmett-Teller (BET) surface area measurements were performed using nitrogen (N<sub>2</sub>) adsorption by ASiQ Micropore Instrument to determine the specific surface areas of rGO-1 and rGO-2. Elemental analysis was performed by a Perkin Elmer 2400 CHNS Analyzer to determine the C, H, O and N contents of rGO-1 and rGO-2. The electrical conductivity of two rGO samples were measured by film four-point probe test.<sup>78-79</sup> X-ray

photoelectron spectroscopy (XPS, SPECS FlexMod, Germany) spectra of rGO-1 and rGO-2 were recorded with Mg K $\alpha$  radiation.

### 3.2.3 Electrode Fabrication and Cell Assembly

The working electrode was fabricated by mixing 70 wt% sulfur (S, Sigma-Aldrich), 20 wt% carbon black (C65, TIMCAL Graphite & Carbon Ltd.) and 10 wt% PVDF in a certain amount of NMP to form a uniform slurry. The mixture slurry was coated onto a carbon coated aluminum foil by doctor blade and dried in a vacuum oven at 60 °C overnight. Lithium metal foil was used as the counter electrode and the electrolyte used here was prepared by mixing 1 M bis(trifluoromethane) sulfonamide lithium (LiTFSI, Sigma-Aldrich) with/without 0.1 M lithium nitrite (LiNO<sub>3</sub>, Sigma-Aldrich) in a mixture solvent of 1,2-dimethoxyethane (DME, Sigma-Aldrich) and 1,3-dioxolane (DOL, Sigma-Aldrich) (1:1 by volume). Coin-type 2032 Li-S cells with GF/rGO-1 and GF/rGO-2 separators were assembled in argon filled glove box. The S loading was around 0.8-1.1 mg cm<sup>-2</sup> and the electrode thickness was around 45-50  $\mu$ m. The amount of electrolyte in each coin cell was fixed at 40  $\mu$ L per 1 mg S.

### 3.2.4 Electrochemical Performance Characterization

The cycling performance of Li-S cells was tested by Arbin battery tester in a potential range of 1.7-2.8 V. Cyclic voltammetry (CV) tests were conducted by a Gamry Reference 600 device with a scan rate of 1 mV s<sup>-1</sup> with a potential range of 1.7-2.8 V. Electrochemical impedance

spectroscopy (EIS) tests were performed by Gamry Reference 600 device to reveal the internal resistance of the Li-S cells with different separators in a frequency range from 1 M Hz to 1 Hz at an AC voltage of 10 mV.

Several Li-S cells assembled with different separators were disassembled at the charged state in the argon filled glove box after cycling. The morphology and S mapping of separators toward the Li metal side after cycling were characterized by FESEM with an EDS detector.

### 3.2.5 Polysulfide Diffusion Test

A 0.1 M  $\text{Li}_2\text{S}_8$  solution was prepared by adding S and lithium metal into a blank electrolyte of 1 M LiTFSI with 0.1M  $\text{LiNO}_3$  in a mixture solvent of 1:1 DME + DOL under stirring at 80 °C for 24 h. For the diffusion test set up, the  $\text{Li}_2\text{S}_8$  solution was added to vials with open hole caps, which were then sealed with separators with/without rGO coatings. The vials were immersed upside down in the blank electrolyte, and the photograph of diffusion process after 30 min was taken by a camera.

## 3.3 Results and Discussion

### 3.3.1 Morphology and Structure Characterization

In this work, GF/rGO-1 and GF/rGO-2 separators were prepared by a simple slurry coating of rGO powders and PVDF binder with a weight ratio of 7:3. Figures 1a and b show plain-view SEM

images of GF/rGO-1 and GF/rGO-2 separators. It is seen that both separators had rough surface with numerous interconnected/overlapped rGO sheets and the rGO-1 showed a more porous surface morphology after drying in vacuum. The corresponding EDS mapping of elemental carbon (C) and oxygen (O) of GF/rGO-1 and GF/rGO-2 separators (top-view), shown in Figures 3.1c-f, demonstrated the uniform distribution of rGO sheets and the existence of C and O elements. As shown in Figures 3.1g and h, the thicknesses of rGO-1 and rGO-2 coatings were fixed at around  $22 \pm 2 \mu\text{m}$  and the coating density was around  $1 \text{ mg cm}^{-2}$  for both samples. Table 3-1 shows the corresponding elemental analysis results of rGO-1 and rGO-2. For both rGO-1 and rGO-2 powders, the elemental oxygen concentrations (15.73 % for rGO-1 and 37.41% for rGO-2) were much lower than their carbon concentrations (83.68% for rGO-1 and 62.05% for rGO-2). In addition, rGO-1 had higher carbon concentration than rGO-2 while rGO-2 had higher oxygen concentration. This indicated that compared with rGO-2, rGO-1 was electrically more conductive with a higher reduction degree. The electrical conductivity measurement results indicated that the electrical conductivities for rGO-1 and rGO-2 were 2.08 and  $0.64 \text{ S cm}^{-1}$ , respectively.

**Table 3-1** Elemental Analysis of rGO-1 and rGO-2.

Sample	C (wt.%)	H (wt.%)	N (wt.%)	O (wt.%)	Conductivity ( $\text{S cm}^{-1}$ )
rGO-1	83.68	<0.5	0.09	>15.73	2.08
rGO-2	62.05	<0.5	<0.04	>37.41	0.64

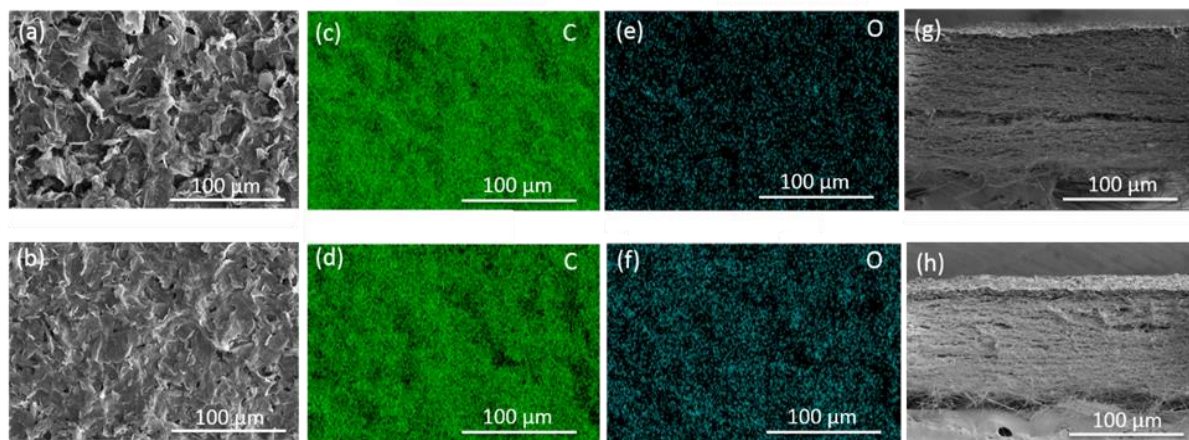


**Figure 3.1** Plain-view SEM images and corresponding C and O mapping of (a, c, e) GF/rGO-1, and (b, d, f) GF/rGO-2 separators. Cross-sectional SEM images of (g) GF/rGO-1 and (h) GF/rGO-2 separators.

Figure 3.2a shows the X-ray diffraction (XRD) patterns of rGO-1 and rGO-2. The XRD pattern of rGO-1 displayed two broad peaks at  $26.2^\circ$  and  $43.7^\circ$ , which could be ascribed to the (002) diffraction of graphite-layered structure and (100) diffraction of graphite, respectively.<sup>80</sup> The interlayer distance obtained from the (002) diffraction of rGO-1 was  $3.40 \text{ \AA}$ . Compared with rGO-1, rGO-2 indicated only one broad peak at  $24.2^\circ$  and the measured interlayer distance was  $3.68 \text{ \AA}$ . The observed peak shift of (002) plane and the expanded interlayer distance could be ascribed to the relatively rich oxygen containing groups of rGO-2.<sup>81</sup> The  $\text{N}_2$  isotherm adsorption curves indicated the BET surface area of these two rGO materials (Figure 3.2b). The results showed that rGO-1 and rGO-2 had similar BET specific surface areas of  $224.9$  and  $245.7 \text{ m}^2 \text{ g}^{-1}$ , respectively.<sup>82</sup> Figures 3.2c and d show the XPS spectra of rGO-1 and rGO-2. As expected, peaks related to O and C were detected in both powders. The relative intensity of O was much lower in rGO-1, which was consistent with the EDS mapping and elemental analysis results. It has been reported in

literature that the wrinkled structure of rGO sheets with high specific surface area and oxygen containing groups could provide physical adsorption and chemical absorption (electrostatic force between oxygen containing groups and negatively-charged S-related species), respectively, for polysulfide adsorption.<sup>69-72, 75-77</sup> However, the electrical conductivity of rGO powders is often lowered when the concentration of oxygen containing groups is high, which could also affect the overall electrochemical performance of Li-S cells as the conductive rGO coating on the separator surface also plays a role in lowering the cell internal resistance and increasing the active material utilization.<sup>6, 69-71, 74-76</sup> In this work, rGO-1 and rGO-2 powders with similar BET surface areas but different electrical conductivities and oxygen concentrations were selected, thus the difference in the electrochemical performance of the Li-S cells with GF/rGO-1 and GF/rGO-2 separators mainly come from the difference in the electrical conductivity and oxygen functional groups of those two rGO powders, which are the result of the different reduction degrees of rGO-1 and rGO-2.

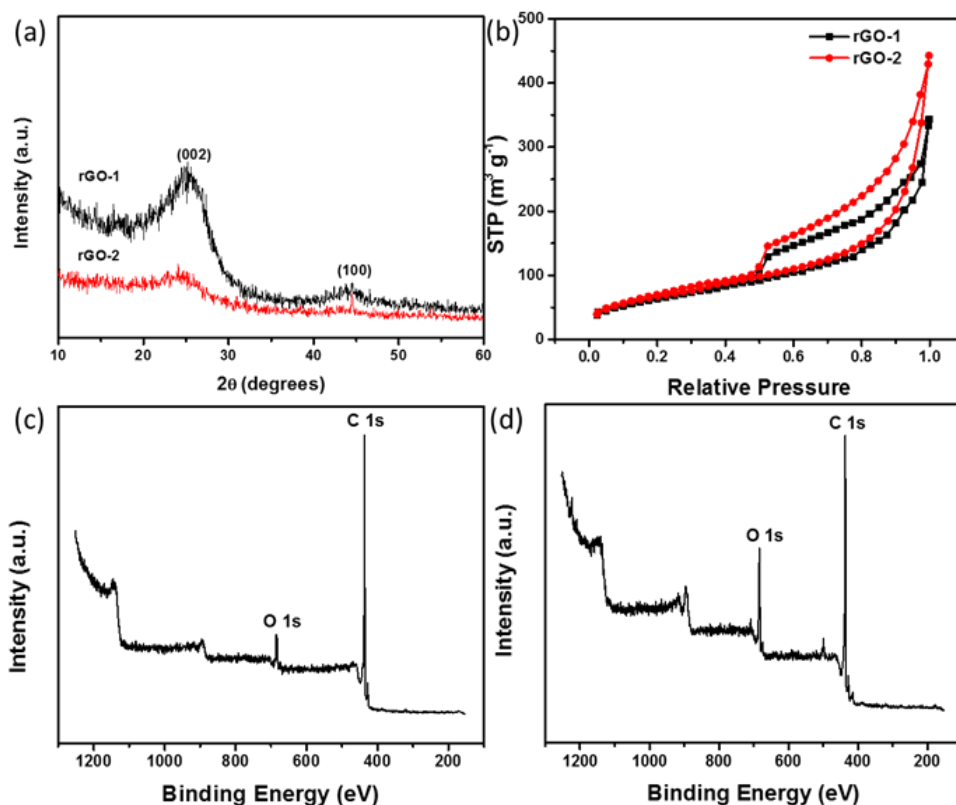


**Figure 3.2** (a) XRD patterns and (b) N<sub>2</sub> isothermal adsorption curves of rGO-1 and rGO-2. XPS spectra of (c) rGO-1 and (d) rGO-2.

### 3.3.2 Electrochemical Performance of Li-S Cells

The electrochemical performance of Li-S cells using GF/rGO-1 and GF/rGO-2 separators was evaluated. Bare GF separator was used as the control. Electrochemical impedance spectroscopy (EIS) tests were carried out to identify the influence of reduction levels of rGO on reducing the internal resistance of Li-S cells (Figure 3.3a). The diameter of the semicircle of the Nyquist plot in high frequency region represents the charge transfer resistance in Li-S cells.<sup>24, 68, 82</sup> Charge transfer resistance of the Li-S cell with bare GF separator was 44 Ω cm<sup>2</sup>. After the incorporation

of conductive rGO coating on the GF separator, the charge transfer resistance of the cells with GF/rGO-1 and GF/rGO-2 separators decreased to 23 and 26  $\Omega \text{ cm}^2$ , respectively. This indicates that the two rGO coatings on the surface of the GF separator provided multiple conductive sites and facilitated the charge transfer for the surface reactions, thus the Li-S cells with coated separators showed smaller resistances.<sup>73</sup> Besides, compared to the cell with GF/rGO-2 separator, the Li-S cell with GF/rGO-1 separator demonstrated smaller impedance, suggesting rGO-1 was more effective in minimizing the internal resistance. The reduced charge transfer resistance of the cell with GF/rGO-1 separator was probably due to the higher electrical conductivity of rGO-1 (2.08  $\text{S cm}^{-1}$ ) with a larger C/O ratio of 5.32, which is also supported by the XPS spectra that displayed a lower O intensity. In addition, as shown in Figure 3a, the cell with rGO-1 coating showed the smallest ohmic resistance ( $R_s$ ), which could be owing to the excellent electrical conductivity of rGO-1, serving as the second current collector and facilitating the electron transfer. Similar results was observed in Liao's work, in which they used rGO as a coating material in Li-S batteries.<sup>83</sup> Figures 3.3b-d showed the CV curves of Li-S cells with GF, GF/rGO-1 and GF/rGO-2 separators measured at a cutoff voltage of 1.7-2.8 V at a scan rate of 0.1  $\text{mV s}^{-1}$ . All the cells exhibited two cathodic peaks and one overlapped anodic peaks, which were typical for Li-S cells. The CV curves of Li-S cell with GF/rGO-1 separator presented a relatively lower reduction potential (peak potentials appeared at 2.31 V and 2.00 V) and a slightly higher oxidation potential (peak potential appeared at 2.43 V) while the peak shifted towards positive or negative potentials for the cells with GF and GF/rGO-2 separators, as shown in Figures b and d, indicating sluggish kinetic processes with higher polarization.<sup>84-86</sup> The excellent properties of the cell with GF/rGO-1 separator could be ascribed to the highly conductive rGO-1 with appropriate functional groups, which not only

facilitated the high rate charge transfer but also provided conductive sites for the reutilization of polysulfides.<sup>73</sup>

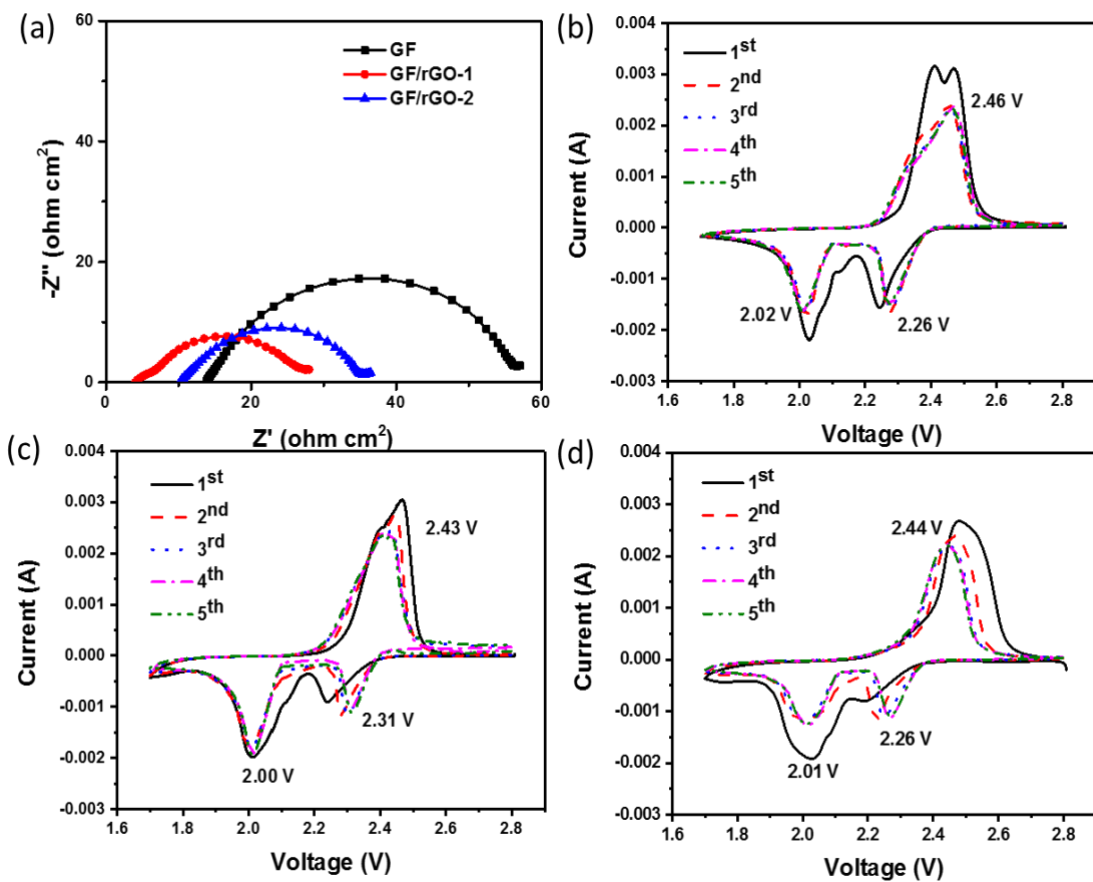


**Figure 3.3** (a) EIS curves of fresh Li-S cells with GF, GF/rGO-1 and GF/rGO-2 separators. CV curves of Li-S cells with (b) GF, (c) GF/rGO-1 and (d) GF/rGO-2 separators at a scan rate of 0.1 mV s<sup>-1</sup>.

To reveal the effect of reduction degree of rGO on polysulfide rejection, the electrochemical performance of the cells with GF, GF/rGO-1 and GF/rGO-2 separators was first evaluated without

using the well-known lithium metal surface protection additive of lithium nitrite ( $\text{LiNO}_3$ ) salt in the electrolyte.<sup>86</sup> Figures 3.4a-c show the discharge-charge profiles of the Li-S cells with GF, GF/rGO-1 and GF/rGO-2 separators. All the cells showed two typical discharge regions (first region: 2.4-2.1 V, representing the formation of long chain polysulfides; second region: 2.1-1.7 V, indicating the conversion of  $\text{Li}_2\text{S}_4$  to  $\text{Li}_2\text{S}_2$  or  $\text{Li}_2\text{S}$ ) and one closely packed charge region, which were consistent with the CV plots (Figures 3.3b-d).<sup>73, 82</sup> Furthermore, the polarization potential ( $\Delta E$ ), as shown in Figure 3.4a, determined by the voltage difference between the charge and discharge plateaus (second discharge region), of the bare GF separator based cell was 269 mV, which was further reduced to 118 mV and 217 mV for GF/rGO-1 and GF/rGO-2 cells, respectively, and was inconsistent with the CV curves (Figures 3.3b-d) that the cell with GF/rGO-1 separator had the smallest polarization potential. The reduced polarization potentials for the cells with two rGO coatings probably came from the smaller cell impedances, suggesting the efficient reaction process with smaller internal barriers. It is worth mentioning that the  $\Delta E$  of the cell with GF/rGO-1 separator was almost 32% lower than the cell with GF/rGO-2 separator, suggesting the efficient reaction process of the Li-S cell when GF/rGO-1 separator was used (Figures 3.4b and c). This is probably due to the smaller cell impedance coming from rGO-1 and the lower O concentration in carbon frameworks, decreasing the reaction barrier and facilitating the reaction process.<sup>73, 79</sup> Besides, in this electrolyte condition, all the cells exhibited an overcharging behavior because of the lack of  $\text{LiNO}_3$  in electrolyte with severe polysulfide shuttling.

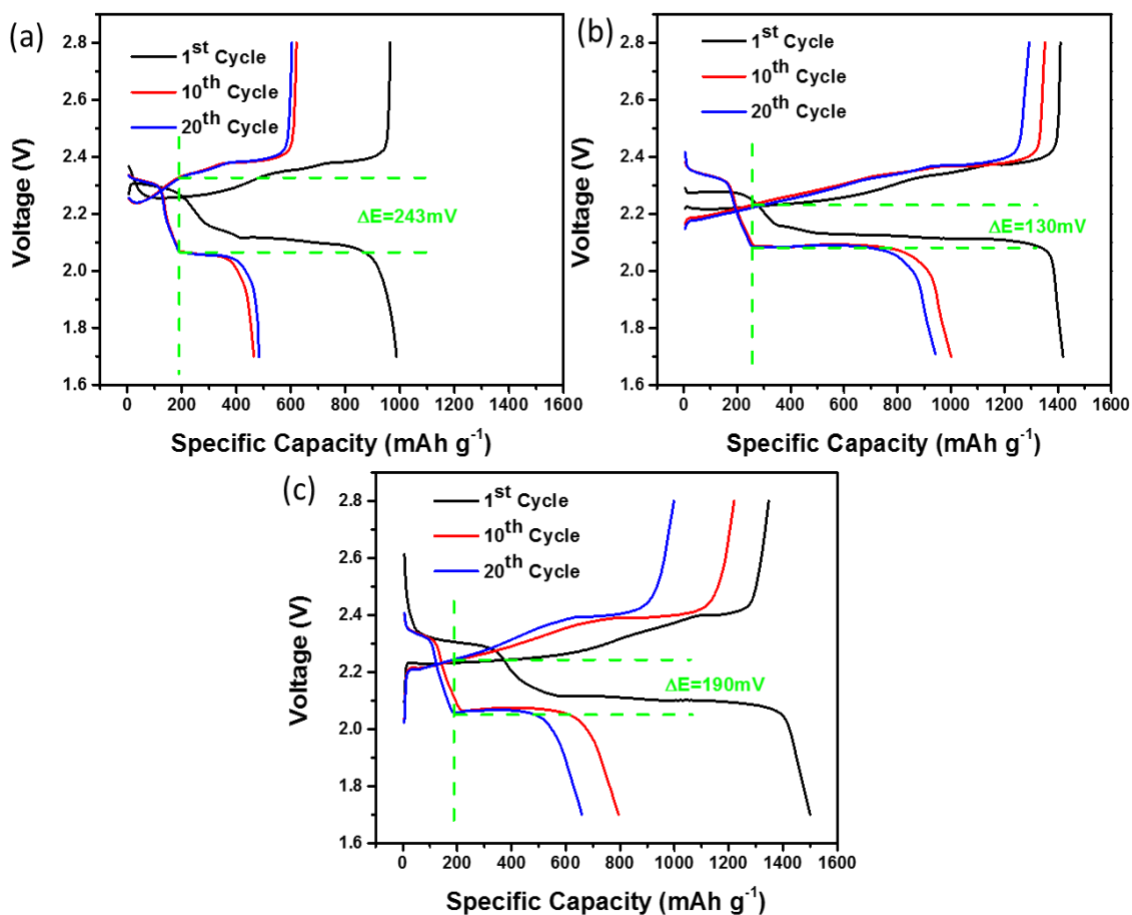


**Figure 3.4** Discharge-charge profiles of Li-S cells with (a) GF, (b) GF/rGO-1 and (c) GF/rGO-2 separators tested with electrolyte without the  $\text{LiNO}_3$  additive.

The specific capacity of the cell with bare GF separator started from  $987 \text{ mAh g}^{-1}$  in the first cycle and ended at  $489 \text{ mAh g}^{-1}$  after 40 cycles (Figure 3.5a). For the cells with GF/rGO-1 and GF/rGO-2 separators, the initial capacities increased to 1419 and  $1499 \text{ mAh g}^{-1}$ , respectively. However, the cell with GF/rGO-2 separator suffered from severe capacity decay and the capacity reduced to  $511 \text{ mAh g}^{-1}$  after 40 cycles. The cell with GF/rGO-1 separator showed the highest performance with a relatively high capacity of  $853 \text{ mAh g}^{-1}$  after 40 cycles, which was almost 74% and 69% higher

than those of the cells with GF and GF/rGO-1 separators, respectively. The prominent performance of Li-S cells with rGO-1 coated separator in the electrolyte without Li metal protector revealed the excellent functionality of rGO-1 in retarding polysulfides. Furthermore, without the presence of LiNO<sub>3</sub> salt, the cell with bare GF separator had a coulombic efficiency of 81% at the 40<sup>th</sup> cycle (Figure 3.5b). The coulombic efficiencies of cells with GF/rGO-1 and GF/rGO-2 separators were 83% and 71%, respectively, at the 40<sup>th</sup> cycle. The cell with GF/rGO-2 separator showed the lowest Coulombic efficiency probably because of the reaction of Li ions with the O-containing groups, such as carboxylic acid, epoxy, and hydroxyl groups, in rGO-2.<sup>87-88</sup> The low coulombic efficiency is coming from severe overcharging behavior during cycling, which is the symbolic process of polysulfide shuttle. Overall, it is clear that the GF/rGO-1 separator was more effective in blocking polysulfides and reducing the shutting phenomena.

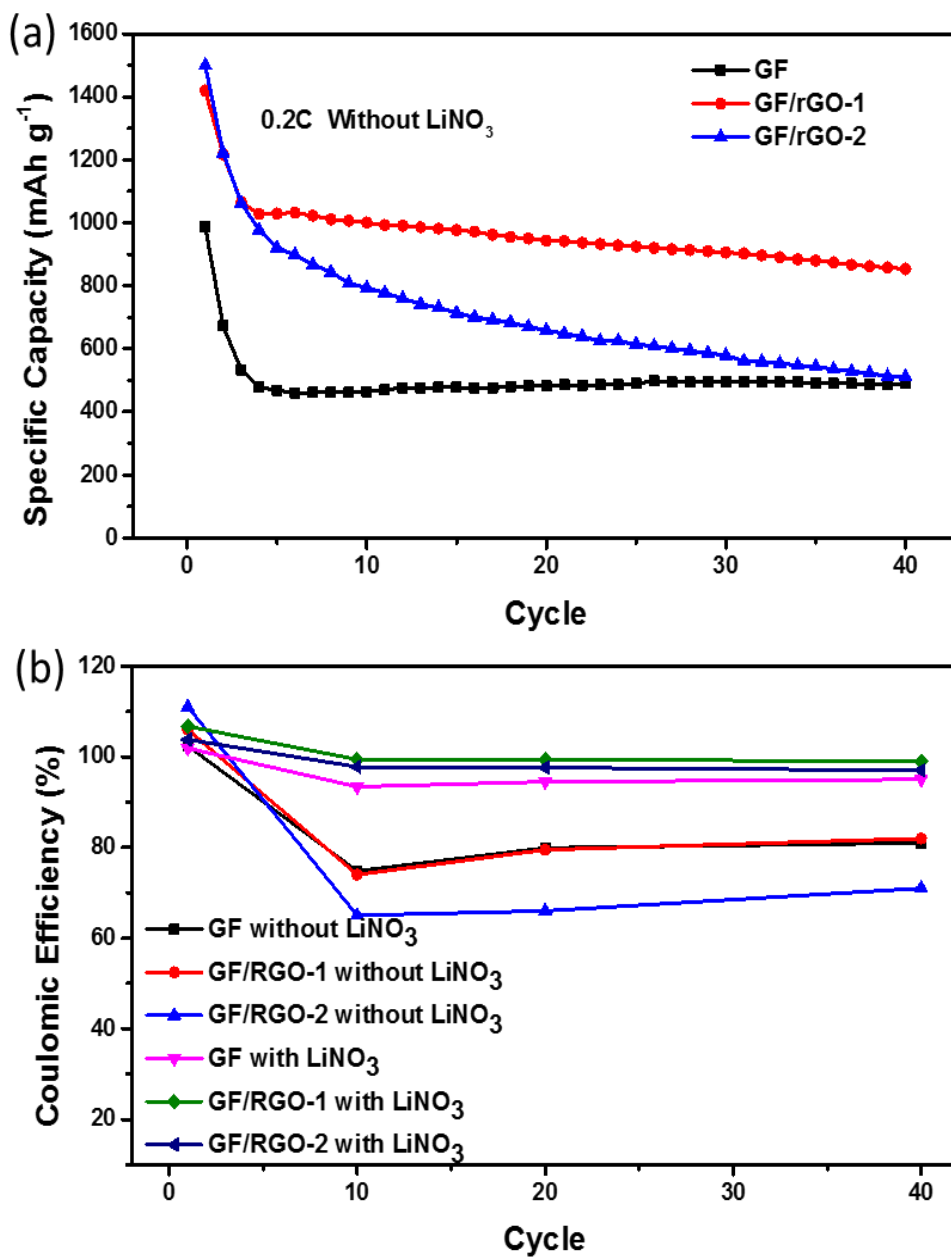


**Figure 3.5** (a) Cycle performance of Li-S cells with GF, GF/rGO-1 and GF/rGO-2 separators tested with electrolyte without LiNO<sub>3</sub> additive, (b) Coulombic efficiencies of Li-S cells with GF, GF/rGO-1 and GF/rGO-2 separators tested with/without the LiNO<sub>3</sub> additive.

The overcharging behavior of the cells was reduced significantly by adding  $\text{LiNO}_3$  salt in the conventional electrolyte solution. After using  $\text{LiNO}_3$ -add electrolyte, the coulombic efficiencies of the cells with GF, GF/rGO-1 and GF/rGO-2 separators increased to 95%, 99% and 97%, respectively, after 40 cycles (Figure 3.5b). Once again, the Li-S cells with rGO-1 coated separator showed the highest Coulombic efficiency as a result of the excellent functionality of rGO-1 and this prominent functionality was further demonstrated in the improved cycling performance and rate capabilities of Li-S cells. Figure 3.6a shows the long cycling performance of Li-S cells with three different separators after adding  $\text{LiNO}_3$  in the electrolyte solution. The initial capacities of the cells with GF, GF/rGO-1 and GF/rGO-2 separators were 1102, 1355 and 1472  $\text{mAh g}^{-1}$ , respectively. After 100 cycles, the cell with GF/rGO-1 separator could still deliver a high capacity of 733  $\text{mAh g}^{-1}$ , which was 56% higher than the cell with GF separator (470  $\text{mAh g}^{-1}$ ) and 42% higher than the cell with GF/rGO-2 separator (518  $\text{mAh g}^{-1}$ ).

It is worth mentioning that the cycling performance of the cell with GF/rGO-1 separator was quite stable as demonstrated in Figure 3.6a. On the other hand, the capacity of the cell with GF/rGO-2 separator kept on decreasing, which indicated its failure of rejecting polysulfides. In contrary, the GF/rGO-1 separator still maintained its excellent functionality in polysulfide blocking, and as a result the cell with GF/rGO-1 separator maintained the cycling stability. It is, therefore, demonstrated that rGO-1, with 15.73% oxygen concentration and 2.08  $\text{S cm}^{-1}$  electrical conductivity, not only provided physical and chemical adsorption for polysulfides, but also acted as a second current collector improving the active material utilization, thus exhibiting better performance in polysulfide rejection than rGO-2.<sup>69-72, 77</sup>

The rate capabilities of the cells with three separators are shown in Figure 3.6b. The cell with GF separator could deliver specific capacities of 581, 409 and 322 mAh g<sup>-1</sup> at current densities of 0.2C, 0.5C and 1C, respectively. For comparison, the cell with GF/rGO-1 separator showed much higher and stabilized capacities of 1155, 923 and 743 mAh g<sup>-1</sup> at current densities of 0.2C, 0.5C and 1C, respectively. On the other hand, when GF/rGO-2 separator was used, the capacities were 993, 637 and 429 mAh g<sup>-1</sup> at 0.2C, 0.5C and 1C, respectively, which were higher than those of the cell with bare GF separator but lower than those of the cell with GF/rGO-1 separator. Interestingly, when the current density was increased to 2C, the cell with GF/rGO-1 separator could still maintain a capacity of 519 mAh g<sup>-1</sup>, which was 169% higher than that of the cell with bare GF separator (193 mAh g<sup>-1</sup> at 2C) and 90% higher than that of the cell with GF/rGO-2 separator (273 mAh g<sup>-1</sup> at 2C). Remarkably, when the current density changed from 2C back to 0.2C, a high reversible capacity of 1016 mAh g<sup>-1</sup> could be achieved for the cell with GF/rGO-1 separator, implying a high retention of 88%, which was 104% and 20% higher than those of the cells with GF and GF/rGO-2 separators. The excellent rate capabilities of the Li-S cell with GF/rGO-1 separator can be ascribed to the excellent electrical conductivity of rGO-1 with higher reduction degree compared to rGO-2, serving as an upper current collector, which not only significantly increased the active material utilization but also effectively trapped the polysulfides from diffusing.

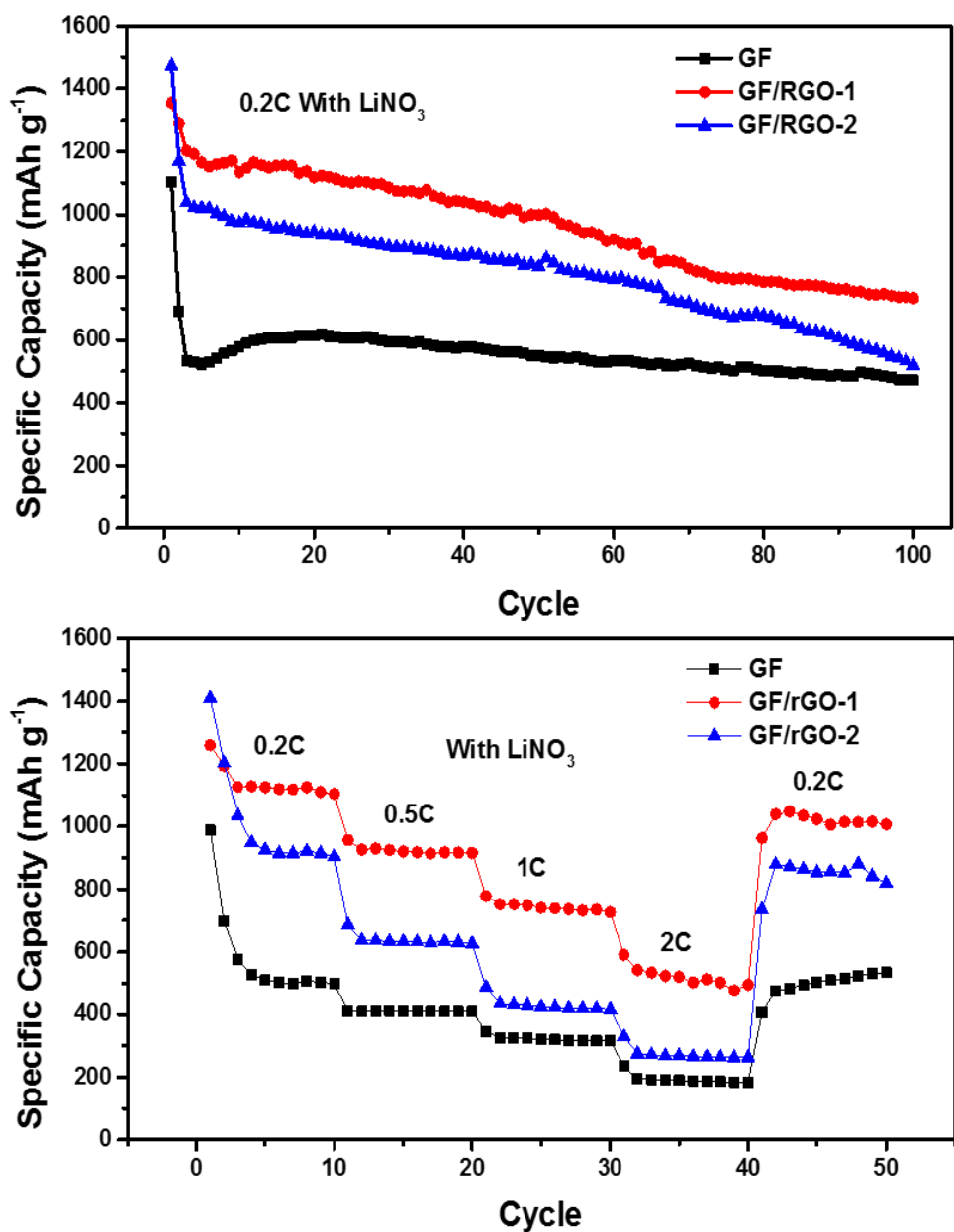


**Figure 3.6** (a) Cycling performance of the Li-S cells with GF, GF/rGO-1 and GF/rGO-2 separators with LiNO<sub>3</sub> additive at current density of 0.2C. (b) Rate capabilities of the Li-S cells with GF, GF/rGO-1 and GF/rGO-2 separators with LiNO<sub>3</sub> additive.

### 3.3.3 Evaluation of Polysulfides Rejection

To reveal the effect of reduction degrees of rGO on the effectiveness of polysulfide inhibition, Li-S cells with GF, GF/rGO-1 and GF/rGO-2 separators were disassembled in an argon-filled glovebox at the charged state after 100 charge-discharge cycles. The cycled separators were examined under SEM to study the changes of their surface morphologies on the Li metal side. As shown in Figure 3.7a, the surface of the GF separator was covered by S-related species, suggesting the poor ability of bare GF separator in trapping polysulfides, which was further confirmed by the strong S signal in EDS mapping (Figure 3.8d). However, when GF/rGO-1 and GF/rGO-2 separators were used, this phenomenon was alleviated and the surface morphologies could be maintained to some extent (Figures 3.7b-c) even though the S-related species still existed, which indicated the effective role of rGOs in trapping polysulfides. Besides, the performance difference within two rGO coated separators, when compared to bare GF separator, was also distinct. With higher reduction degree, GF/rGO-1 separator was more effective in trapping polysulfides, which was also reflected in the surface morphology and the relatively weak intensity of S signal in EDS mapping (Figures 3.7b and e). As discussed earlier, the rGO coating on the surface of the separator facing the cathode side with high specific surface area and oxygen containing groups could act as a barrier to confine the polysulfides between the cathode/separator while providing conductive sites for the reutilization of polysulfides. Hence, when rGO-1 with higher electrical conductivity and appropriate O containing groups was used, the polysulfides' shuttling was largely minimized.

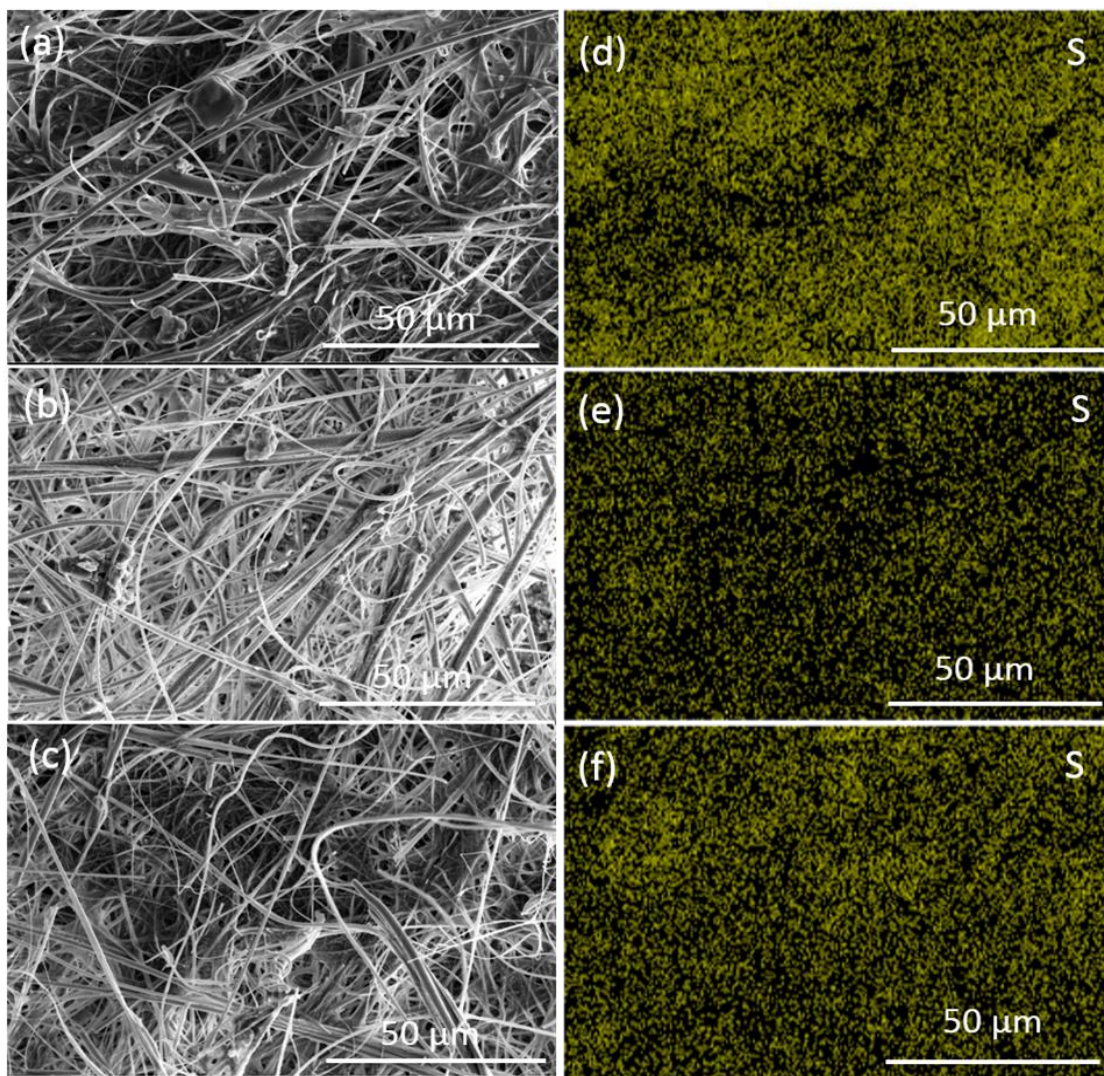


**Figure 3.7** SEM images of the cycled separators towards Li anode: (a) GF, (b) GF/rGO-1, (c) GF/rGO-2. Corresponding S mapping (d, e, f) of (a), (b) and (c), respectively.

In order to observe the polysulfide diffusion process through the separators, a simple diffusion test was conducted. In the test, a 0.1 M  $\text{Li}_2\text{S}_8$  solution was sealed in small vials with open hole caps using separators with/without rGO coatings. These vials were immersed upside down in the blank

electrolyte of 1 M LiTFSI with 0.1M LiNO<sub>3</sub> in a mixture solvent of 1:1 DME + DOL (Figure 3.8). It is seen that after 30 min, the blank electrolyte with the bare GF separator changed to dark yellow, indicating that a large amount of polysulfides had penetrated through the GF separator from the vial into the blank electrolyte. However, this phenomenon was alleviated when GF/rGO-1 and GF/rGO-2 separators were used. The electrolyte with GF/rGO-2 separator was light yellow. However, the electrolyte with GF/rGO-1 separator did not show observable color change after 30 min, demonstrating the excellent polysulfide blockage ability of rGO-1 coating. On one hand, the rGO-1 coating has excellent polysulfide blockage ability because of its porous structure/assembly morphology (as shown in Figures 1a and b) and the O containing groups, which offered strong physical and chemical adsorption for the negatively charged polysulfides. On the other hand, the enlarged interlayer spacing in rGO-2 (3.68 Å compared with 3.40 Å of rGO-1) as shown in XRD results may contribute to its better electrolyte wetting to some degree, which enhanced the polysulfide diffusivity. Those results were consistent with the electrochemical performance of Li-S cells and the morphological changes of separators after cycling.

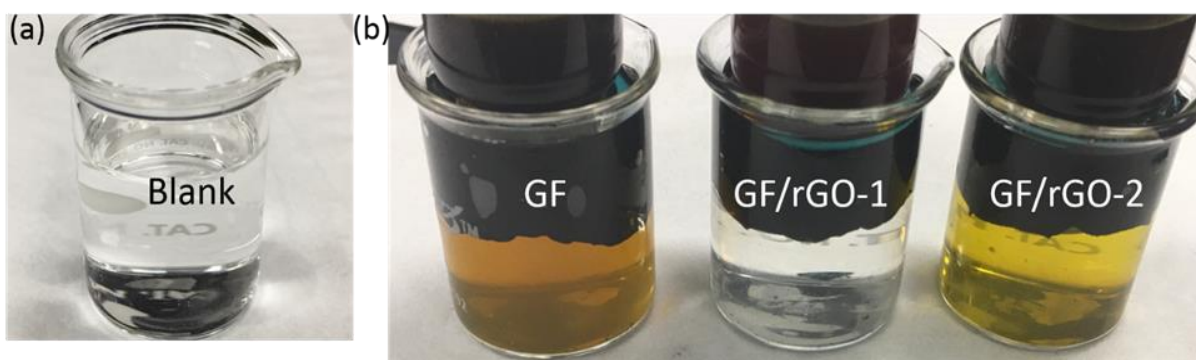


**Figure 3.8** Photo images of (a) blank electrolyte and (b) polysulfide diffusion model with GF, GF/rGO-1 and GF/rGO-2 separators after 30 min.

### 3.4 Conclusion

In summary, two different rGO powders with carbon concentrations of 84 wt.% and 62 wt.%, respectively, were carefully selected to explore the effect of rGO reduction degree on the performance of Li-S batteries. The rGO-1 powder with higher reduction degree exhibited better capability in rejecting polysulfides, which was supported by the electrochemical performance of Li-S cells with GF/rGO-1 separators and further confirmed by the surface morphology study of cycled GF/rGO-1 separator. Compared to other rGO based research, which seldom mentioned the reduction degree, this work opens an alternative avenue in rGO selection for high performance Li-S batteries.

**CHAPTER 4            A NOVEL BI-FUNCTIONAL DOUBLE-LAYER rGO-PVDF/PVDF  
NANOFIBER MEMBRANE FOR HIGH-PERFORMANCE LITHIUM-SULFUR  
BATTERIES**

**Abstract**

A novel, bi-functional double-layer reduced graphene oxide (rGO)-polyvinylidene fluoride (PVDF)/PVDF membrane was fabricated by a simple electrospinning technique and was used as a promising separator for lithium-sulfur batteries. This double-layer membrane separator delivers two different functionalities: *i*) the porous PVDF nanofiber framework in both rGO-PVDF and PVDF layers provides good thermal stability and maintains the structure integrity of the separator; and *ii*) the conductive rGO-PVDF layer serves as a polysulfide inhibitor and ensures the fast transfer of lithium ions. Compared to conventional polypropylene membrane separators, this new separator design can significantly enhance the cycling stability and rate capability of the incorporated lithium-sulfur batteries. Overall, it is demonstrated that this new double-layer rGO-PVDF/PVDF composite membrane separator opens an alternate avenue in the structural design of high-performance lithium-sulfur batteries in dealing with multiple challenges.

**Key Words:** reduced graphene oxide, PVDF, nanofiber, separator, thermal stability, lithium-sulfur batteries

## 4.1 Introduction

The lithium-sulfur (Li-S) battery is considered as a promising next-generation energy storage system because sulfur (S) has a high theoretical capacity of 1675 mAh g<sup>-1</sup> and Li-S cells have a large gravimetric energy density of 2500 Wh kg<sup>-1</sup>, which is nearly one magnitude higher than that of the currently commercialized lithium-ion batteries (with energy density of ~250 Wh kg<sup>-1</sup>).<sup>8, 57, 89-91</sup> Besides, S is abundant on the earth and is nontoxic.<sup>73, 77, 90, 92</sup> However, the practical implementation of Li-S batteries is hindered by the continuous fading of cell capacities, which is caused by the “shuttle effect” of soluble reduction intermediates, called “polysulfides”.<sup>93-96</sup> Normally, long chain polysulfides (Li<sub>2</sub>S<sub>n</sub>, 4 ≤ n ≤ 8) easily diffuse to the lithium anode through the separator and react with lithium forming a short chain polysulfides with solid-state low-order lithium sulfides (Li<sub>2</sub>S/Li<sub>2</sub>S<sub>2</sub>) depositing on the lithium surface, thus leading to low active material utilization.<sup>96-98</sup> Furthermore, safety issue has always been a main concern in Li-S batteries, especially in the practical applications such as electric vehicles (EVs) which require a wide temperature window to guarantee safe operation.<sup>4, 99-100</sup>

It is well known that separators play a critical role in batteries by separating the cathode from the anode to avoid electric short circuit and providing transport channels for ions.<sup>14, 24, 101</sup> In addition, as the key component relating to the safe operation of batteries, separators should be thermally stable with minimum dimensional change.<sup>19, 102</sup> An ideal separator of Li-S batteries should not only have the abovementioned properties, but also help suppress the diffusion of polysulfides.<sup>14, 19, 102</sup> Unfortunately, the widely-used commercial polypropylene (PP) membrane separators cannot satisfy many of the requirements for Li-S battery applications. To address these challenges, many efforts have been done on the cathode structure design with carbon frameworks and advanced

binder selections. The carbon frameworks have physical/chemical barrier functions and can reduce the diffusion of polysulfides, thus leading to an improved cycle stability.<sup>73, 77, 93, 95, 103</sup> Some polymer binders, especially recent reported advanced polar binders with polar groups and network structures such as amino functional group-containing polymers and graphene oxide-polyacrylic acid polymers, have also been found to not only provide physical adhesion between active materials and additives, but also offer strong binding energy for the absorption of polysulfides.<sup>104-105</sup> In addition, surface-modified PP membranes as well as functional interlayers have also been prepared by adding conductive carbon materials and/or ionic polymers to migrate the diffusion of polysulfides.<sup>14, 16, 77, 95, 97, 106-107</sup> Even though the cells with polar binders, carbon frameworks/coatings or interlayers show improved cycle stability with enhanced active material utilization, the rate capabilities are still not ideal because of the slow kinetics caused by the low porosity and poor wettability of PP.<sup>24</sup> The additional carbon coatings or interlayers also increase the total mass of the cells, which reduce the cell energy density. In addition, the low melting temperature of PP causes thermal instability and safety concern, which further restrict the potential application of Li-S batteries in high temperature operations. Therefore, it comes with a critical question: is there any simple and straightforward approach that can allow the safe operation of Li-S batteries at higher temperatures while at the same time, address the slow kinetic caused by PP membrane separators?

Electrospun nanofiber membranes have gained considerable attention as potential separators for batteries due to their high specific area and high porosity, demonstrating unparalleled advantages in electrolyte uptake and ion transport.<sup>20, 24, 101</sup> Various polymers have been used to prepare nanofiber membranes including polyacrylonitrile (PAN), polyvinyl chloride (PVC),

polyvinylidene fluoride (PVDF) and polyethylene oxide (PEO).<sup>23-24, 108</sup> Among these polymers, PVDF stands out for use in Li-based battery systems because of its good wettability, ideal chemical and mechanical stability as well as excellent thermal resistance.<sup>23, 109</sup> It has been reported that using PVDF nanofiber membrane as a polymer separator in lithium-ion batteries could significantly improve the thermal stability.<sup>110</sup> In addition, reduced graphene oxide (rGO), owing to its excellent electric conductivity and high surface area, has been reported to be able to block the migration of polysulfides which leads to an improved active material utilization.<sup>73, 77, 93</sup>

Here inspired by the abovementioned considerations, we report a novel bi-functional double-layer rGO-PVDF/PVDF nanofiber membrane separator which could potentially solve the continuous capacity fading problem while enabling high temperature safe operation. This novel double-layer structure design of porous rGO-PVDF/PVDF nanofiber composite membrane separator has two different advantages: *i*) the PVDF nanofiber framework in both rGO-PVDF and PVDF layers has good thermal stability and can help maintain the structure integrity of the separator; and *ii*) the conductive rGO-PVDF layer serves as a polysulfide inhibitor and ensures the fast transfer of lithium ions. Benefiting from the PVDF nanofiber framework and rGO incorporated layer, Li-S cells using this new separator can deliver significantly enhanced thermal safety with stable cycling performance.

## 4.2 Experimental

### 4.2.1 Membrane Preparation

PVDF ( $M_w$   $30 \times 10^4 - 50 \times 10^4$ , Shanghai Ofluorine Chemical Technology) solution (8 wt%) was prepared by dissolving 2 g PVDF powder in 23 g mixture solvent of dimethylformamide (DMF, 99.8%, Sigma-Aldrich)/acetone (99.5%, Sigma-Aldrich) (7:3 by volume) and kept overnight under stirring. For the preparation of rGO-PVDF solution, 0.2 g rGO (Standard Grapheen) was first dispersed in 23 g mixture solvent of DMF/acetone (7:3 by volume) under sonication. PVDF was then added to the rGO-dispersed solution and stirred overnight to form a homogenous 10 wt% rGO-PVDF solution with respect to the weight of PVDF.

The PVDF nanofiber membrane was prepared by electrospinning of the as-prepared PVDF solution at high voltage of 15 kV with a feeding rate of  $0.75 \text{ ml h}^{-1}$ . The thickness of PVDF nanofiber membrane was fixed at  $130 \pm 5 \text{ }\mu\text{m}$  by using a controlled amount of PVDF solution. Double-layer rGO-PVDF/PVDF membranes were prepared by electrospinning the rGO-PVDF solution directly onto an electrospun PVDF membrane. rGO-PVDF/PVDF membranes with two different rGO-PVDF layer thicknesses of  $75 \pm 5 \text{ }\mu\text{m}$  and  $95 \pm 5 \text{ }\mu\text{m}$  were prepared and they were denoted as rGO-PVDF/PVDF-1 and rGO-PVDF/PVDF-2, respectively. Both rGO-PVDF/PVDF-1 and rGO-PVDF/PVDF-2 membranes had the same thickness of  $130 \pm 5 \text{ }\mu\text{m}$ .

#### 4.2.2 Membrane Structure Characterization

The morphology of the nanofiber membranes was characterized by a field-emission scanning electron microscopy (FE-SEM, FEI Verios 460L, USA) with an energy dispersive X-ray spectroscopy (EDS) detector. X-ray diffraction (XRD) patterns were determined by Rigaku D/Max 2400 (Japan) with Cu K $\alpha$  radiation ( $\lambda=1.5418\text{\AA}$ ) in a 2-Theta range from 5° to 60° to identify the structure of the nanofiber membranes. The functional groups of the nanofiber membranes were analyzed by a Fourier transform-infrared spectroscopy (FT-IR, Thermo Scientific™ Nicolet™ iS™10). Elemental analysis was performed by a Perkin Elmer 2400 CHNS Analyzer to determine the C, H, O and N contents of rGO. The electrical conductivity of rGO was determined by film four-point probe test.<sup>36</sup> The porosity tests were carried out to investigate the porosities of the nanofiber membranes by using n-butyl alcohol uptake approach and calculated by the formula below:

$$Porosity(\%) = (w_w - w_d) / (\rho_b \times V) \times 100\% \quad (4.1)$$

where  $w_w$  is the weight of wet separator,  $w_d$  the weight of dry separator,  $\rho_b$  the density of n-butyl alcohol, and  $V$  the geometric volume of the separator.

The electrolyte uptake tests were determined by soaking separators (weighted before soaking) in the liquid electrolyte of 1 M bis(trifluoromethane) sulfonamide lithium (LiTFSI, 99.95% trace metals basis, Sigma-Aldrich) and 0.1 M lithium nitrite (LiNO<sub>3</sub>, 99.99% trace metals basis, Sigma-Aldrich) in a mixture solvent of 1,2-dimethoxyethane (DME, 99.5%,

Sigma-Aldrich)/1,3-dioxolane (DOL, 99%, Sigma-Aldrich) (1:1 by volume) for 2 h at room temperature. The electrolyte uptake values were calculated by:

$$\text{Electrolyte uptake(\%)} = (w_1 - w_0)/w_0 \times 100\% \quad (4.2)$$

where  $w_0$  and  $w_1$  are the weights of the separators before and after soaking in the electrolyte.

#### 4.2.3 Thermal Performance Evaluation

Thermal shrinkage tests were carried out to examine dimensional stability of the separators. The separators were soaked separately in vials containing a liquid electrolyte of 1 M LiTFSI and 0.1 M LiNO<sub>3</sub> in a mixture solvent of DME/DOL (1:1 by volume). The vials were kept in an oven at 80 °C for 24 h.

#### 4.2.4 Sulfur Electrode Fabrication and Cell Assembly

Electrochemical performances of coin-type 2032 Li-S cells with PVDF and rGO-PVDF/PVDF membrane separators were evaluated by various electrochemical tests. The working electrode was fabricated by coating a slurry of 70 wt% Sulfur (S, 99.5-100.5%), 20 wt% carbon black (C65, TIMCAL Graphite & Carbon Ltd.) and 10 wt% PVDF in N-methyl-2-pyrrolidone (NMP, 99%, Sigma-Aldrich) onto a carbon-coated aluminum foil. The coated electrode was dried under vacuum at 60 °C overnight and had a S loading of around 0.8-1.1 mg cm<sup>-2</sup>. The maximum S loading density was 1.1 mg cm<sup>-2</sup>. The electrolyte used in this study consisted of 1 M LiTFSI and 0.1 M LiNO<sub>3</sub> in

a mixture solvent of DME/DOL (1:1 by volume). The amount of electrolyte was controlled at 40  $\mu\text{L}$  per 1 mg sulfur. Lithium metal foil was used as the counter electrode.

#### 4.2.5 Electrochemical performance characterization

The cycling performance of the Li-S cells was tested in a potential range of 2.8-1.7 V by an Arbin battery tester. The cyclic voltammetry (CV) tests were conducted in a potential range of 2.8-1.7 V with scan rates of 0.1, 0.2 and 0.3  $\text{mV s}^{-1}$  by a Gamry Reference 600 device. Lithium-ion diffusion coefficients were measured by CV using the same Gamry Reference 600 device from 1 MHz to 1 Hz at an AC voltage of 10 mV at different scan rates. Electrochemical impedance spectroscopy (EIS) tests were carried out by Gamry Reference 600 to investigate the internal resistance of the assembled cells. After cycling tests, Li-S cells were disassembled at the charged state in an argon-filled glove box and the separators/lithium metal anodes were collected for further analysis. The morphological characterization and the EDS mapping of the separators (toward the Li metal side)/lithium metal anodes after cycling were carried out using FESEM with an EDS detector. All the capacities were calculated based on the mass of sulfur.

## 4.3 Results and Discussion

### 4.3.1 Morphology and Structure Characterization

The surface morphological features of PP, PVDF and rGO-PVDF membranes were characterized by FE-SEM. As shown in Figure 4.1, it is seen that the PP membrane exhibited a slit-like structure with microporous pores (Figures 4.1a and b). On the other hand, the as-spun PVDF membrane represented a porous network structure with micro/mesopores constructed by randomly distributed PVDF nanofibers (Figures 4.1c and d). Compared with pure PVDF membrane, the rGO-incorporated rGO-PVDF membrane showed a rough surface with wrinkled rGO sheets randomly accumulated and distributed in PVDF nanofibers (Figure 4.1e). The wrinkled structure of rGO sheets in the rGO-PVDF membrane is consistent with the rGO powder before being incorporate into the nanofiber matrix (Figure 4.1f). Both pure PVDF and rGO-PVDF composite membranes demonstrated a porous topography with combined nanofibrous network, which is beneficial for the organic electrolyte uptake and penetration.

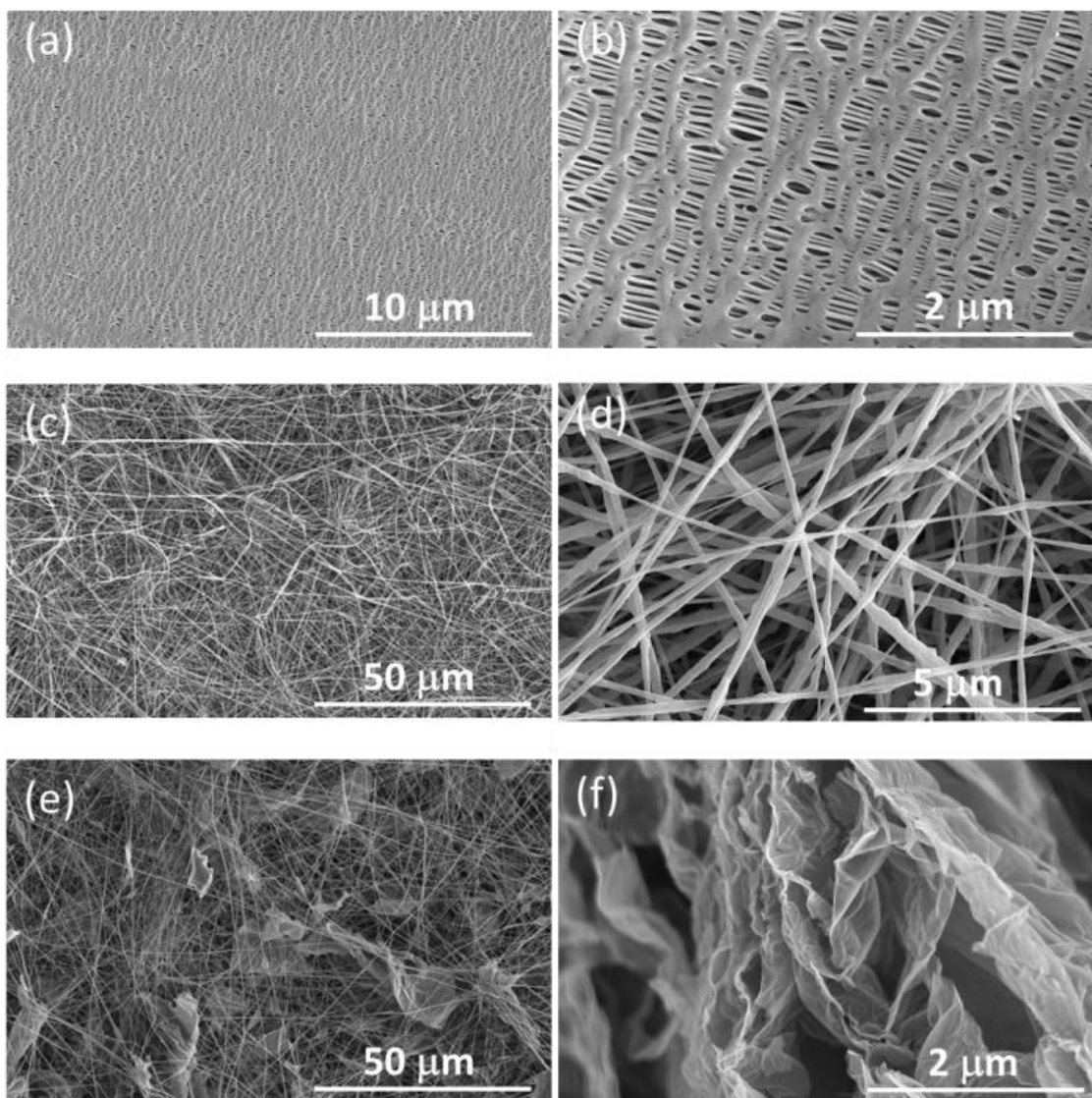


**Figure 4.1** SEM images of (a, b) PP membrane, (c, d) PVDF nanofiber membrane, (e) rGO-PVDF nanofiber composite membrane, and (f) rGO powder.

To minimize polysulfide diffusion and increase active material utilization, double-layer rGO-PVDF/PVDF separators were prepared by electrospinning an rGO-PVDF nanofiber composite layer onto a PVDF nanofiber membrane. This conductive composite layer could serve as a protective barrier to confine the polysulfides at the cathode/separator side and reutilize the

dissolved polysulfides. The individual thicknesses and the homogeneity of the rGO-PVDF and PVDF layers in the resultant double-layer rGO-PVDF/PVDF separators were investigated by analyzing the cross-sectional FESEM images of two different rGO-PVDF/PVDF composite membrane separators, i.e., rGO-PVDF/PVDF-1 and rGO-PVDF/PVDF-2, as shown in Figure 4.2. It could be clearly seen from the cross-sectional FESEM images that the double layer structure was achieved, where the rGO-PVDF was the top layer and PVDF was the bottom layer. The measured rGO-PVDF layer thicknesses were  $75 \pm 5$  and  $95 \pm 5$   $\mu\text{m}$  for rGO-PVDF/PVDF-1 and rGO-PVDF/PVDF-2, respectively. The total thicknesses of the as-prepared rGO-PVDF/PVDF-1 and rGO-PVDF/PVDF-2 membranes were around  $130 \pm 5$   $\mu\text{m}$ . For comparison, the pure PVDF nanofiber membrane studied in this work was controlled to the same thickness of  $130 \pm 5$   $\mu\text{m}$ .

The porosities and electrolyte uptakes of PP, PVDF, rGO-PVDF/PVDF-1 and rGO-PVDF/PVDF-2 membranes are shown in Table 4-1. PP membrane had a porosity of 45% with an electrolyte uptake value of 174% while PVDF membrane showed a porosity of 68% with 310% electrolyte uptake. After the incorporation of rGO-PVDF layer, the porosities and electrolyte uptake values were further increased to 70%, 354% for rGO-PVDF/PVDF-1 and 71%, 380% for rGO-PVDF/PVDF-2, respectively. As a result, the as-prepared rGO-PVDF/PVDF membranes could capture more electrolyte and thus ensuring the fast ion transfer between the cathode and the anode in Li-S batteries. The significantly increased electrolyte uptake values of rGO-PVDF/PVDF separator mainly came from the porous structure of PVDF nanofiber skeleton and the wrinkled rGO sheets. The Brunauer-Emmett-Teller (BET) specific surface area and pore size distribution of rGO was investigated by nitrogen ( $\text{N}_2$ ) isothermal adsorption (Figure 4.3). The rGO sheets exhibited a high BET surface area of  $345.831 \text{ m}^2 \text{ g}^{-1}$  with mesopores. This exposed surface area

and porous structure are beneficial for the electrolyte capture and the adsorption of polysulfides on rGO sheets.

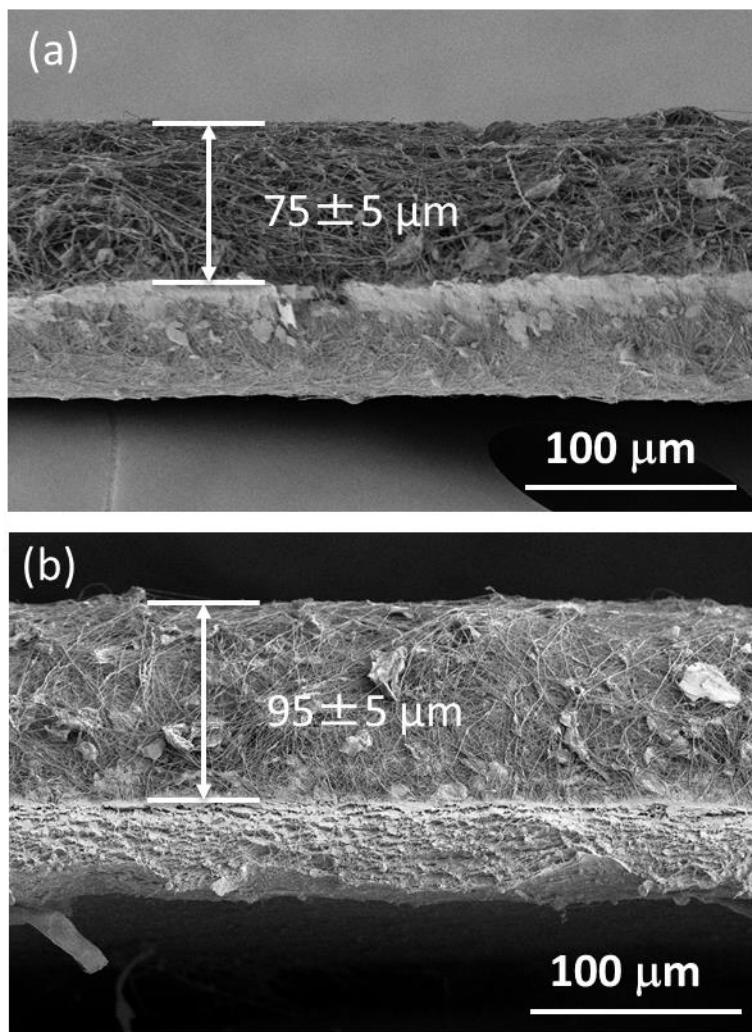


**Figure 4.2** Cross-sectional FESEM images of double-layer rGO-PVDF/PVDF separators with clear demonstration of rGO-PVDF and PVDF membrane layers: (a) rGO-PVDF/PVDF-1; (b) rGO-PVDF/PVDF-2.

**Table 4-1** . Porosity and electrolyte uptake parameters for PP, PVDF, rGO-PVDF/PVDF-1 and rGO-PVDF/PVDF-2 separators.

Sample	Porosity (%)	Electrolyte uptake (%)
PP	45	174
PVDF	68	310
rGO-PVDF/PVDF-1	70	354
rGO-PVDF/PVDF-2	71	380

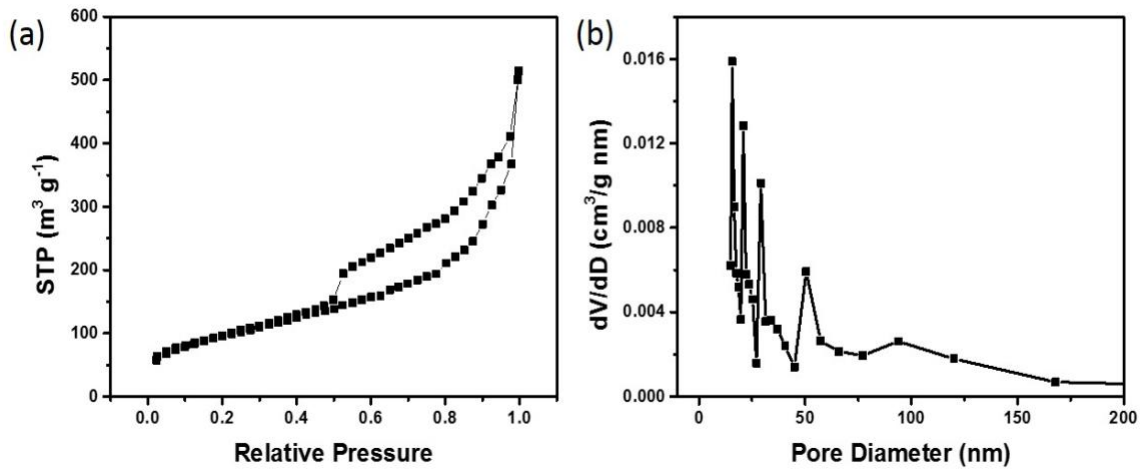


**Figure 4.3** (a) Nitrogen adsorption-desorption isotherms of rGO powders. (b) BJH pore-size distributions of rGO powders.

Figure 4.4a shows the XRD patterns of pure PVDF, rGO-PVDF/PVDF-1 and rGO-PVDF/PVDF-2 membrane separators. For comparison, the XRD pattern of rGO powder was also shown. The two characteristic diffraction peaks of rGO at 26.2° and 43.7° could be ascribed to the (002)

diffraction of layered graphite structure and (100) diffraction of graphite, respectively.<sup>93, 111</sup> On the other hand, only one sharp peak at  $2\theta$  angle of  $20.6^\circ$  was observed in pure PVDF nanofiber membrane, corresponding to the (110) diffraction of the  $\beta$ -phase of PVDF.<sup>79</sup> No obvious additional diffraction peaks were observed in two different rGO-PVDF/PVDF composite membrane separators.

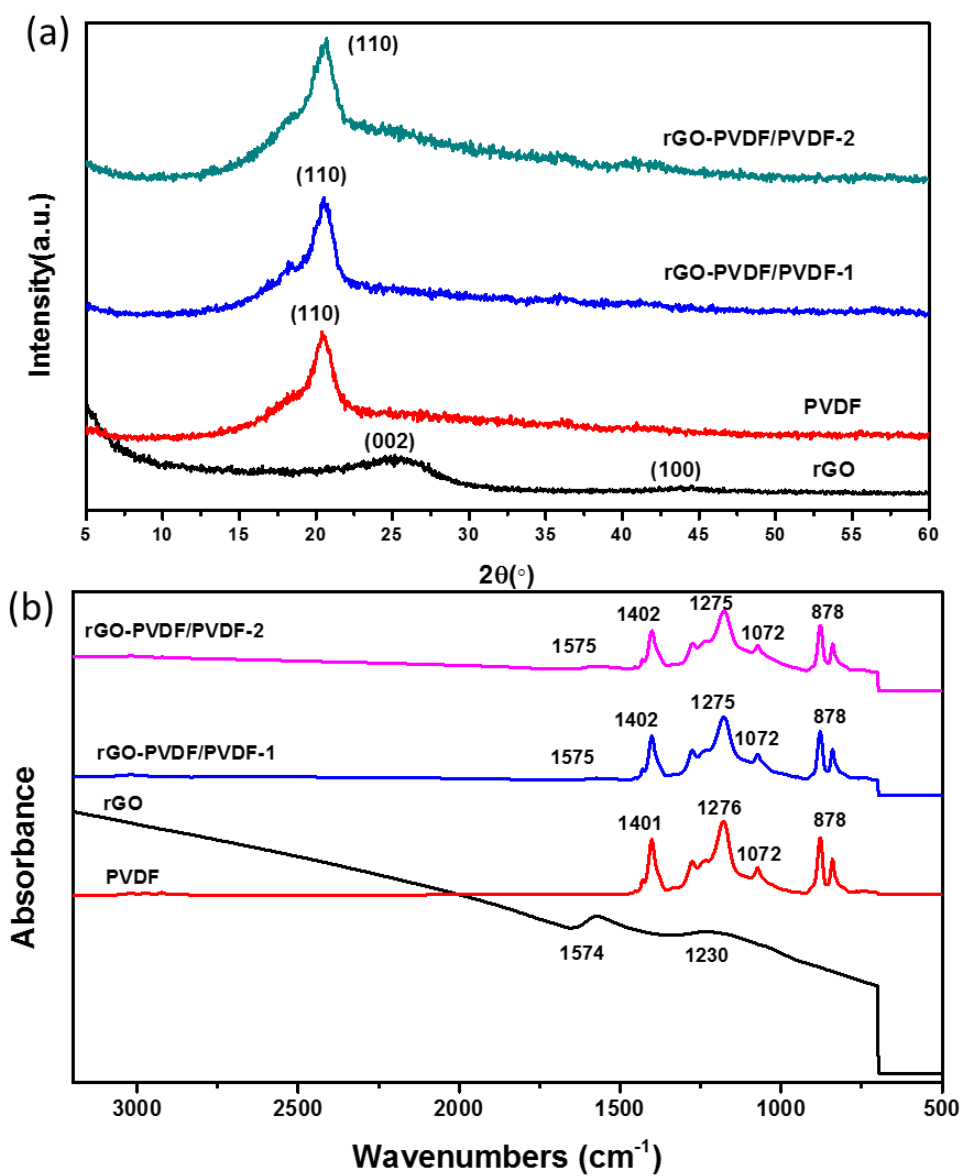


**Figure 4.4** (a) XRD patterns and (b) FTIR spectra of the rGO powder, and PVDF, rGO-PVDF/PVDF-1 and rGO-PVDF/PVDF-2 nanofiber separators.

FTIR spectroscopic analysis was conducted to further investigate the chemical structure/functional groups of rGO, pure PVDF, rGO-PVDF/PVDF-1 and rGO-PVDF/PVDF-2 membrane separators, as shown in Figure 4.4b. For the PVDF membrane, the peaks at 1401, 1276, 1072, 878  $\text{cm}^{-1}$  could be ascribed to the stretching mode of  $-\text{CH}_2-$  and  $-\text{CF}_2-$ , respectively.<sup>81, 112-113</sup> After incorporation of rGO into the PVDF membrane, a typical band of rGO was observed at 1575  $\text{cm}^{-1}$  in rGO-PVDF/PVDF-1 and rGO-PVDF/PVDF-2 composite membranes, which corresponded to the skeletal vibration from graphene domains.<sup>114-115</sup> In addition, the slightly increased peak intensity of rGO-PVDF/PVDF-2 at 1575  $\text{cm}^{-1}$  was associated with its higher rGO-PVDF layer thickness. Table 4-2 indicated the rGO powder had an oxygen concentration of 12.67 wt.%. No additional peaks relating to oxygen containing groups could be observed in rGO-PVDF/PVDF-1 and rGO-PVDF/PVDF-2 composite membranes in FTIR probably because of the relatively low oxygen concentration in rGO sheets as well as the low rGO concentration in the mixture rGO-PVDF precursor solution (0.8 wt.%). Overall, no significant absorption peak shift was observed in the composite separators when compared with the pristine PVDF (1402, 1276, 1027 and 878  $\text{cm}^{-1}$ ), indicating the coexistence of PVDF and rGO without any chemical interactions between them.

**Table 4-2** Elemental analysis and electrical conductivity results of rGO.

<b>Sample</b>	<b>Carbon (wt.%)</b>	<b>Hydrogen (wt.%)</b>	<b>Nitrogen (wt.%)</b>	<b>Oxygen (wt.%)</b>	<b>Conductivity (S <math>\text{cm}^{-1}</math>)</b>
<b>rGO</b>	85.51	1.11	0.71	12.67	2.1

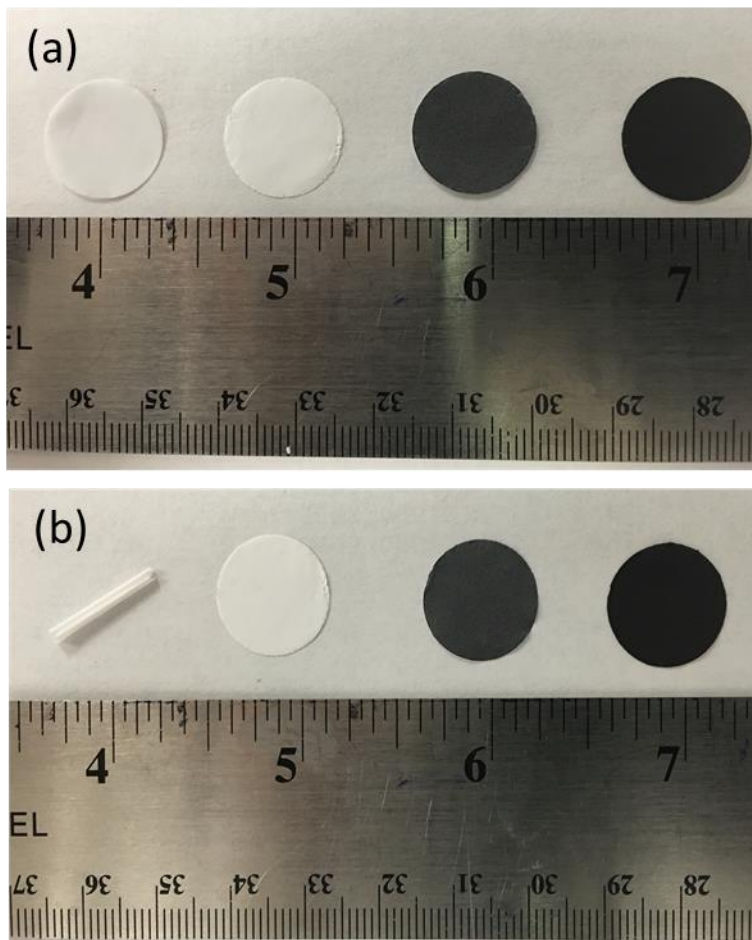


**Figure 4.5** Photographs of PP, PVDF, rGO-PVDF/PVDF-1 and rGO-PVDF/PVDF-2 separators (a) before and (b) after thermal treatment (dried after thermal treatment in liquid electrolyte at 80 °C for 24 h).

#### 4.3.2 Thermal Stability Measurement

Thermal shrinkage behavior of PP, PVDF, rGO-PVDF/PVDF-1 and rGO-PVDF/PVDF-2 separators was investigated by comparing their dimensional changes after thermal treatment at 80 °C for 24 h and the results are demonstrated in Figure 4.5. It was clear that

the PP separator went through severe dimensional change while all the PVDF based nanofiber membranes maintained their original shape, indicating their excellent dimensional stability under elevated temperatures. The poor dimensional stability of PP separators under elevated temperatures was the result of its low melting temperature.<sup>19</sup>

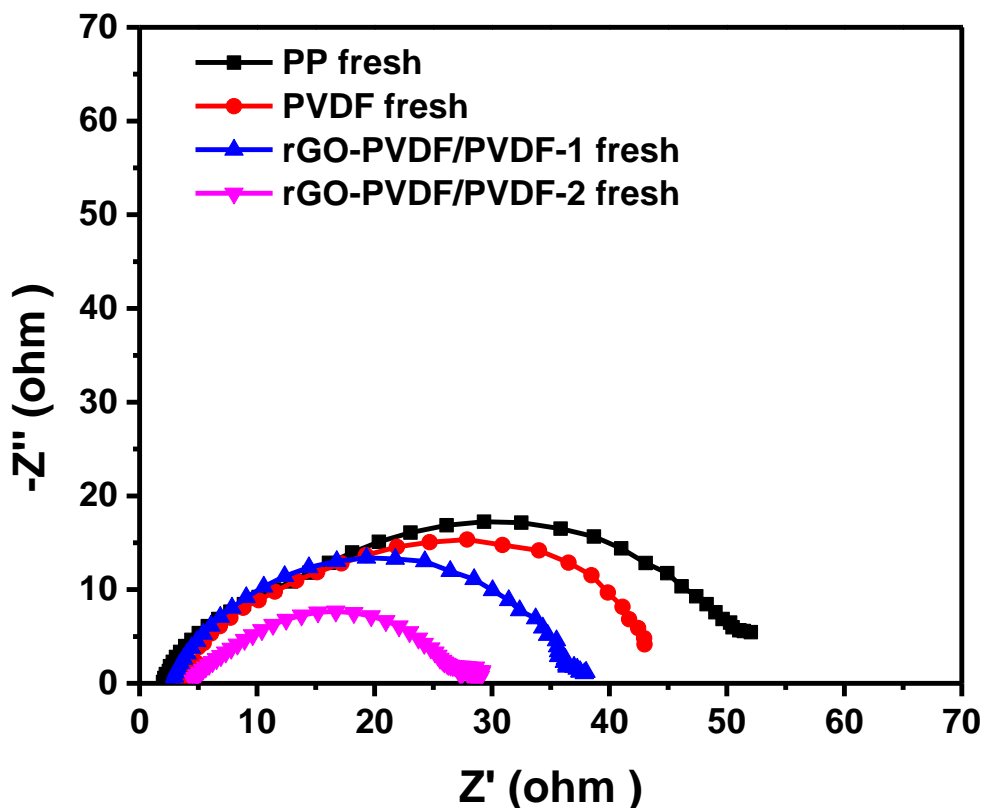


**Figure 4.6** Nyquist plots of Li-S cells with PP, PVDF, rGO-PVDF/PVDF-1 and rGO-PVDF/PVDF-2 separators before cycling.

#### 4.3.3 Electrochemical Evaluation

In order to analyze the impact of the rGO incorporation, electrochemical impedance analysis (EIS) was conducted from the frequency range of 1M Hz to 1Hz with the Li-S cells using PP, PVDF,

rGO-PVDF/PVDF-1 and rGO-PVDF/PVDF-2 separators before cycling. The Nyquist plots were shown in Figure 4.6 and the diameter of the semi-circle in Nyquist plots represents the charge transfer resistance ( $R_{ct}$ ). It was obvious that the  $R_{ct}$  values of the cells with PP, PVDF, rGO-PVDF/PVDF-1 and rGO-PVDF/PVDF-2 separators were 50.0, 39.2, 35.2, and 22.8  $\Omega$ , respectively. The reduced  $R_{ct}$  values of rGO-PVDF/PVDF-1 and rGO-PVDF/PVDF-2 separators could be ascribed to the conductive rGO incorporated layer (the electrical conductivity of rGO was 2.1 S  $\text{cm}^{-1}$  as showed in Table S1), acting as an embedded current collector thus significantly minimizing internal resistance.<sup>14, 106</sup>

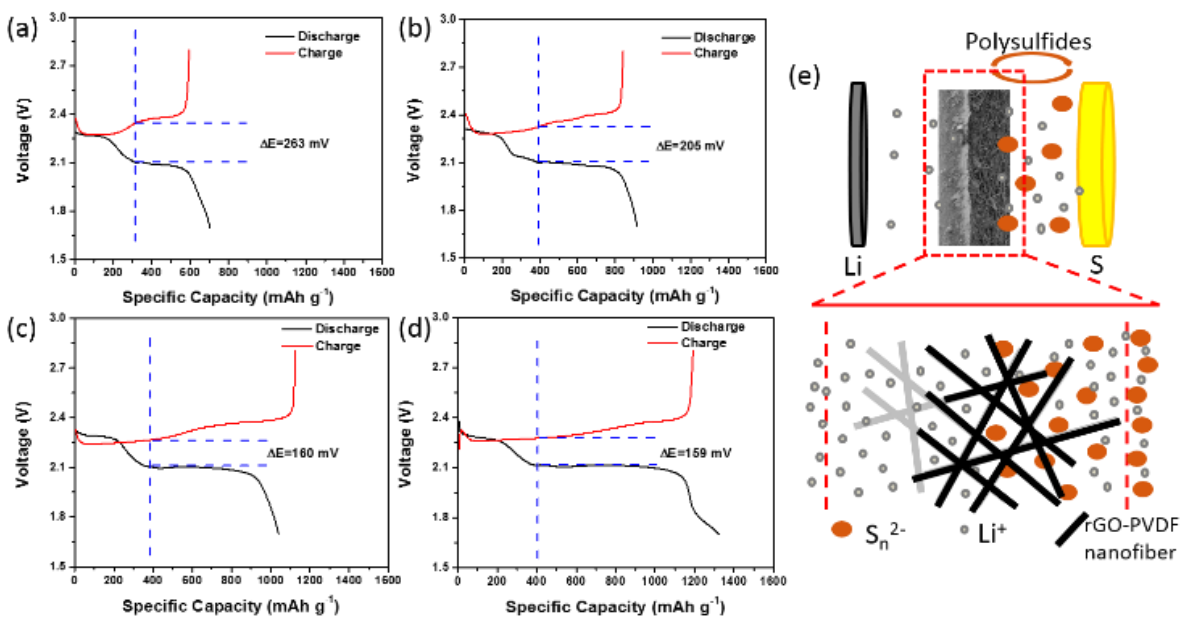


**Figure 4.7** Galvanic discharge-charge curves of Li-S cells with (a) PP, (b) PVDF, (c) rGO-PVDF/PVDF-1 and (d) rGO-PVDF/PVDF-2 separators. (e) Schematic illustration of bifunctional double-layer rGO-PVDF/PVDF membrane separator.

Galvanostatic discharge-charge curves of Li-S cells with PP, PVDF, rGO-PVDF/PVDF-1 and rGO-PVDF/PVDF-2 separators at a current density of 0.2 C are shown in Figure 4.7. All the cells exhibited two discharge regions: the first one refers to the formation of long-chain polysulfides at the voltage range of 2.4-2.1 V vs Li<sup>+</sup>/Li and the second one refers to the formation of short chain Li<sub>2</sub>S<sub>2</sub>/Li<sub>2</sub>S at the range of 2.1-1.7 V vs Li<sup>+</sup>/Li.<sup>24</sup> From Figures 4.7a-d, two continuous regions in the charge curves of all four Li-S cells were observed, representing the reaction from lithium sulfides to polysulfides and finally to sulfur. Besides, the cells with rGO-PVDF/PVDF-1 and rGO-PVDF/PVDF-2 separators showed lower polarization potentials of 160 and 159 mV, respectively, indicating the smaller reaction barriers due to the incorporation of rGO. Compared to the cells with PP separator (discharge capacity of 703 mAh g<sup>-1</sup>), the cells with PVDF, rGO-PVDF/PVDF-1 and rGO-PVDF/PVDF-2 separators showed higher discharge capacities of 817, 1040 and 1322 mAh g<sup>-1</sup>, respectively. The improved capacities in cells with PVDF, rGO-PVDF/PVDF-1 and rGO-PVDF/PVDF-2 separators could be partially ascribed to the presence of a porous nanofibrous network structure, which could absorb more electrolyte to facilitate the lithium-ion transfer. In addition, the conductive rGO incorporated layer, because of the high electrical conductivity, high specific surface area as well as the oxygen containing functional groups of rGO, serves as a second current collector and polysulfide reservoir, and hence polysulfides tend to be confined between the cathode and the rGO-PVDF layer and to be reutilized instead of shuttling through the whole separator and depositing on the lithium anode surface, enhancing the active material utilization.<sup>14, 24, 94</sup> Figure 4.7e showed the schematic configuration of this effective bi-functional double-layer separator.

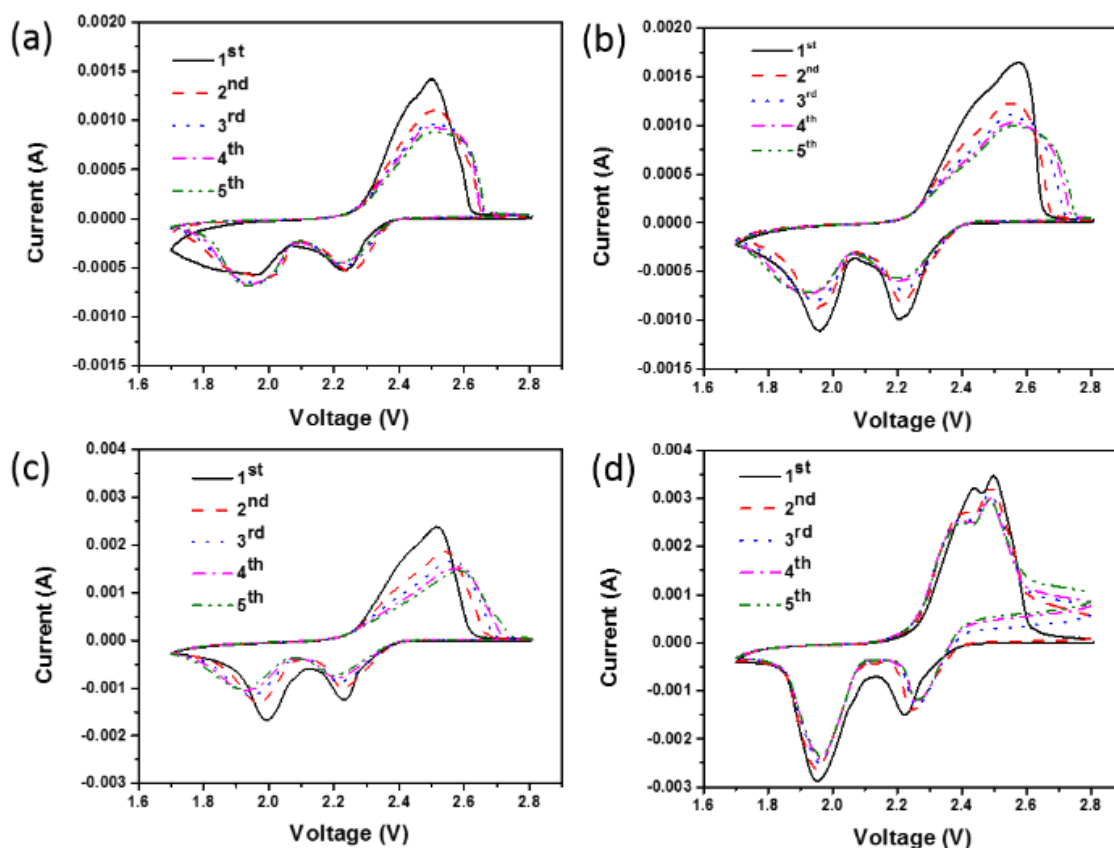


**Figure 4.8** CV curves of Li-S cells with (a) PP, (b) PVDF, (c) rGO-PVDF/PVDF-1 and (d) rGO-PVDF/PVDF-2 separators.

CV tests of Li-S cells with PP, PVDF, rGO-PVDF/PVDF-1 and rGO-PVDF/PVDF-2 separators were conducted with a cut off voltage of 2.8 V to 1.7 V at a scan rate of  $0.1 \text{ mV s}^{-1}$  (Figure 4.8). All four cells showed typical redox reactions of Li-S batteries with two cathodic peaks and one overlapped broad anodic peak. Interestingly, for the cell with rGO-PVDF/PVDF-2 membrane separator, the peak positions, intensities and the integral areas were almost same for the 1<sup>st</sup> and 2<sup>nd</sup> cycles, which demonstrated the good cycling stability of the cell.<sup>23</sup> On the contrary, for the cells with PP and PVDF separators, the peak positions shifted towards positive or negative potentials in

the subsequent cycles and became wider, which indicated the sluggish reaction kinetics process of Li-S system.<sup>23</sup> The fast reaction kinetics processed by cells with rGO-PVDF/PVDF-1 and rGO-PVDF/PVDF-2 separators could be ascribed to the presence of highly-conductive rGO with functional groups, which not only facilitated the high rate of charge transfer but also provided sufficient conductive sites for polysulfides, thus significantly minimizing the shuttle effect and improving the active material utilization.<sup>14</sup>

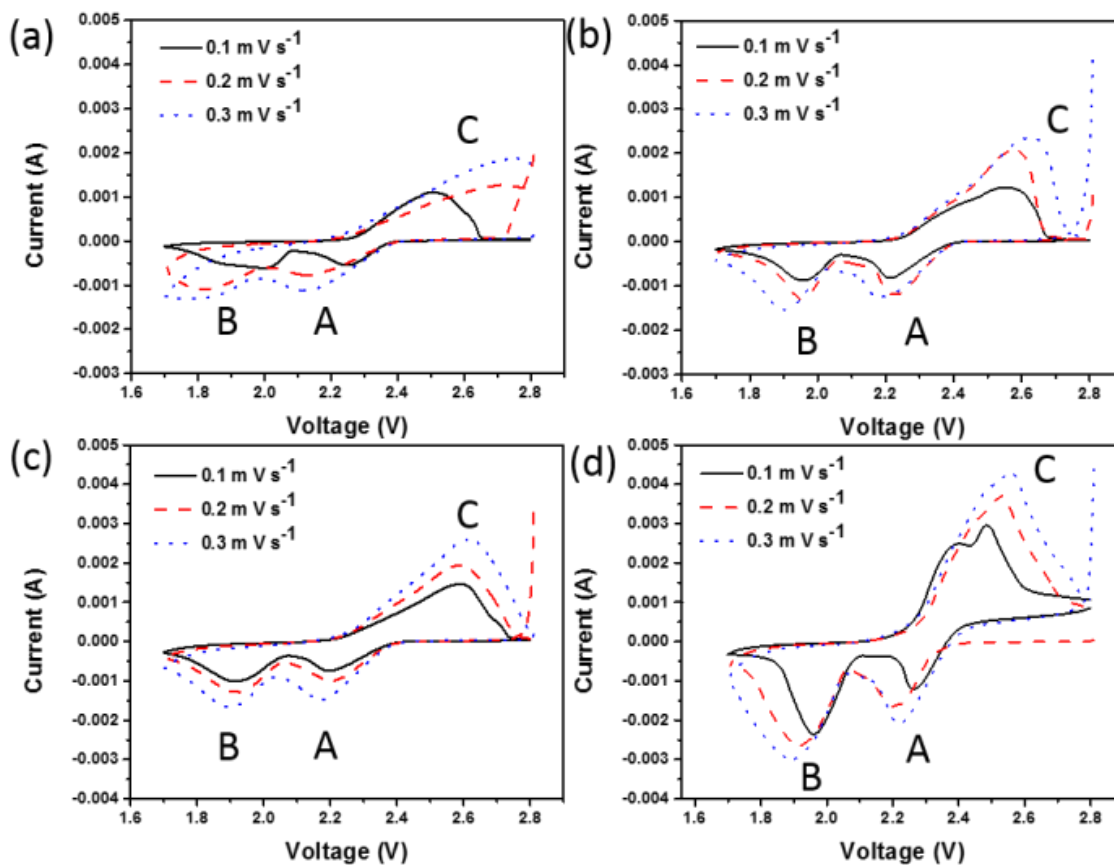


**Figure 4.9** CV curves at scan rates of 0.1, 0.2 and 0.3 mV s<sup>-1</sup> of Li-S cells with (a) PP, (b) PVDF, (c) rGO-PVDF/PVDF-1 and (d) rGO-PVDF/PVDF-2 separators.

#### 4.3.4 Lithium Ion Diffusion Coefficients

To further investigate the impact of the rGO incorporation on lithium-ion transfer, lithium-ion diffusion coefficients were measured by CV with different scan rates of 0.1, 0.2 and 0.3 mV s<sup>-1</sup> and calculated based on the Randles-Sevick equation:

$$I_p = 2.69 \times 10^5 n^{1.5} A D_{Li}^{+0.5} C_{Li}^+ v^{0.5} \quad (4.3)$$

where  $I_p$  is the peak current in A;  $n$  the number of electrons transferred during the reaction which is 2 for Li-S cells;  $A$  the electrode area which is 1.27 cm<sup>2</sup>;  $C_{Li}^+$  the concentration of  $Li^+$  in electrolyte in unit of mol mL<sup>-1</sup>, and  $v$  the scanning rate in unit of V s<sup>-1</sup>. Figure 4.9 shows the CV curves of Li-S cells with PP, PVDF, rGO-PVDF/PVDF-1 and rGO-PVDF/PVDF-2 separators at different scan rates of 0.1, 0.2 and 0.3 mV s<sup>-1</sup>. It was obvious that all the cathodic and anodic peak currents had linear correlation with the square root of the scan rates ( $v^{0.5}$ ) from the Randles-Sevick equation, which was clearly shown in Figure 4.10. As the slopes obtained from the linear fit of the curves were correlated with the lithium-ion diffusion coefficient, it was clear that the cell with PP separator showed the lowest lithium ion diffusivity which could be ascribed to its poor capability in trapping polysulfides since the accumulation of polysulfides in the electrolyte could increase its viscosity.<sup>116</sup> The lithium-ion diffusion coefficients at peak A were calculated to be  $7.24 \times 10^{-9}$ ,  $4.19 \times 10^{-9}$ ,  $1.15 \times 10^{-8}$  and  $1.69 \times 10^{-8}$  for cells with PP, PVDF, rGO-PVDF/PVDF-1 and rGO-PVDF/PVDF-2 separators, respectively. At peak B, the lithium-ion diffusion coefficients for the cells with the four separators were  $4.27 \times 10^{-9}$ ,  $9.7 \times 10^{-9}$ ,  $9.16 \times 10^{-9}$ , and  $2.41 \times 10^{-8}$ , respectively. Then the lithium-ion diffusion coefficients became  $1.22 \times 10^{-8}$ ,  $2.89 \times 10^{-8}$ ,  $2.68 \times 10^{-8}$ , and  $3.80 \times 10^{-8}$

<sup>8</sup>, respectively, at peak C for the Li-S cells with these four separators. These results further demonstrated that the superior performance of the cell with rGO-PVDF/PVDF-2 membrane was as a result of the rGO's excellent conductivity and ability in capturing polysulfides.

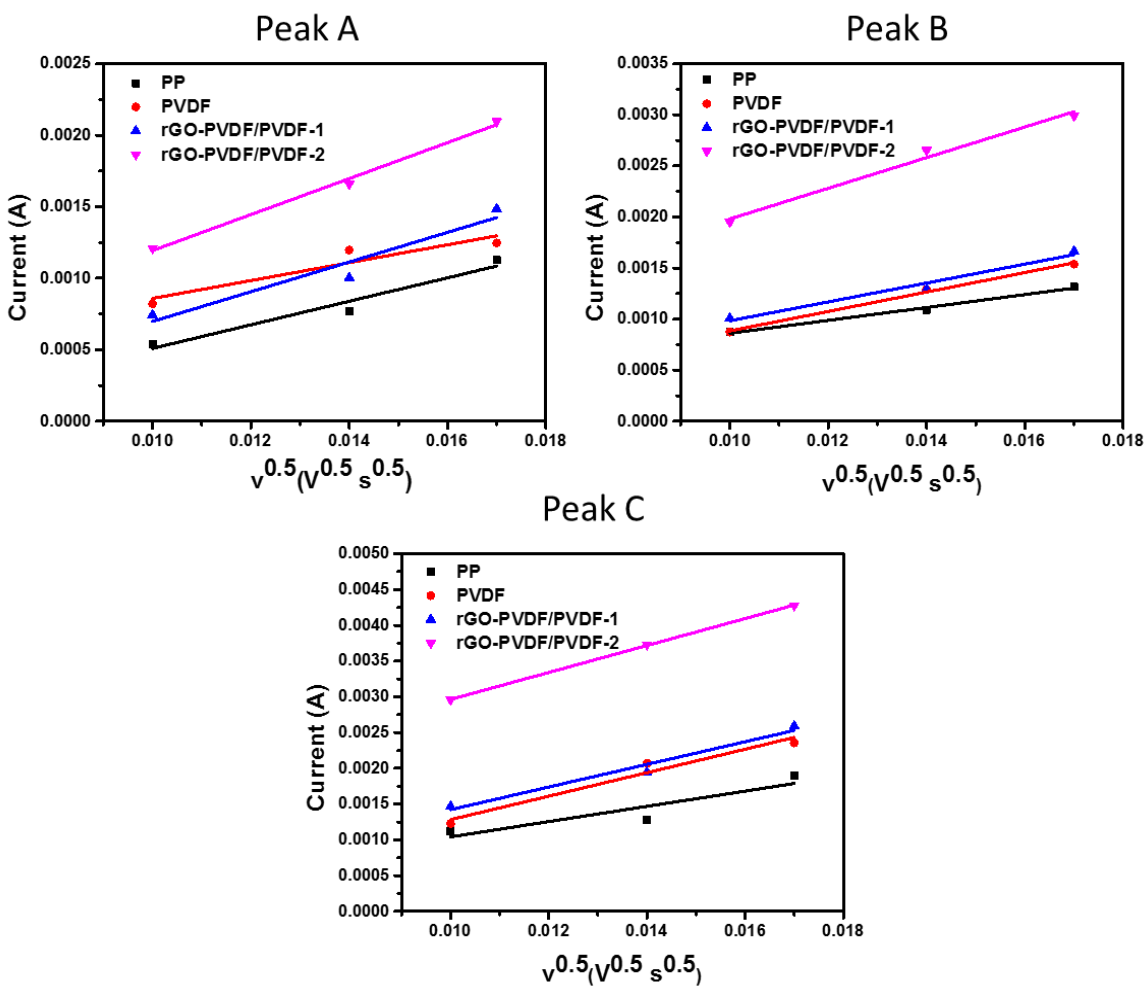


**Figure 4.10** Plots of CV peak currents: peak A refers to the cathode reaction of  $S_8$  to  $Li_2S_4$ ; peak B refers to the cathodic reaction of  $Li_2S_4$  to  $Li_2S$ ; and peak C refers to the anodic reaction of  $Li_2S$  to  $S_8$ .

#### 4.3.4 Rate Capabilities and Cycle Performance

Rate capabilities of Li-S cells with PP, PVDF, rGO-PVDF/PVDF-1 and rGO-PVDF/PVDF-2 separators were tested with different current C rates range from 0.2C to 2C for every 10 cycles and results are demonstrated in Figure 4.11a. The cell with rGO-PVDF/PVDF-2 separator showed the highest capacity of 1070 mAh g<sup>-1</sup> at a current density of 0.2C, which was 117%, 92% and 33% higher than those of cells with PP (492 mAh g<sup>-1</sup>), PVDF (557 mAh g<sup>-1</sup>) and rGO-PVDF/PVDF-2 (805 mAh g<sup>-1</sup>) separators, respectively. The capacities of the cell with PP separator were 322, 206 and 9 mAh g<sup>-1</sup> at 0.5, 1 and 2C. Then the capacities slightly increased to 380, 215 and 14 mAh g<sup>-1</sup> for the cell with PVDF separator at 0.5, 1 and 2C. More importantly, for the Li-S cells with rGO-PVDF/PVDF-1 and rGO-PVDF/PVDF-2 separators, the capacities significantly increased to 569, 454, 265 and 806 708, 590 mAh g<sup>-1</sup>, respectively, which revealed their ultrafast rate capabilities during charge/discharge. It is also important to note that the cell with rGO-PVDF/PVDF-2 separator could still deliver a discharge capacity of 822 mAh g<sup>-1</sup> when the current density was reversed back to 0.2 C, which was 141%, 69% and 27% higher than those of the cells with PP, PVDF and rGO-PVDF/PVDF-1 separators, respectively, indicating a highly efficient system with the introduction of highly conductive rGO into the porous PVDF skeleton.

The long cycling performance of the Li-S cells with different separators was tested at a current density of 0.2C and the results are shown in Figure 4.11b. The initial discharge capacities for Li-S cells with PP, PVDF, rGO-PVDF/PVDF-1 and rGO-PVDF/PVDF-2 separators were 703, 817, 1040 and 1322 mAh g<sup>-1</sup>, respectively. However, the discharge capacities kept on decreasing for the cells with PP and PVDF separators and only 372 and 380 mAh g<sup>-1</sup> were left after 100 cycles. For comparison, the Li-S cells with rGO-PVDF/PVDF-1 and rGO-PVDF/PVDF-2 separators

exhibited more stable cycling performance with discharge capacities of 522 and 646 mAh g<sup>-1</sup> maintained at the 200th cycle, which further demonstrated the significance of the inclusion of rGO contained layer. The coulombic efficiencies of the cells with PP and PVDF separators reached 96% and 99% after 100 cycles while the cells with rGO-PVDF/PVDF-1 and rGO-PVDF/PVDF-2 separators maintained coulombic efficiencies of 97% and 95% after 200 cycles. As discussed above, the better cycling performance of the double-layer membrane separators could be ascribed to the presence of a rGO-PVDF layer, which not only reduced the internal resistance of the cells, facilitating the transportation of lithium-ions, but also helped provide sufficient conductive sites, thus minimizing the shuttle effect and significantly enhancing the active material utilization.

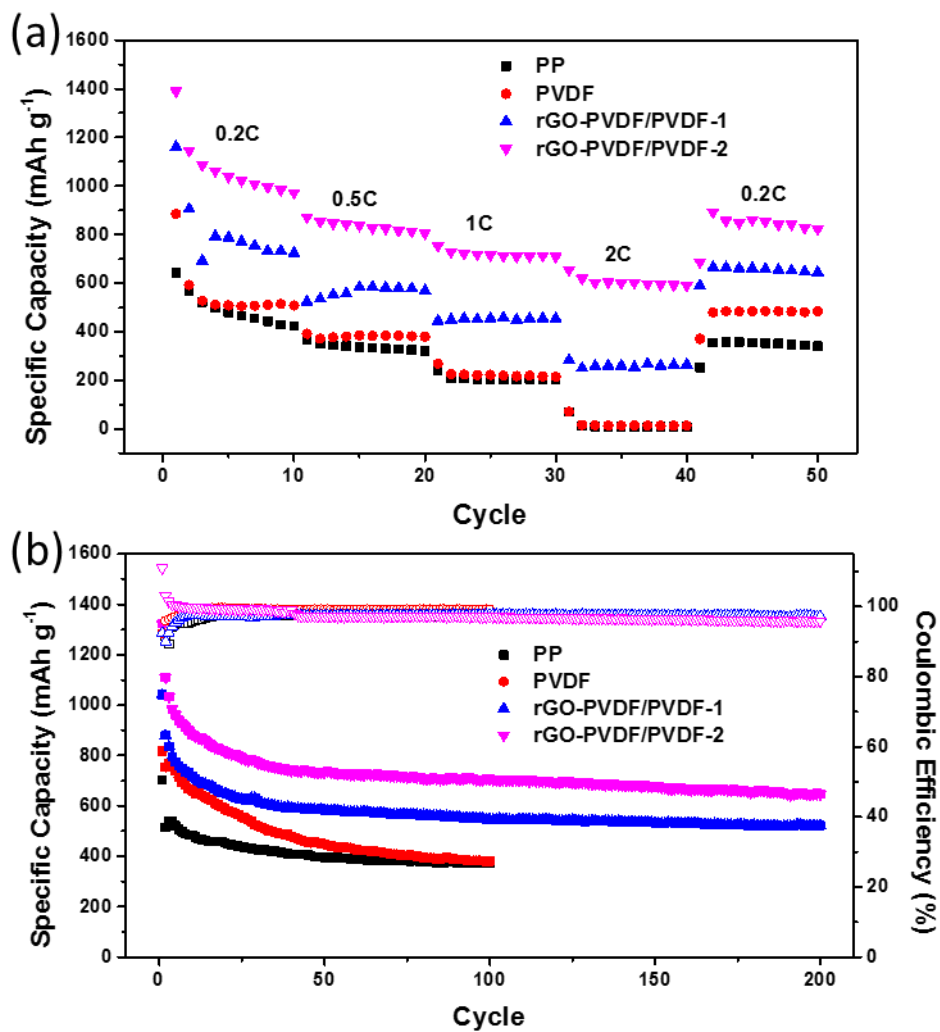


**Figure 4.11** (a) Rate capabilities of Li-S cells with PP, PVDF, rGO-PVDF/PVDF-1 and rGO-PVDF/PVDF-2 separators at current densities of 0.2C, 0.5C, 1C, 2C and 0.2C, respectively. (b) Cycling performance of Li-S cells with PP, PVDF, rGO-PVDF/PVDF-1 and rGO-PVDF/PVDF-2.

#### 4.3.5 Evaluation of polysulfide Rejection - Surface Morphology of Cycled Separators/Li Metal Anode and EIS Curves

To further demonstrate the retarded polysulfide diffusion in the Li-S cell with rGO-PVDF/PVDF-2 separator, the cells with PP and rGO-PVDF/PVDF-2 separators were disassembled after 200 cycles at 1C, and FESEM images and related S mappings of the cycled separators facing the Li metal side were analyzed and compared, as shown in Figure 4.12. It was seen that the surface of the PP membrane was covered by S-related species (Figure 4.12a). At a higher magnification (Figure 4.12c), the FESEM image revealed that the open pores in the PP separator were largely blocked by the S-related species and only few pores were exposed, which severely impeded the lithium ion transportation. The lower cycle capacity and sluggish reaction kinetic of the cell with PP separator could partially be the result of the blocked pores. On the other hand, compared with PP, the rGO-PVDF/PVDF-2 separator showed much better performance in suppressing the migration of polysulfides as the open pores within the network structure could be clearly seen from the SEM image (Figure 4.12b) even though it still showed random accumulation of S-related species on the surface of the nanofiber membrane. In addition, it was found that the S-related species were mainly attached on the surface of network-like nanofibers (Figure 4.12d), which might come from the relatively high binding energy between sulfur related species and C-F groups.<sup>100, 117</sup> Moreover, compared with PP membrane, rGO-PVDF/PVDF-2 separator showed weaker S signal in the element mapping (Figures 4.12e and f). Figure 4.13 shows the SEM images of PP and rGO-PVDF/PVDF-2 separators after 100 cycles at 1C and similar morphological changes could be observed in both separators.

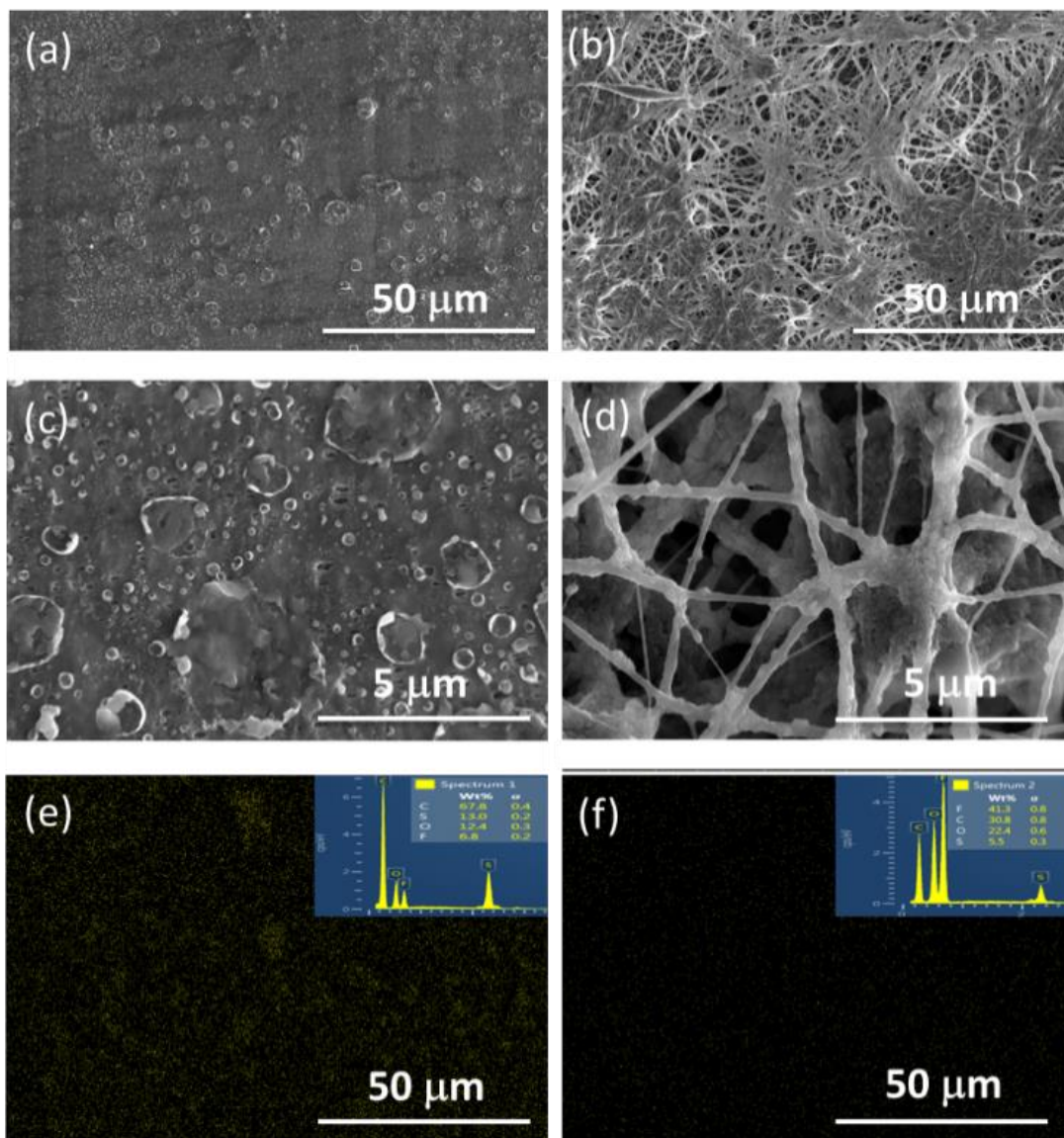


**Figure 4.12** SEM images of (a, c) PP and (b, d) rGO-PVDF/PVDF-2 separators towards Li metal side after 200 cycles at 1C, and (e, f) corresponding S mappings of (a) and (b), respectively.

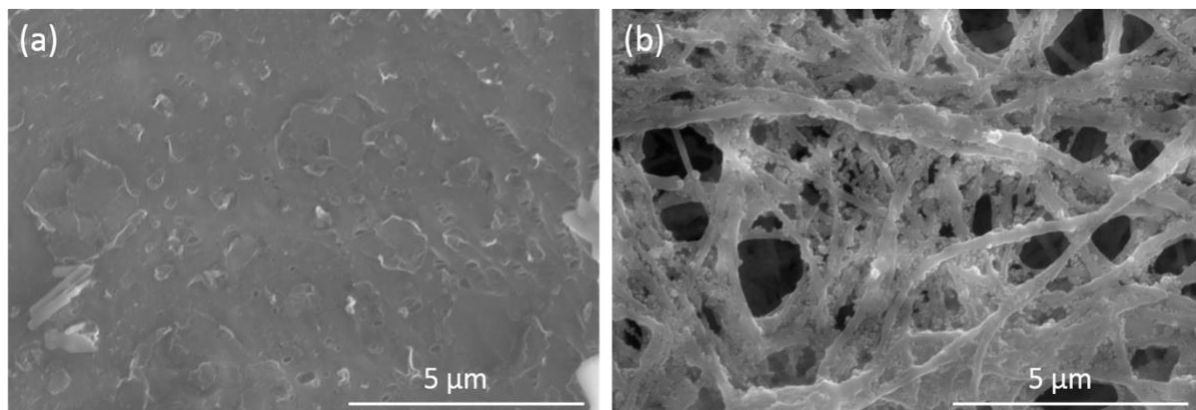


**Figure 4.13** SEM images of (a) PP and (b) rGO-PVDF/PVDF-2 separators towards Li metal side after 100 cycles at 1C.

Figure 4.14 indicated the surface morphological changes of Li metal anode after 200 cycles at 1C. Obvious damage with cracks and very dense/un-even accumulation of S related species could be observed on the surface of the lithium metal anode in Li-S cell with PP separator, which came from the side reactions of polysulfides with metallic Li during cycling. In contrast, a relatively less damaged and smooth Li anode surface could be observed in the Li-S cell with rGO-PVDF/PVDF-2 separator. The S mappings also showed that the cycled Li anode surface with PP separator presented a much stronger S signal when compared with the cycled Li anode surface with rGO-PVDF/PVDF-2 separator (Figures 4.14c and d). Those results were consistent with the surface morphological changes in PP and rGO-PVDF/PVDF-2 separators and the electrochemical performance of Li-S cells, which suggested the excellent functionality of this double-layer nanofiber membrane separator structure. Yan and his co-workers used *in-situ* UV/vis analysis and SEM to study the structural change of Li anodes in rGO-added Li-S cells during cycling, and they also found that the minimized polysulfide shuttling could lead to relatively uniform morphology in cycled Li anode.<sup>118</sup>

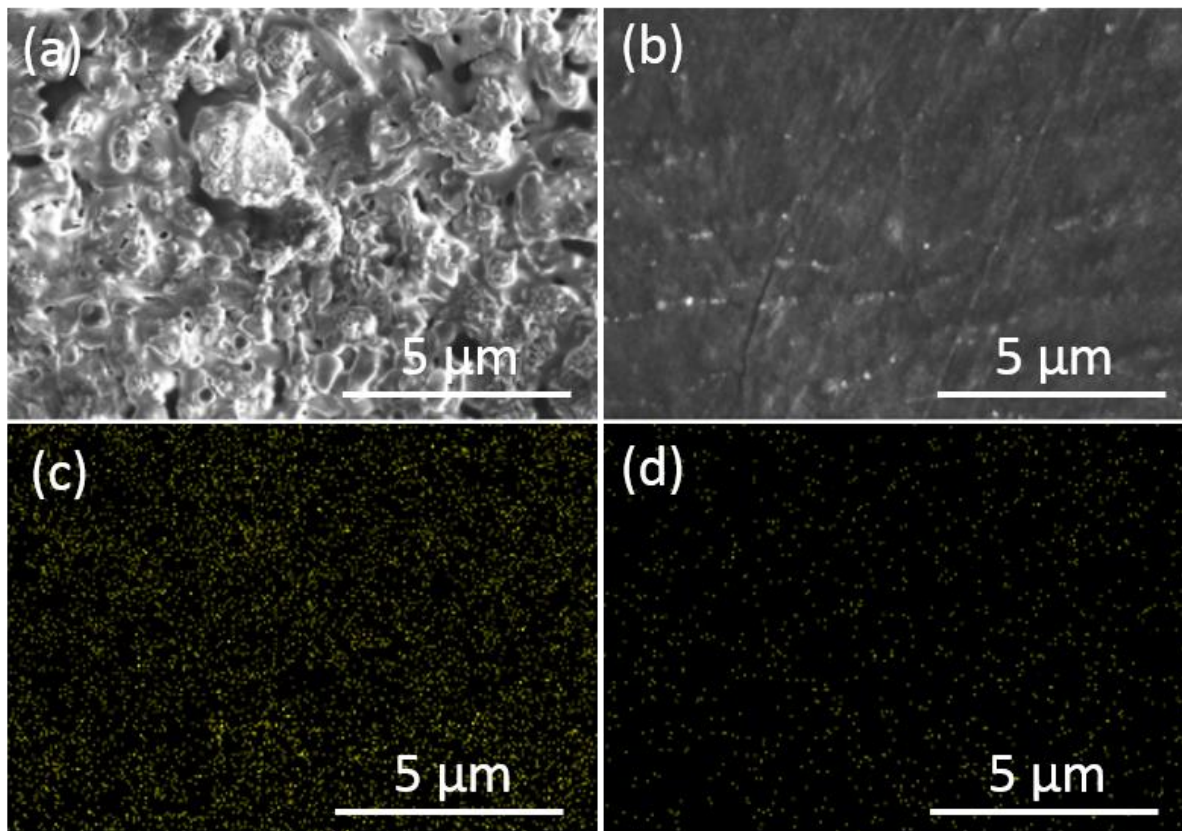


**Figure 4.14** SEM images of Li metal anode surface with (a) PP and (b) rGO-PVDF/PVDF-2 separators after 200 cycles at 1C, (c, d) corresponding S mapping of (a, b), respectively.

The ability of rGO-PVDF/PVDF separators in minimizing the shuttle effect of polysulfides could also be reflected in the EIS measurements. The EIS tests were conducted with the cells before and after 200 cycles at 1C in a frequency range of 1M Hz to 1Hz and the results are illustrated in Figure 4.15. It was found that the cell with PP separator showed  $R_{ct}$  values of 50.0 and 158.4  $\Omega$ , respectively, before and after cycling. However, benefiting from the rGO-PVDF layer, the  $R_{ct}$  value in the cell with rGO-PVDF/PVDF-2 separator was 27.7 $\Omega$  even after 200 cycles, which did

not increase too much as compared to the fresh cell, which showed a  $R_{ct}$  of 22.8  $\Omega$  before cycling. Normally, an increased diameter of the semicircle in Nyquist plot reflects the accumulation of uncontrolled polysulfides as a result of the higher degree of polysulfide diffusion.<sup>119-121</sup> Compared with the large  $R_{ct}$  increase in the cell with PP separator after 200 cycles, the small  $R_{ct}$  value change in the cell with rGO-PVDF/PVDF-2 separator before and after 200 cycles suggested the good ability of the rGO layer in trapping and reutilizing polysulfides, which mitigated the accumulation of S related species on the lithium anode and ensured fast charge and lithium ion transport. Those findings were consistent with the morphology observation (Figures 4.12a-d, Figures 4.14a and b) as well as S mapping data observed on separators towards the lithium metal side/lithium anodes (Figures 4.12e and f, Figures 4.14c and d) that after cycling, rGO-PVDF/PVDF-2 separator/lithium anode could still maintain the network structure/relative smooth surface with weak S signals.

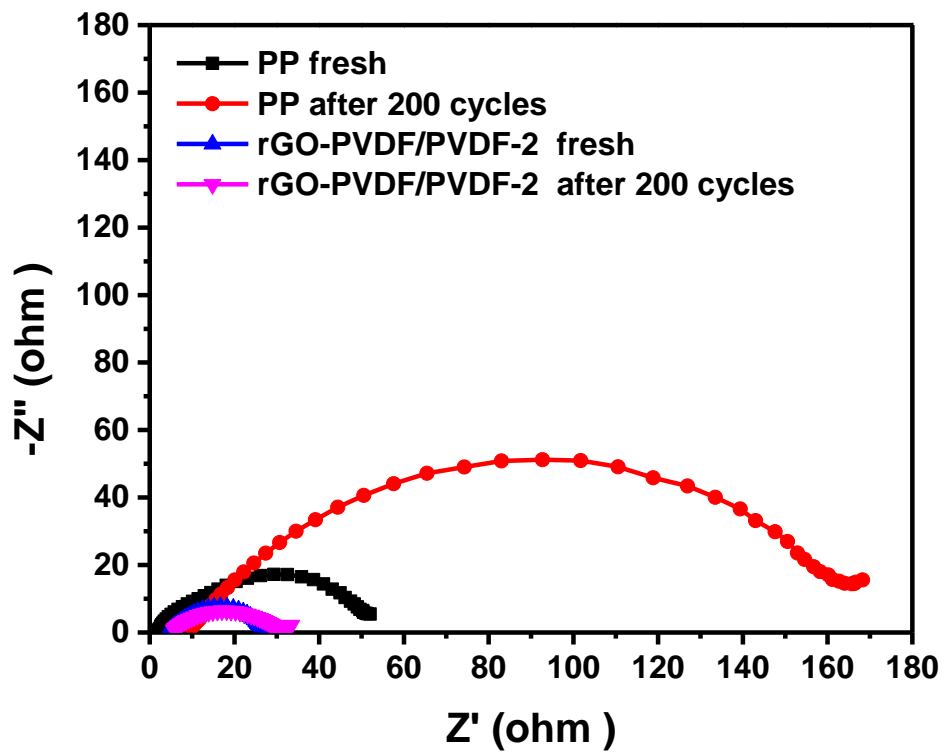


**Figure 4.15** Nyquist plots of Li-S cells with PP and rGO-PVDF/PVDF-2 separators before and after 200 cycles at 1C.

#### **4.4 Conclusion**

A bi-functional double-layer rGO-PVDF/PVDF nanofiber membrane separator was developed to enable the safe operation and stable cycling performance of Li-S batteries. Compared with PP separator, the rGO-PVDF/PVDF membrane separator with nanofibrous PVDF framework and rGO incorporated conductive layer demonstrated combined functionalities of significantly enhanced thermal stability as well as effective polysulfide inhibition. This novel double-layer separator design provides a general strategy in dealing with multiple challenges of Li-S batteries.

**CHAPTER 5       $\text{Li}_{0.33}\text{La}_{0.557}\text{TiO}_3$  CERAMIC NANOFIBER-ENHANCED  
POLY(ETHYLENE OXIDE)-BASED COMPOSITE POLYMER ELECTROLYTE FOR  
ALL-SOLID-STATE LITHIUM BATTERIES**

**Abstract**

A polyethylene oxide (PEO)-based composite solid polymer electrolyte filled with one-dimensional (1D) ceramic  $\text{Li}_{0.33}\text{La}_{0.557}\text{TiO}_3$  (LLTO) nanofibers was designed and prepared. It exhibits a high ionic conductivity of  $2.4 \times 10^{-4} \text{ S cm}^{-1}$  at room temperature and a large electrochemical stable window of up to 5.0 V vs Li/Li<sup>+</sup>, and is a promising electrolyte candidate for all solid-state lithium batteries.

**Key Words:** Polyethylene oxide, LLTO, Solid polymer electrolyte, All-solid-state lithium batteries

## 5.1 Introduction

After commercialization of lithium-ion batteries (LIBs) in 1991, tremendous progress has been achieved in portable electronic devices such as smartphones, laptops, etc.<sup>122-123</sup> However, because of the emerging demand on high-energy density batteries for large-scale electric device (EVs), LIBs meet their bottleneck, which is due to the inherent chemistry limitations of LIBs.<sup>4</sup> Novel electrode materials including high capacity sulfur (S), lithium (Li) metal and high voltage oxides are promising candidates for high energy density batteries.<sup>12, 124-125</sup> However, the use of these materials in contact with liquid electrolytes leads to several safety issues in addition to the flammability of organic solvent.<sup>126</sup> The polysulfide dissolution, Li dendrite formation as well as the uncontrolled side reactions of these materials remains challenges for the development of high-energy density batteries.<sup>3, 12</sup>

Solid electrolytes are considered as promising material their good mechanical strength (beneficial for mitigation of Li dendrite penetration) and potentially high electrochemical stability (necessary for stable operation).<sup>127-128</sup> Among all solid electrolyte systems, the solid-state polymer electrolytes (SPEs) have gained more attention.<sup>129</sup> In SPEs, various polymers like polyacrylonitrile (PAN), poly(ethylene oxide) (PEO), poly(vinylidene fluoride) (PVDF) and poly(methyl methacrylate) (PMMA) are usually blended with Li salts.<sup>32-33, 130-131</sup> However, the ionic conductivity of these SPEs is relatively low ( $10^{-6} - 10^{-9}$  S cm<sup>-1</sup> at room temperature), which severely hinders their use in high energy density batteries.<sup>32, 132</sup> It has been known that the ionic conductivity of SPEs is mainly controlled by the amorphous regions of the polymer matrix, thus diminishing the crystallinity of polymers can improve the ionic mobility and the X-ray diffraction (XRD) and differential scanning calorimetry (DSC) are two main techniques that are used to verify the

amorphous phase.<sup>131-134</sup> Previous approaches including adding plasticizers, forming co-polymer and cross-linking polymers have been demonstrated for improving the ionic conductivity of SPEs, but only with the sacrifice of some benefits of SPEs, *i.e.*, adding plasticizers lowered the mechanical strength and electrochemical stability of SPEs.<sup>135-136</sup>

On the contrary, adding ceramic fillers in the polymer matrix can improve the ionic conductivity and electrochemical stability of the SPEs *simultaneously*.<sup>132</sup> Appleby and his coworkers added  $\text{La}_{0.55}\text{Li}_{0.35}\text{TiO}_3$  ceramic particles into the PEO polymer matrix and they observed improved ionic conductivity and interfacial stability of SPEs.<sup>130</sup> Cui and coworkers reported that in-situ synthesized silicon dioxide ( $\text{SiO}_2$ ) nanoparticles in polyethylene oxide (PEO) matrix significantly suppresses the crystallization of PEO and leads to high ionic conductivity of  $4.4 \times 10^{-5} \text{ S cm}^{-1}$  at  $30 \text{ }^\circ\text{C}$ .<sup>50</sup> Although the in-situ hydrolysis method provided better distribution/contact of  $\text{SiO}_2$  in PEO matrix compared to dispersing pre-made  $\text{SiO}_2$  particles in PEO polymer, further improvements are still needed to overcome the bumper of particle-particle junction, which is essential for the ionic conductivity improvement. To minimize the particle-particle junction, one-dimensional (1D) inorganic nanofiber fillers, with high surface-to-volume ratio, are preferable for composite solid polymer electrolyte applications, which need large surface area to ensure good filler-matrix contact.<sup>20</sup> Presence of highly-conductive 1D ceramic nanofiber fillers could improve the ionic conductivity of the SPEs by introducing a continuous ion conducting pathway within the polymer matrix, and at the same, could further hinder the crystallinity of polymer matrix and facilitate the polymer segmental mobility for ion conduction.<sup>32-33</sup>

Having noticed the huge benefits of highly-ionic conductive 1D ceramic fillers, here we report  $\text{Li}_{0.33}\text{La}_{0.557}\text{TiO}_3$  (LLTO) nanofiber-incorporated PEO-based composite polymer electrolytes for all-solid-state Li batteries. LLTO nanofibers were prepared by electrospinning and subsequent annealing processes and were later dispersed into PEO polymer, which was pre-mixed with Li salts. Introducing ceramic LLTO nanofibers into PEO matrix has several desired advantages: *i*) dispersion of 1D LLTO nanofibers could provide continuous ionic conductive pathways, *ii*) LLTO nanofibers with high surface area could increase the effective conductive interface between ceramic LLTO fillers and PEO polymer, which could also control the recrystallization kinetics of the PEO polymer chains and help diminish the crystallinity of PEO, and *iii*) LLTO ceramic fillers could also improve the electrochemical stability of PEO polymer electrolyte. With all aforementioned benefits of LLTO nanofiber fillers, LLTO nanofiber/PEO composite solid polymer electrolyte demonstrated good ionic conductivity of  $2.4 \times 10^{-4} \text{ S cm}^{-1}$  at room temperature. Moreover, a largely extended electrochemical stability window up to 5.0 V was also obtained, which implies that this composite solid electrolyte could meet higher voltage requirements of most lithium batteries. Hence, it is demonstrated that LLTO nanofiber-enhanced PEO-based composite solid polymer electrolyte with good ionic conductivity and large electrochemical stability window is a promising electrolyte candidate for solid-state lithium batteries.

## 5.2 Experimental

### 5.2.1 Synthesis of LLTO Nanofibers

$\text{Li}_{0.33}\text{La}_{0.557}\text{TiO}_3$  (LLTO) nanofibers were fabricated by electrospinning and subsequent calcination processes. For the electrospinning solution, 3.3 mmol lithium nitrite ( $\text{LiNO}_3$ , Sigma-Aldrich), 5.6 mmol lanthanum nitrite hexahydrate ( $\text{La}(\text{NO}_3)_3 \cdot 6\text{H}_2\text{O}$ , Sigma-Aldrich) and 10 mmol titanium butoxide ( $\text{Ti}(\text{OC}_4\text{H}_9)_4$ , Sigma-Aldrich) were dissolved in 20 ml mixture solvent of dimethylformamide (DMF, Sigma-Aldrich)/acetic acid ( $\text{CH}_3\text{COOH}$ , Sigma-Aldrich) (8:2 by volume) and kept for 30 min under magnetic stirring. Then 2g polyvinylpyrrolidone (PVP,  $M_w=1,300,000$ , Sigma-Aldrich) was added and a yellow transparent solution was formed after stirring overnight. Precursor nanofibers were prepared by electrospinning of the mixture solution at a high voltage of 15 kV with a feeding rate of  $0.75 \text{ ml h}^{-1}$ . The distance between the stainless-steel needle and aluminum collector was fixed at 15 cm. As-spun nanofibers were subsequently calcined at different temperatures of 700, 800 and 900 °C for 2 h in air with a heating rate of  $5 \text{ }^\circ\text{C min}^{-1}$ .

### 5.2.2 Synthesis of LLTO nanofiber filled solid composite polymer electrolyte

A salt solution was first prepared by dissolving 0.5 g of bis(trifluoromethane)sulfonamide lithium (LiTFSI, Sigma-Aldrich) in 17.1 g acetonitrile ( $\text{CH}_3\text{CN}$ , Sigma-Aldrich). LLTO nanofibers with 10, 15 and 20 wt. % (based on the total weight of PEO and LiTFSI) were added into the above solution and sonicated for 10 min. Then 1 g poly (ethylene oxide) (PEO,  $M_w=600,000$ , Sigma-Aldrich) was added and the weight ratio of PEO/LiTFSI was fixed at 2:1. After magnetically

stirring overnight, the mixture was then directly dropped onto the stainless-steel spacer (1.89 cm<sup>2</sup>, MTI). Solid composite electrolytes were obtained after drying under vacuum at 60 °C overnight to totally remove the solvent.

### 5.2.3 Structure Characterization

Thermo-gravimetric analysis (TGA, Perkin Elmer Pyris 1) was conducted in air atmosphere with a heating rate of 20 °C min<sup>-1</sup> to examine the LLTO ceramic nanofiber formation during calcination process. Scanning electron microscopy (FE-SEM, FEI Verios 460L, USA) and aberration corrected scanning transmission electron microscopy (STEM, FEI Titan 80-300, USA) were used to identify the morphology of the LLTO nanofibers. X-ray diffraction (XRD) measurements were conducted by a Rigaku SmartLab X-ray diffractometer (Japan) with CuK $\alpha$  radiation (1.5418 Å) in a 2 $\theta$  range of 10° to 80°. Diffraction data were acquired using a step size and count time of 0.05° 2 $\theta$  and 3 sec/step, respectively.

### 5.2.4 Electrochemical performance characterization

For the ionic conductivity measurements, dried solid composite electrolyte membrane was sandwiched between two stainless steel electrodes and for each solid composite electrolyte membrane. Measurements were conducted on three samples for each composition. Electrochemical impedance spectroscopy (EIS) tests were carried out by Gamry Reference 600 devices from 1M Hz to 1Hz at an AC voltage of 5 mV. For linear sweep voltammetry tests, lithium

metal was used as the counter and reference electrode while stainless steel was the working electrode. The tests were conducted at a scan rate of  $10 \text{ mV s}^{-1}$ . Symmetric Li/solid composite electrolytes/Li cells were prepared using Li foil as the electrodes and tested at a current density of  $0.5 \text{ mA cm}^{-2}$  at  $25 \text{ }^\circ\text{C}$ . The cells were run for 0.5 h each cycle. The assembly was carried out in an argon filled glove box.

## 5.3 Results and Discussion

### 5.3.1 Morphology and Structure Characterization of LLTO Nanofibers

Figure 5.11a-d show SEM images of as-spun precursor nanofibers and the ceramic LLTO nanofibers calcined at different temperatures. Electrospun precursor nanofibers have uniform fibrous structure and smooth surface (Figure 1a) with the average fiber diameter of 770 nm (Figure 5.2a). Uniform LLTO nanofibers with very smooth surface appearance were formed after calcination at 700 °C and the average fiber diameter was 374 nm (Figures 5.1b and 5.2b). The average diameter of LLTO nanofibers decreased to 110 nm (Figure 5.2c) after calcination at a higher temperature of 800 °C and the surface of the nanofibers became rough on which small grains of LLTO could be clearly seen (Figure 5.1c). Furthermore, after calcination at 900 °C, the formation of large grains can be clearly seen in the LLTO fiber structure (Figure 5.1d). Diameter distribution of LLTO nanofibers after calcination at 900 °C was provided in Figure 5.2d and the average fiber diameter was found to be 212 nm. The fiber diameters after 900 °C calcination did not follow the normal distribution probably because of the irregular fiber diameter.

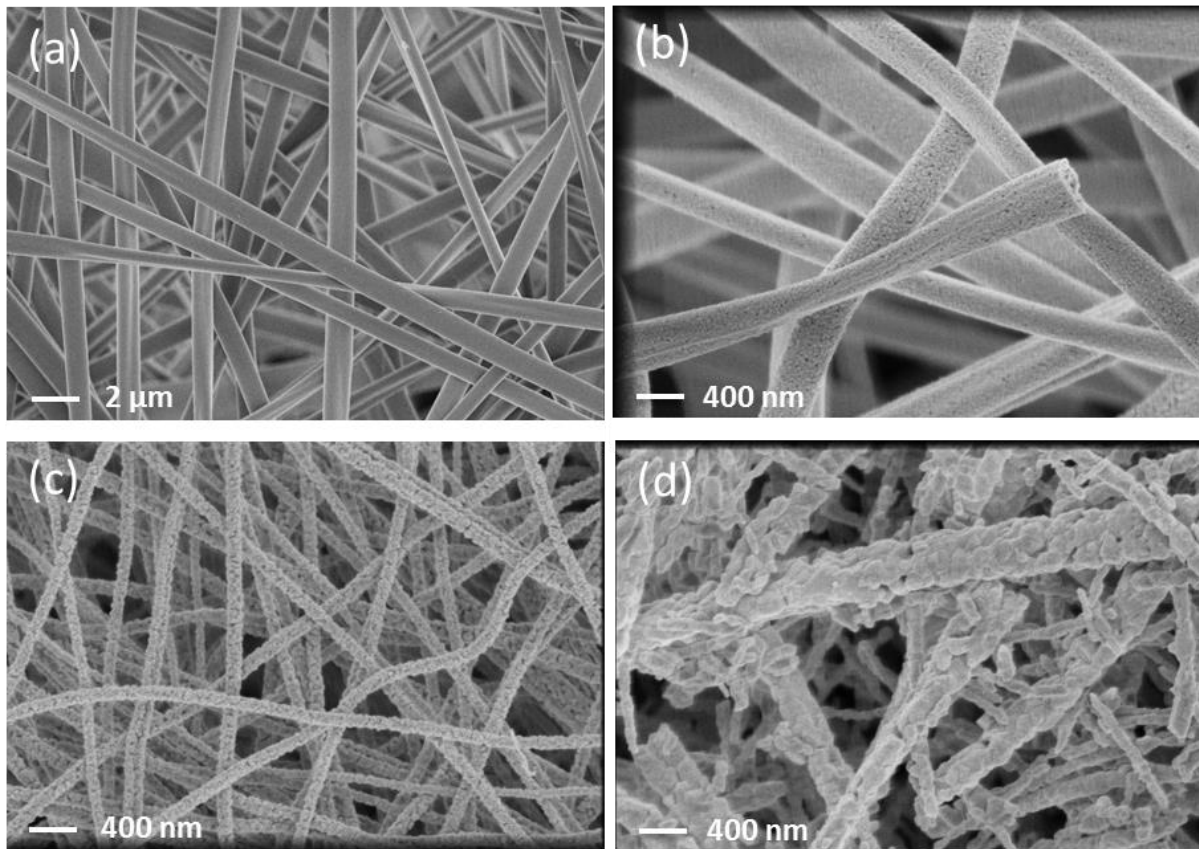


**Figure 5.1** SEM images of as-spun precursor nanofibers (a), LLTO nanofibers after calcination at (b) 700 °C, (c) 800 °C and (d) 900 °C for 2h.

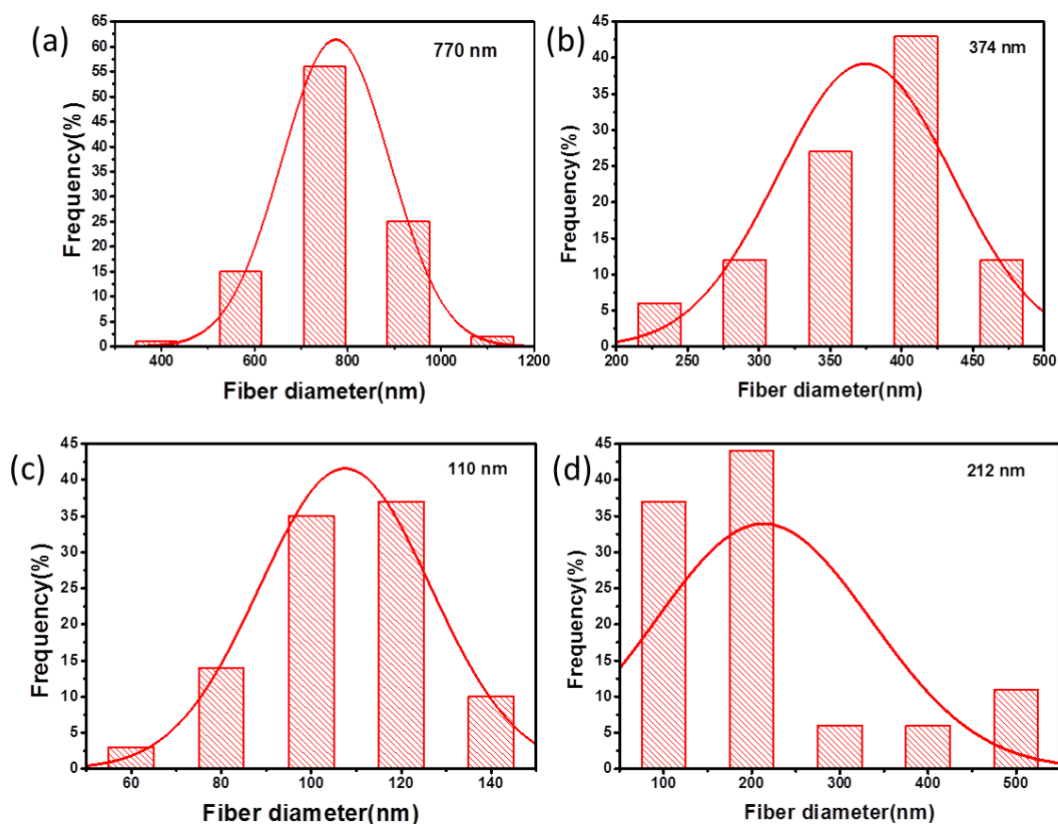


**Figure 5.2** Diameter distributions and average diameters of (a) as-spun precursor nanofibers, (b) LLTO nanofibers calcined at 700 °C for 2h and (c) LLTO nanofibers calcined at 800 °C for 2h, and (d) LLTO nanofibers calcined at 900 °C for 2h.

TGA was used to study the formation process of LLTO nanofibers during calcination and the result was shown in Figure 5.3a. From the TGA curve, no obvious weight loss was observed at above 730 °C, which indicates the formation of stable ceramic LLTO nanofibers. Figure 5.3b demonstrates the XRD patterns of LLTO nanofibers calcined at 700, 800 and 900 °C for 2h. Main peaks in the diffraction patterns of LLTO nanofibers calcined at 700, 800 and 900 °C were ascribed to the LLTO structure, which are consistent with the JCPDS card 01-087-0935 with tetragonal cell.

Between these three samples, LLTO nanofibers calcined at 800 °C was selected for further analysis because of the large and irregular fiber shape and the existence of large grains in LLTO structure when calcined at 700 and 900 °C, respectively.

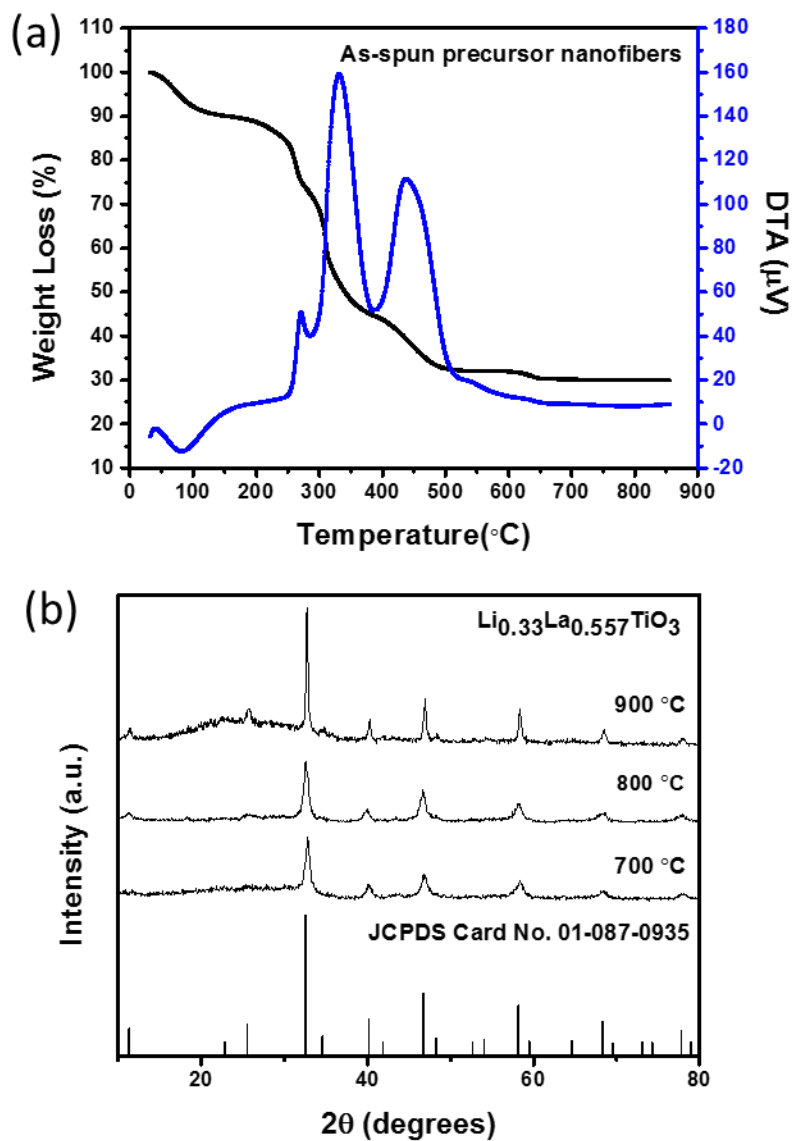


**Figure 5.3** (a) TGA curves of as-spun precursor nanofibers. (b) XRD patterns of the LLTO nanofibers calcined at 700, 800 and 900 °C for 2h.

TEM was used to identify the morphological features of individual LLTO nanofibers calcined at 800 °C. Identical features of LLTO ceramic structure could be observed in Figure 5.4a-b.<sup>33</sup> Figure 5.4c shows the corresponding selected area electron diffraction (SAED) patterns of LLTO nanofiber which could be ascribed to polycrystalline structure with tetragonal cell and it was consistent with the XRD results. Figure 5.4d exhibits the high-resolution TEM (HRTEM) image of a LLTO nanofiber. Observed lattice spacing from the HRTEM image of LLTO nanofiber was 0.27 nm, which corresponded to the (110) plane of LLTO. Based on the SEM, TEM, TGA and XRD results LLTO nanofibers calcined at 800 °C were considered as the filler for fabrication of solid composite electrolytes.

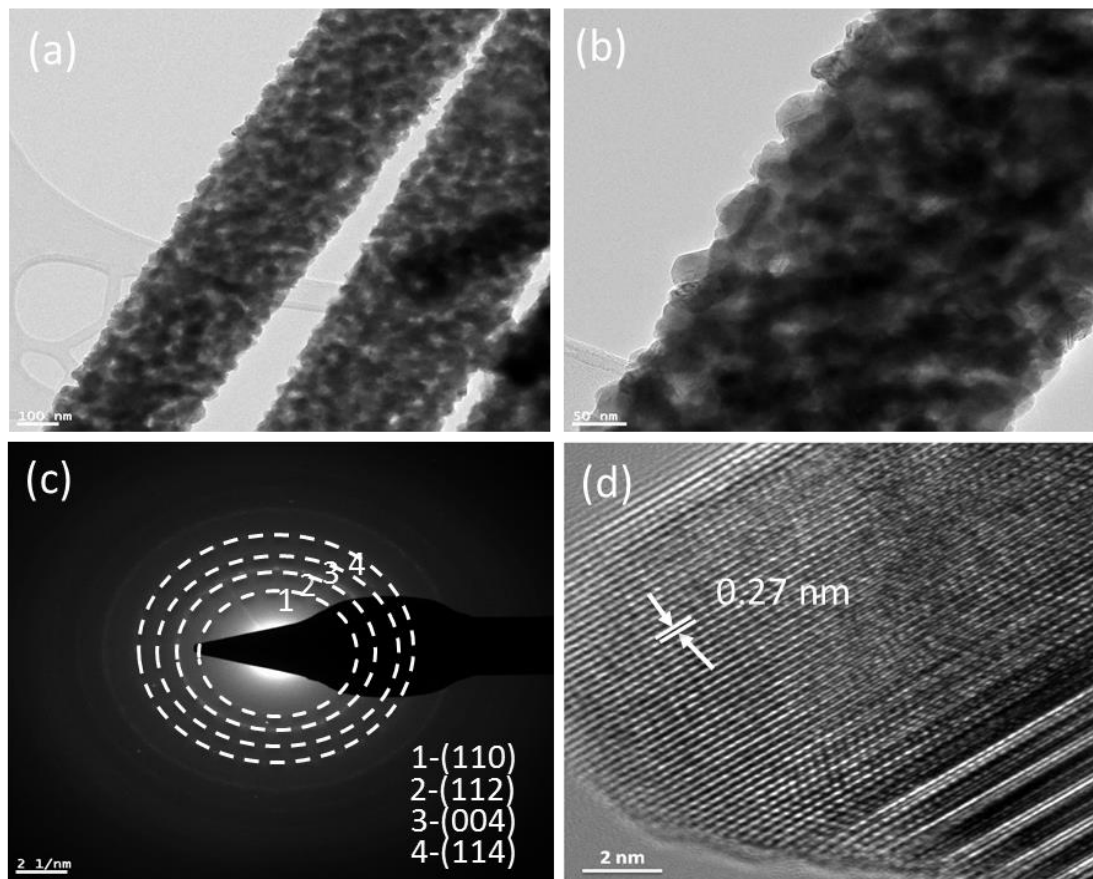


**Figure 5.4** (a, b) TEM images of LLTO nanofibers (800 °C) in different magnifications. (c) Corresponding selected area electron diffraction (SAED) patterns. (d) High-resolution TEM (HRTEM) image of an individual LLTO nanofiber.

### 5.3.2 Preparation and Characterization of Solid Composite Electrolyte

PEO/LiTFSI/LLTO solid composite electrolytes were prepared by dispersing LLTO nanofibers in PEO/LiTFSI salt/acetonitrile solution, followed by solvent removal. Figure 5.5a shows the EIS result of an LLTO plate calcined at 800 °C. The calculated ionic conductivity of LLTO was  $1.3 \times 10^{-4} \text{ S cm}^{-1}$ , which was comparable with that in the previous reported study.<sup>137</sup> In order to explore

the crystalline phase in PEO/LiTFSI/LLTO composite electrolytes with different LLTO nanofiber concentrations, XRD measurements were conducted and the results are shown in Figure 5.5b. Diffraction peaks observed at  $19.04^\circ$  and  $23.40^\circ$  were ascribed to the PEO crystalline structure, which is identical with the JCPDS card 00-052-2279. Besides, no obvious additional peaks were observed for LiTFSI, which indicates the complete dissolution of LiTFSI salts. All the electrolytes containing LLTO nanofibers showed typical diffraction peaks of the LLTO structure. It is worth to mention that dispersing LLTO nanofibers into the PEO matrix has influence on the crystallinity of PEO, and the relative intensity of the peaks corresponding to PEO decreased to the lowest level when 15 wt.% LLTO was added. However, after adding 20 wt.% LLTO, the relative peak intensity of PEO increased slightly, which was probably due to the accumulation of LLTO nanofibers in the PEO matrix and it was also revealed by the SEM images of solid polymer electrolytes with different LLTO concentrations. The PEO/LiTFSI/LLTO 20% indicated obvious overlap of LLTO nanofibers while the LLTO nanofibers were well-dispersed in the polymer matrixes with PEO/LiTFSI/LLTO 10% and 15% (Figure 5.6).<sup>50</sup> As a result of the aggregation of LLTO nanofibers in the PEO matrix, the ionic conductivity of PEO/LiTFSI/LLTO 20% was lowered. Figure 5.5c showed the XRD results of PEO/LiTFSI/LLTO particle 15% and it is clear that the crystallinity of PEO was higher than that of PEO/LiTFSI/LLTO 15%. These results revealed that more amorphous regions could be achieved in the PEO polymer matrix when 15% LLTO nanofiber fillers are added, which is important for the conductivity improvement of PEO/LiTFSI/LLTO composite electrolytes.

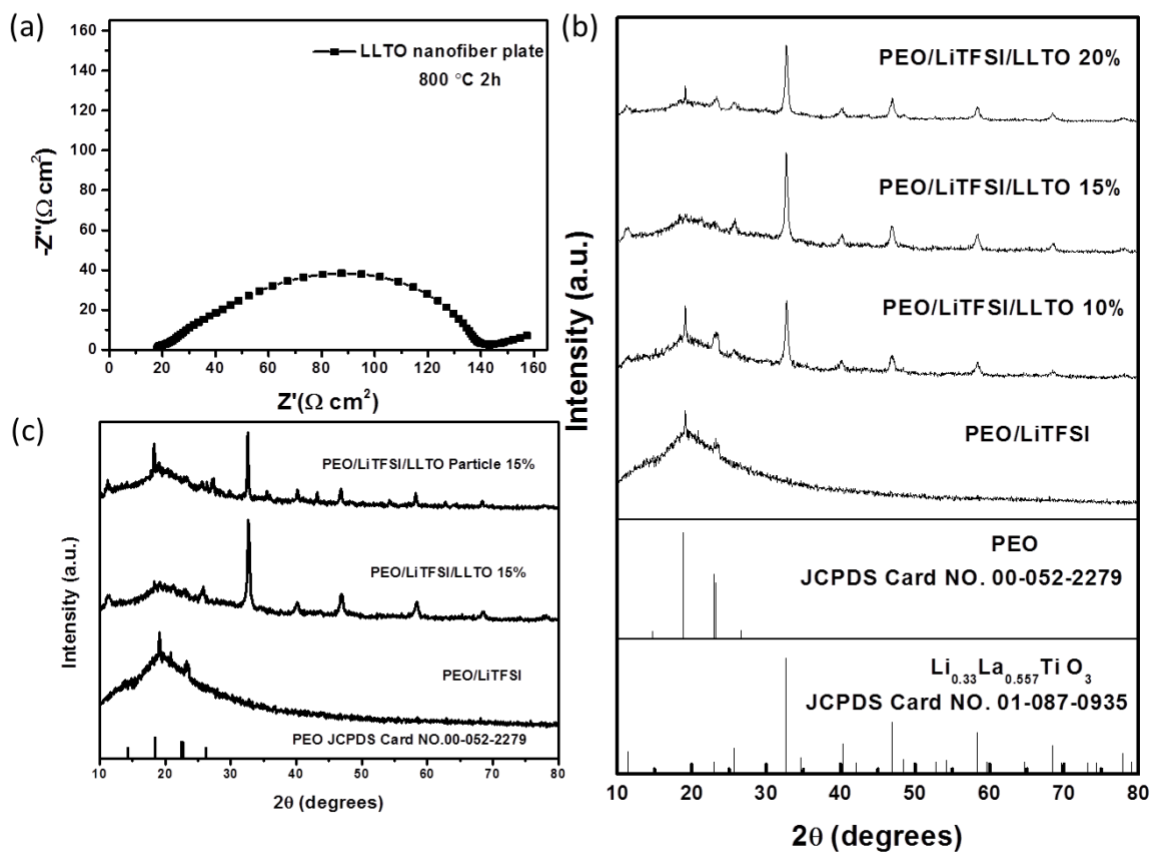


**Figure 5.5** (a) EIS curve of LLTO plate at room temperature. (b) XRD patterns of the PEO/LiTFSI/LLTO solid composite electrolytes with different LLTO nanofiber contents. (c) XRD patterns of the PEO/LiTFSI/LLTO solid composite electrolytes without and with 15 wt.% LLTO nanofiber/particle, showing the influence of LLTO morphology on the crystalline phase of PEO.

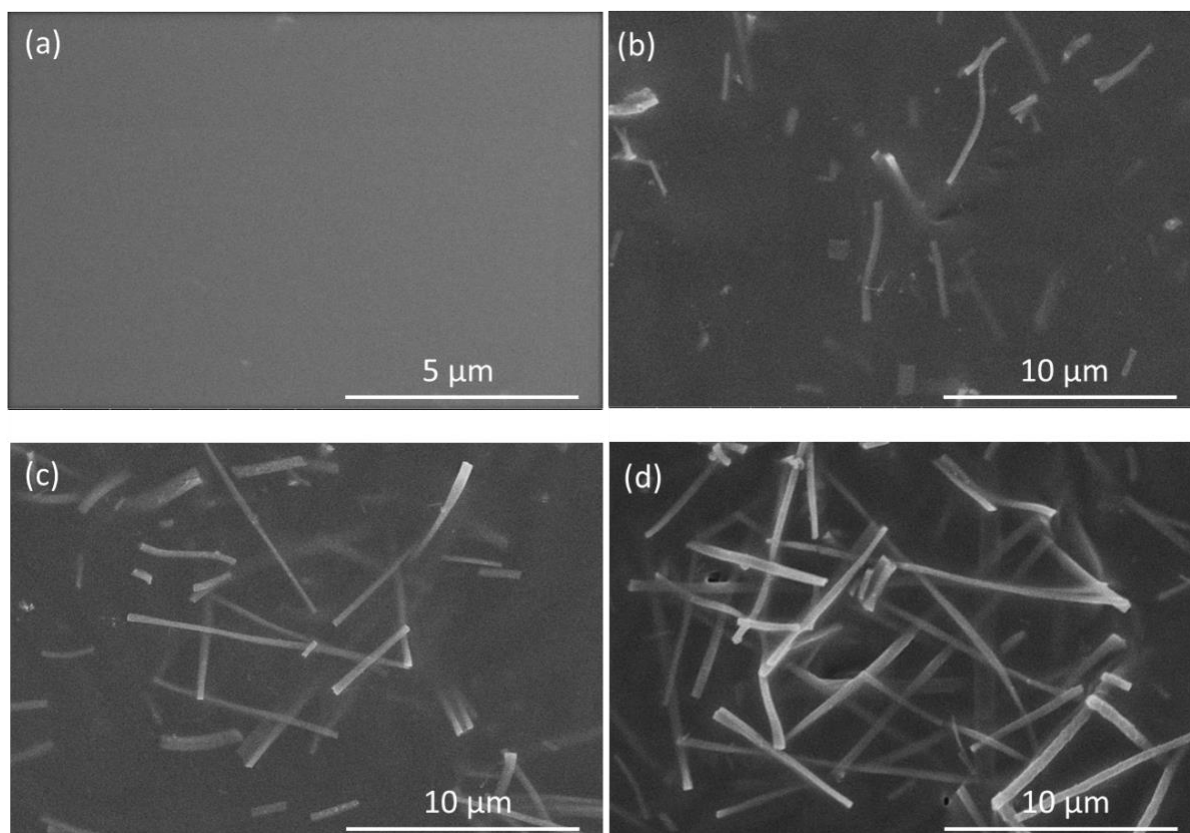


**Figure 5.6** SEM images of (a) PEO/LiTFSI, (b) PEO/LiTFSI/LLTO 10 wt.%, (c) PEO/LiTFSI/LLTO 15 wt.%, and (d) PEO/LiTFSI/LLTO 20 wt.% solid electrolytes.

It is worth to mention that in recently reported studies of PAN-LLTO, PEO-LLZO and PAN-LLZO solid electrolyte systems, Liu et al., Fu et al. and Yang *et al.* either claimed that the incorporation of LLTO or LLZO had no influence on the crystallinity of PAN polymer matrix or did not provide data regarding the crystallinity of the polymer matrix.<sup>32, 50, 138</sup> Our study clearly demonstrated the role of adding LLTO in decreasing the crystallinity of PEO matrix, which was important in the improvement of ionic conduction. Detailed comparison of those reported literatures was listed in Table 5-1. Low crystallinity of PEO mainly comes from the incorporation of LLTO nanofiber fillers. The 1D structure of LLTO nanofibers could contribute to increasing

the effective/conductive interface between the polymer chains and the ionic species, thus affecting the recrystallization kinetics of PEO.<sup>32-33, 50</sup>

**Table 5-1** Comparison between our research and the reported work in literature.

	<b>Crystallinity of polymer matrix after adding fillers</b>	<b>Concentration of nanofiber fillers in the polymer matrix</b>	<b>Proposed main conduction mechanism</b>	<b>Ionic conductivity (S cm<sup>-1</sup>)</b>	<b>Stability and voltage window of Li/composite electrolyte/Li cell</b>
LLTO nanofiber + PAN (Ref 32)	Not changed	Compared LLTO concentrations (0%, 5%, 10%, 15% and 20%)	5 1. Fast ion transport on LLTO nanofiber surface; 2. 3D ion-conducting network	$2.4 \times 10^{-4}$	No information
LLZO nanofiber + PEO (Ref 50)	No information	One LLZO/PEO ratio (1:4)	3D structure provides long-range ion transfer	$2.5 \times 10^{-4}$	Voltage value of around $\pm 300$ mV at $0.5 \text{ mA cm}^{-2}$ over 1000 h
LLZO nanofiber + PAN (Ref 138)	Not changed	Compared LLZO concentrations (0%, 1%, 2.5%, 5%, 10% and 15%)	6 1. Increased Li <sup>+</sup> dissociation from the ClO <sub>4</sub> <sup>-</sup> anion; 2. Preferred Li <sup>+</sup> diffusion at the LLZO/polymer interface	$1.31 \times 10^{-4}$	Voltage value of around $\pm 400$ mV at $50 \mu\text{A cm}^{-2}$ over 89 h
Our work	The crystallinity of PEO was lowered.	Compared LLTO concentrations (0%, 5%, 10%, 15% and 20%)	4 1. Creation of more amorphous region in the PEO matrix 2. Continuous ionic conductive pathways provided by 1D LLTO nanofibers	$2.4 \times 10^{-4}$	Voltage value of around $\pm 115$ mV at $0.5 \text{ mA cm}^{-2}$ over 720 h

### 5.3.3 Ionic Conductivity Measurement of Solid Composite Electrolyte

Ionic conductivities of PEO/LiTFSI/LLTO solid composite electrolytes were measured by EIS tests. The thickness of the solid composite electrolytes was around  $100 \pm 10 \mu\text{m}$ . Figure 5.7a demonstrates the EIS results of different solid composite electrolytes tested at room temperature. On the EIS, after fitting, well-defined semi-circle at high and middle frequencies could be ascribed to the combination of bulk resistance and bulk capacitance, which came from the migration of polymer chains and ions.<sup>32, 139</sup> Among all solid electrolytes studied, the PEO/LiTFSI/LLTO (15 wt.%) solid composite electrolyte demonstrated the lowest resistance. Figure 5.7b demonstrates the calculated ionic conductivity results of solid composite electrolytes with different LLTO concentrations tested at room temperature. It is clear that the ionic conductivities of PEO/LiTFSI solid composite electrolytes at room temperature reached to the maximum value of  $2.4 \times 10^{-4} \text{ S cm}^{-1}$  when 15 wt.% LLTO was incorporated. The ionic conductivities were  $1.75 \times 10^{-5}$ ,  $6.2 \times 10^{-5}$  and  $5.5 \times 10^{-5} \text{ S cm}^{-1}$  for PEO/LiTFSI, PEO/LiTFSI/LLTO (10 wt.%) and PEO/LiTFSI/LLTO (20 wt.%) solid electrolytes, respectively. Figure 5.8a indicates the temperature dependence of the ionic conductivity of PEO/LiTFSI/LLTO solid composite electrolytes with different LLTO nanofiber contents at the temperature range of 25 to 90 °C. The slopes in the Arrhenius plots indicate the conductivity changes in solid electrolytes, where the decrease in slope could lead to decrease in activation energy.<sup>50, 140</sup> It is obvious from the plots that compared to the PEO/LiTFSI solid electrolyte, increased ionic conductivities can be observed for all PEO/LiTFSI/LLTO solid composite electrolytes. PEO/LiTFSI/LLTO (15 wt.%) solid composite electrolyte showed the highest ionic conductivity, which was nearly one order of magnitude higher than that of the PEO/LiTFSI solid electrolyte at all temperatures. In addition, Figure 5.8b and c shows the EIS

result and Arrhenius plot of the PEO/LiTFSI/LLTO particle 15% solid composite electrolyte. PEO/LiTFSI/LLTO particle 15% solid composite electrolyte had an ionic conductivity of  $2.7 \times 10^{-5} \text{ S cm}^{-1}$  at 25°C, which was lower than those of the solid composite electrolytes with LLTO nanofiber fillers, indicating the benefits of the 1D nanofiber structure in conductivity enhancement.

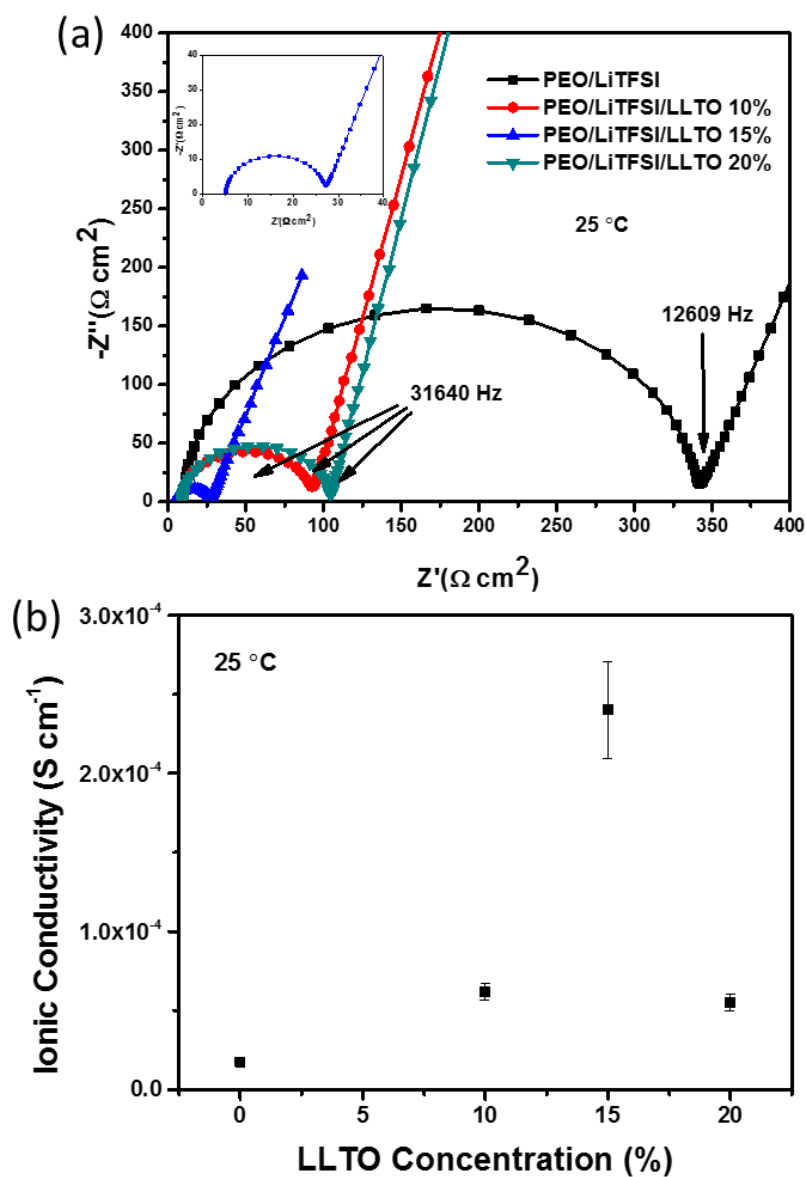


**Figure 5.7** (a) EIS results of the PEO/LiTFSI/LLTO solid composite electrolytes with different LLTO nanofiber contents at room temperature (Inset is the individual EIS figure for the PEO/LiTFSI/LLTO 15%). (b) Ionic conductivities of the PEO/LiTFSI/LLTO solid composite electrolytes with different LLTO nanofiber contents at room temperature.

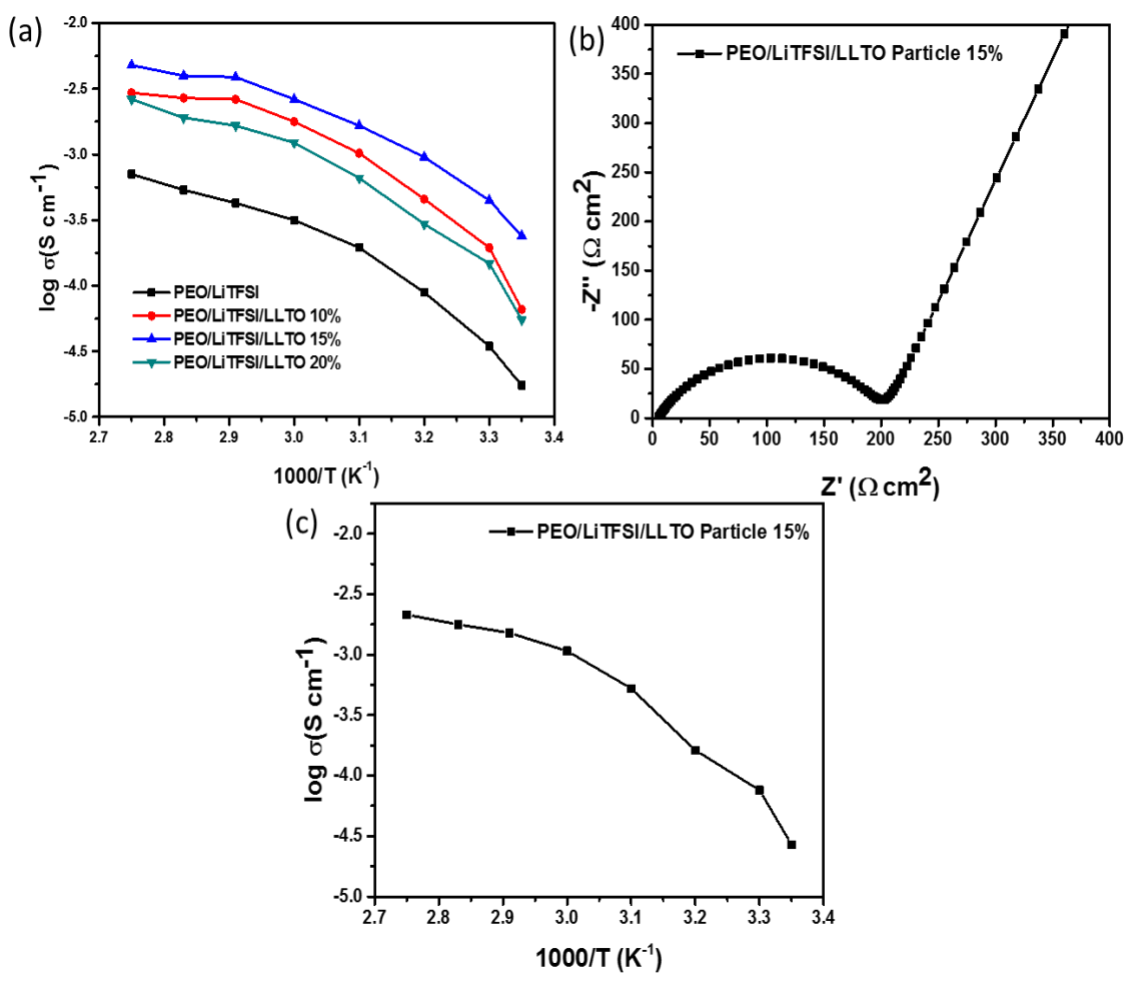


**Figure 5.8** (a) Arrhenius plots of the PEO/LiTFSI/LLTO solid composite electrolytes with different LLTO contents. (b) EIS result of the PEO/LiTFSI/LLTO particle solid composite electrolyte with 15% LLTO particles at room temperature. (c) Arrhenius plot of the PEO/LiTFSI/LLTO particle solid composite electrolyte with 15% LLTO particles.

### 5.3.4 Activation Energy Calculation

Besides, it is well known that the relationship between ionic conductivity and temperature follows the traditional Arrhenius equation:

$$\sigma(T) = A \exp(-E_a / RT) \quad (5.1)$$

where  $T$  is the absolute temperature,  $A$  is a pre-exponential factor,  $E_a$  is the activation energy, and  $R$  is the universal gas constant ( $8.314 \text{ J mol}^{-1}$ ). Based on this equation, it is clear that the reduction of  $E_a$  leads to increase in ionic conductivity. Table 5-2 shows the calculated activation energies of PEO/LiTFSI/LLTO solid composite electrolytes with different LLTO concentrations. PEO/LiTFSI/LLTO (15 wt.%) solid composite electrolyte showed the lowest activation energy of 0.40 eV (0.52, 0.48 and 0.48 eV, respectively, for PEO/LiTFSI, PEO/LiTFSI/LLTO (10 wt.%) and PEO/LiTFSI/LLTO (20 wt.%) solid electrolyte), which is consistent with the Arrhenius plots on which the PEO/LiTFSI/LLTO (15 wt.%) solid composite electrolyte exhibited the smallest slope with the lowest activation energy.

**Table 5-2** Activation energies of solid composite electrolytes with different LLTO concentrations below 60 °C.

<b>Weight Ratio (wt.% LLTO)</b>	0	10	15	20
<b>Activation Energy (eV)</b>	0.52	0.48	0.40	0.48

Prominent conductivity of the PEO/LiTFSI/LLTO 15 wt.% solid composite electrolyte could be ascribed to following reasons. On one hand, compared with the PEO/LiTFSI solid electrolyte, the incorporation of LLTO nanofibers into PEO matrix provided more effective contact with PEO polymer and decreased the crystallinity of PEO polymer, thus more amorphous region was created within the PEO polymer for better ion conduction. On the other hand, LLTO is a perovskite-type lithium ion conductor with rich vacancies on the surface region and lithium ions could hop along the vacancies in LLTO by replacing a nearby vacancy.<sup>50</sup> Therefore, the 1D structure of LLTO nanofibers with high surface area could provide a fast/continuous ionic pathway for Li ions. As a result of the combined advantages of enriched amorphous region and continuous ionic pathway, the PEO/LiTFSI/LLTO composite electrolyte exhibited lower activation energy and higher ionic conductivity.

### 5.3.5 Electrochemical Stability Window

Since a large electrochemical window is a desirable factor for the electrolytes of high-voltage lithium batteries, linear sweep voltammetry (LSV) was carried out to test the electrochemical stability of PEO/LiTFSI and PEO/LiTFSI/LLTO 15 wt.% solid composite electrolytes. For LSV testing, stainless steel was used as the working electrode and lithium foil was used as the counter and reference electrodes. Linear sweep voltammetry curve of two solid composite electrolytes are demonstrated in Figure 5.9. It is seen that the PEO/LiTFSI/LLTO 15 wt.% composite electrolyte exhibited a stable voltage window up to 5V vs Li/Li<sup>+</sup>, indicating that this solid composite electrolyte could satisfy the requirements of most high-voltage lithium battery applications. On the

other hand, PEO/LiTFSI solid electrolyte showed an obvious peak above 3V, indicating the instability of this solid polymer electrolyte without LLTO nanofibers.

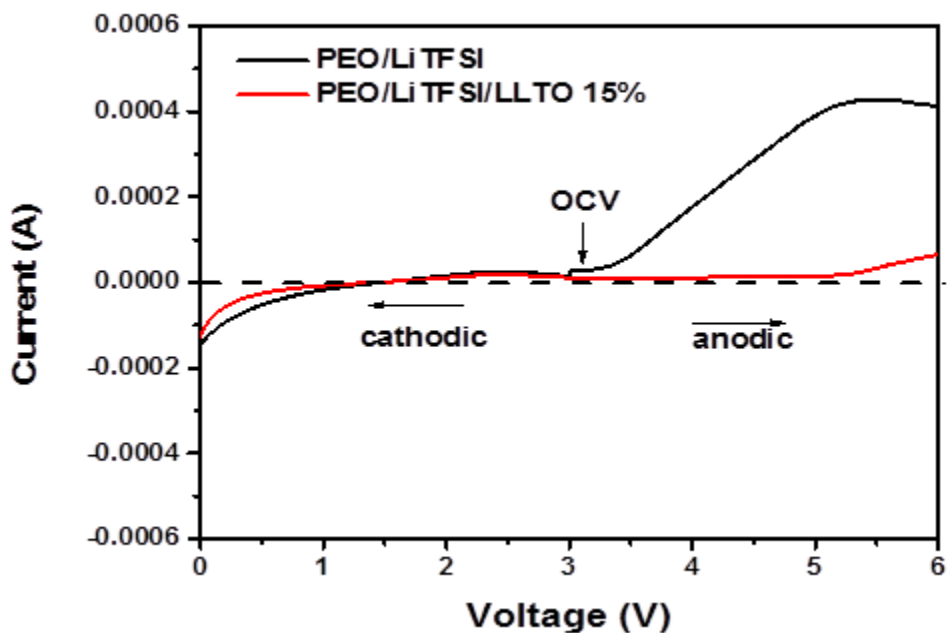


**Figure 5.9** Linear Sweep voltammetry curve of PEO/LiTFSI and PEO/LiTFSI/LLTO 15 wt.% solid composite electrolytes.

### 5.3.6 Voltage Profiles of Symmetric Li Cell

In addition, to further identify the interface stability of PEO/LiTFSI/LLTO 15 wt.% solid composite electrolyte, symmetric hybrid cell (Li/solid composite electrolyte/Li) was fabricated and tested for 0.5 h (each cycle) with a constant current density of  $0.5 \text{ mA cm}^{-2}$  at  $25 \text{ }^\circ\text{C}$ . The result is shown in Figure 5.10. The negative voltage represents Li plating and the positive voltage

indicates Li stripping.<sup>32</sup> The cell exhibited a relatively stable voltage of around  $\pm 115$  mV after 720 h cycling and this voltage value is much lower than the previously reported voltage value of symmetric cell with LLZO/PEO solid polymer electrolyte ( $\pm 300$  mV) tested at the same current density.<sup>32</sup> The smooth voltage curve indicated the relatively stable interfacial resistance between Li and the PEO/LiTFSI/LLTO 15 wt.% solid composite electrolyte, which is beneficial for the applications in lithium batteries.

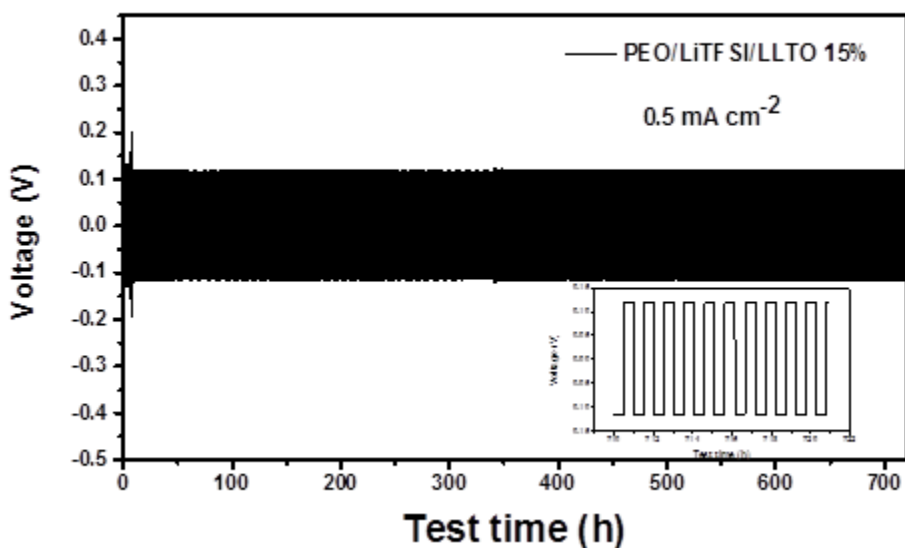


**Figure 5.10** Voltage profile of the continued lithium plating/stripping cycling of PEO/LiTFSI/LLTO 15 wt.% solid electrolyte tested at a current density of  $0.5 \text{ mA cm}^{-2}$  at  $25 \text{ }^\circ\text{C}$  (Insert: voltage profiles of PEO/LiTFSI/LLTO 15 wt.% solid electrolyte tested at 710 - 720 h).

## 5.4 Conclusion

In summary, ceramic LLTO nanofibers with high aspect ratio were successfully prepared by a simple electrospinning and subsequent calcination processes. LLTO nanofibers were further dispersed into PEO polymer to fabricate the PEO/LLTO composite solid polymer electrolytes. Incorporation of LLTO nanofibers in the PEO matrix has significantly influenced the overall performance of solid composite polymer electrolytes: LLTO nanofibers, with high aspect ratio, provided continuous ionic conductive pathways for the ion transport and simultaneously they limited the recrystallization kinetics of the PEO chains and maintained the lower crystallization of PEO matrix. Hence, the PEO/LiTFSI/LLTO composite electrolyte, with 15 wt. % of LLTO nanofibers respect to the total PEO and LiTFSI amount, showed a high ionic conductivity of  $2.4 \times 10^{-4} \text{ S cm}^{-1}$  at room temperature, which is nearly one order of magnitude higher than that of bare PEO/LiTFSI polymer electrolyte. In addition, for PEO/LiTFSI/LLTO composite electrolyte, a considerably enlarged electrochemical stability window was achieved, which could endure up to 5V vs Li/Li<sup>+</sup> and could satisfy most lithium-based batteries. Therefore, it is demonstrated that PEO/LiTFSI/LLTO composite solid electrolyte, with high ionic conductivity and large electrochemical stability window, opens an opportunity for next-generation high-energy density and safe lithium batteries.

## **CHAPTER 6            FLEXIBLE ELECTROLYTE-CATHODE BILAYER FRAMEWORK WITH STABILIZED INTERFACE FOR ROOM-TEMPERATURE ALL-SOLID-STATE LITHIUM-SULFUR BATTERIES**

### **Abstract**

Lithium-sulfur batteries (LSBs) have been regarded as the promising next-generation energy storage system beyond state-of-the-art lithium-ion batteries because of their low cost and high energy density. To avoid the “polysulfide shuttle” in liquid LSBs and to address safe concerns originated from the use of flammable liquid organic electrolyte and the formation of lithium dendrites, all-solid-state LSBs (ASSLSBs) have gained extensive attention recently. The key issues restrict the realization of ASSLSBs lie in the low ionic conductivity of solid electrolytes, the insufficient contact between electrode/electrolyte interfaces and the poor electrical/ionic conductivities of S and its discharge products. Here, we report a novel bilayer framework through integrating three-dimensional (3D) carbon nanofiber/sulfur (CNF/S) cathode with one-dimensional (1D) ceramic LLTO nanofiber incorporated PEO composite solid electrolyte for room-temperature ASSLSBs. The stabilized cycling performance of this novel bilayer structure design lies in the reduced interfacial resistance and enhanced interfacial stability between electrode/electrolyte interfaces due to the addition of  $\text{Li}^+$  conducting 1D LLTO nanofibers, as well as the formed fast-continuous electron/ion transportation pathways within the 3D cathode architecture. Meanwhile, the mechanically robust bilayer framework with micro-/meso- pores could also accommodate the large volume change of sulfur during continuous charge-discharge process and help suppress the Li dendrite formation. As a result of the aforementioned benefits of

the novel bilayer structure design, the introduced ASSLSBs could deliver a stable cycling performance at room temperature with high coulombic efficiency of over 99%.

**Key Words:** composite solid polymer electrolyte, all-solid-state batteries, lithium-sulfur batteries, lithium dendrite, room temperature.

## 6.1 Introduction

Lithium sulfur (Li-S) batteries have gained attention as a promising energy storage system because sulfur (S) has high theoretical capacity of 1675 mAh g<sup>-1</sup> and is abundant on earth, which is ideal for broad applications like electrical vehicles (EVs).<sup>1, 56</sup> However, the practical application of Li-S batteries is severely restricted by the continuous capacity fading, coming from the shuttle effect of soluble discharge intermediate “polysulfides” in liquid electrolyte and the safety concerns originated from the use of flammable organic solvents and the formation of lithium dendrites.<sup>24, 57</sup> The replacement of liquid electrolytes with solid electrolytes has been regarded as the fundamental approach to address the aforementioned problems.<sup>141</sup> In this view, various types of solid electrolytes, including gel electrolytes, ceramic electrolytes, polymer electrolytes and composite electrolytes, have been evaluated in Li-S batteries to suppress the polysulfide shuttle (improve the specific capacity) and eliminate the safety concerns caused by liquid electrolytes and lithium dendrites.<sup>13, 142-143</sup> Li-S cells using those solid electrolytes need to be operated at 60 °C or higher with the aim of getting better contact and higher ionic conductivity, even at a low active material loading (around 0.5 mg cm<sup>-2</sup>).<sup>144-146</sup> The temperature above 60 °C is far beyond the operation limits of most practical battery applications.<sup>28, 147</sup> Hence, in order to enable the safe operation of all-solid-state Li-S batteries (ASSLSBs) at room temperature (RT), solid electrolytes with high RT ionic conductivity and small interfacial resistance at the electrode/electrolyte interfaces are urgently needed.<sup>141</sup>

In addition to the development of suitable solid electrolytes, it is essential to offer a network skeleton with high electrical conductivity for the S loading within the cathode of ASSLSBs since S is electrically insulating. In this respect, composite S cathode structures with reduced graphene

oxide and carbon black have been explored to improve the electrical conductivity in ASSLSBs.<sup>53</sup>  
<sup>148</sup> Recent reported works by Xu et al. and Wang et al. also concluded that the S cathode should also be ionically conductive as well because the interfacial ion transport between the active material and the solid electrolytes plays a crucial role in completing the electrode reactions of RT-ASSLSBs. Hence, it is essential to develop a balanced dual-conductive (electrical and ionic) matrix for the sulfur cathode.<sup>27, 53</sup> Furthermore, the large volume change of S during lithiation/delithiation leads to active material detachment from conductive additives and destroys the structural integrity of the cathode, and the problem becomes even worse in solid-electrolyte system as the S cathode always consists of a thick-complex composite of active material (S), conductive additive and solid electrolyte.<sup>27</sup> When the detachment of active materials from the conductive additive/solid electrolyte takes place during discharge/charge process, the conductive pathways for electrons and ions are interrupted, leading to a fast capacity decay of ASSLSBs.<sup>27</sup> To address this issue, a mechanically robust conductive matrix should be introduced.

Taking into consideration all the above-mentioned issues regarding the solid electrolyte and S cathode, it seems that a smart electrolyte/electrode integrated architecture with high ionic conductivity and small interfacial resistance at RT should be developed. Here, we report a novel composite framework of one-dimensional (1D)  $\text{Li}_{0.33}\text{La}_{0.557}\text{TiO}_3$  (LLTO) ceramic nanofiber/poly(ethylene oxide) (PEO) composite electrolyte enhanced three-dimensional (3D)-flexible carbon nanofiber/sulfur (CNF/S) cathode for RT-ASSLABs (Figure 6.1). The key aspect of this study is to integrate highly Li ion conductive/mechanically robust solid composite polymer electrolyte with dual-conductive matrix in one novel bilayer structure design, which reconciles the conductivity-rigidity inconsistency and satisfies multiple requirements for RT-ASSLSBs. The

advantages of this novel bilayer structure design with thin LLTO incorporated solid composite electrolyte layer lie in the following aspects: *i)* dispersing 1D LLTO nanofibers within the polymer matrix provides continuous ionic conductive pathways for the ion transfer in solid polymer electrolyte and enhances amorphous region in the PEO matrix; *ii)* the LLTO nanofibers on/within the thin PEO solid polymer electrolyte enable facial ion transport and reduce the interfacial resistance at the electrolyte/electrode interface; *iii)* since the liquid PEO/LLTO solid electrolyte was infiltrated onto the surface and pores of CNF/S nanofibers (similar to liquid electrolyte), a balanced conducting matrix with high electrical and ionic conductivities is achieved; *iv)* the uniform distribution of nano-sized S along the CNF axis could shorten the diffusion distances for both  $\text{Li}^+$  and electrons; *v)* the mechanically robust cathode with micro-/meso- pores could accommodate the large volume change during continuous charge-discharge process, and *vi)* the entire bilayer structure can be placed on the top of the anode surface to form a full Li-S cell without the additional electrolyte or separator layer. With all those advantages, our novel 1D LLTO nanofiber enhanced CNF/S-PEO/LLTO bilayer framework demonstrates favorable electrochemical performance at RT with high coulombic efficiency of over 99%. Therefore, it is demonstrated that this study provides a promising strategy in dealing with multiple challenges of RT-ASSLSBs.

## 6.2 Experimental

### 6.2.1 PEO/LLTO solid electrolyte preparation

$\text{Li}_{0.33}\text{La}_{0.557}\text{TiO}_3$  (LLTO) nanofibers were prepared by electrospinning and subsequent high temperature calcination process. The starting materials for the electrospinning solution were lithium nitrate ( $\text{LiNO}_3$ , Sigma-Aldrich), lanthanum nitrate hexahydrate ( $\text{La}(\text{NO}_3)_3 \cdot 6\text{H}_2\text{O}$ , Sigma-Aldrich) and titanium butoxide ( $\text{Ti}(\text{OC}_4\text{H}_9)_4$ , Sigma-Aldrich). Stoichiometric amounts of these materials were first dissolved in a mixture solvent of dimethylformamide (DMF, Sigma-Aldrich)/acetic acid ( $\text{CH}_3\text{COOH}$ , Sigma-Aldrich) (8:2 by volume) and kept for 30 min under magnetic stirring. Then 2g polyvinylpyrrolidone (PVP,  $M_w=1,300,000$ , Sigma-Aldrich) was added into the solution as the polymer support in the electrospinning process. A high voltage of 15 KV with a feeding rate of  $0.75 \text{ ml h}^{-1}$  was applied to get the as-spun precursor nanofibers. LLTO nanofibers were obtained after calcination of as-spun precursor nanofibers at  $800 \text{ }^\circ\text{C}$  for 2h in air.

PEO/LLTO solid polymer electrolyte was prepared using the formula below: first, 0.5 g bis(trifluoromethane)sulfonamide lithium (LiTFSI, Sigma-Aldrich) and 0.225 g LLTO were added in 17.1 g acetonitrile ( $\text{CH}_3\text{CN}$ , Sigma-Aldrich); then poly (ethylene oxide) (PEO,  $M_w=600,000$ , Sigma-Aldrich) was added with the fixed weight ratio of PEO/LiTFSI (2:1). PEO/LLTO solid polymer electrolyte was obtained after drying at  $60 \text{ }^\circ\text{C}$  overnight under vacuum.

### 6.2.2 CNF/S-PEO/LLTO Bilayer Framework Preparation

CNFs were prepared by carbonization of as-spun polyacrylonitrile (PAN, Mw=150,000, Sigma-Aldrich) nanofibers as we reported before.<sup>149</sup> First, a viscous electrospinning solution consisting of 3 g PAN and 27 g *N, N*-dimethylformamide (DMF, >99.5%, Sigma-Aldrich) was prepared. Then the solution was electrospun into PAN nanofibers at a high voltage of 15 KV with a feeding rate of 0.75 ml h<sup>-1</sup>. CNFs were obtained by stabilizing as-spun PAN nanofibers at 280 °C for 5 h in air (5 °C min<sup>-1</sup>), followed by carbonization in nitrogen atmosphere at 1000 °C for 1 h (2 °C min<sup>-1</sup>). CNF/S electrode was fabricated by directly dropping 10 μL S/carbon disulfide (CS<sub>2</sub>, Fisher Scientific) solution (127 mg S in 1 ml CS<sub>2</sub>) onto the pre-punched CNF mat (1.27 cm<sup>2</sup>). For the preparation of bi-layer CNF/S-PEO/LLTO electrode, 30 μL PEO/LLTO solution was directly dropped onto the CNF/S electrode and then dried in the vacuum oven at 60 °C overnight to completely remove the solvent.

### 6.2.3 Structure Characterization

The surface morphology and structure features were characterized by field-emission scanning electron microscopy (FE-SEM, FEI Verios 460L, USA) with an energy dispersive X-ray spectroscopy (EDS) detector. Aberration corrected scanning transmission electron microscopy (STEM, FEI Titan 80-300, USA) was used to identify the structure and morphology of the samples. X-ray diffraction (XRD) measurements were conducted by a Rigaku SmartLab X-ray diffractometer (Japan) in a 2θ range of 10-80 ° with CuKα radiation (1.5418 Å). Differential scanning calorimetry (DSC) was carried out at a heating/cooling rate of 2 °C min<sup>-1</sup> using a TA Instrument Discovery Series.

#### 6.2.4 Electrochemical Characterization

The ionic conductivity measurement was conducted by sandwiching dried solid PEO and PEO/LLTO electrolytes between two stainless steel electrodes. Electrochemical impedance spectroscopy (EIS) tests were carried out by Gamry Reference 600 devices in a frequency range of 100 kHz to 1 Hz at an AC voltage of 5 mV. For the electrochemical stability window test, lithium metal foil was used as the counter electrode and stainless steel electrode was the working electrode. The test was carried out at a scan rate of 10 mV s<sup>-1</sup> with a voltage range of 2.8-1.7 V. To study the interfacial stability, symmetric Li/electrolyte/Li cells were tested at a current density of 0.5 mA cm<sup>-2</sup> and run for 0.5 h each cycle at room temperature (25 °C).

All-solid-state Li-S cell was assembled using Li foil as the anode without adding any liquid electrolyte. Cycling performance of all-solid-state Li-S cell was tested by Arbin battery tester with a potential range of 2.8-1.7 V at a current density of 0.05 C. The cell assembly was carried out in the argon filled glove box and the capacities were calculated based on the total sulfur mass in the cathode.

## 6.3 Results and Discussion

### 6.3.1 Fabrication and Characterization of Novel CNF/S-PEO/LLTO Bilayer Structure

The bilayer structure was prepared by direct casting PEO/LLTO solution onto the CNF/S cathode and subsequent integration of LLTO nanofiber and CNF/S cathode through PEO polymer during solvent evaporation. Details of the fabrication process are given in the Experimental section.

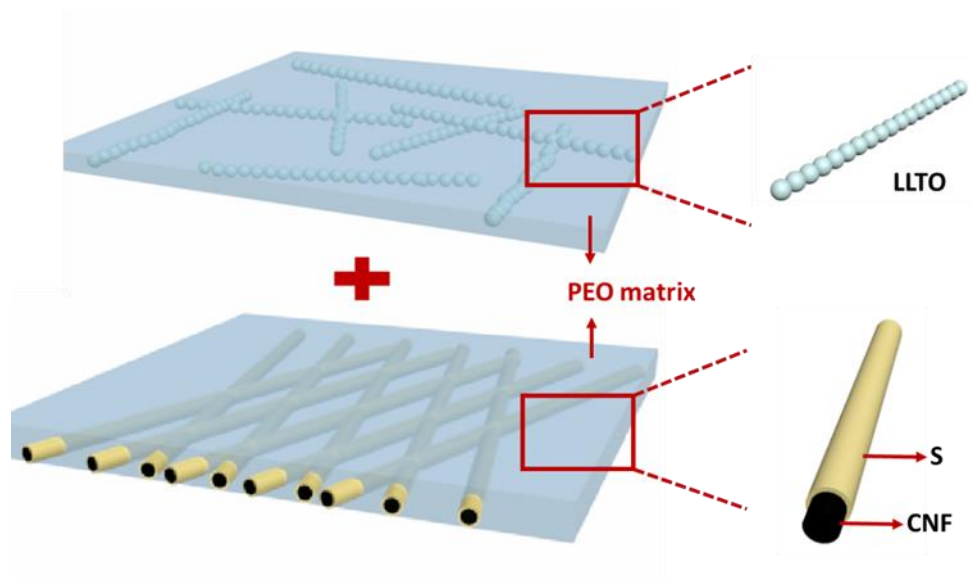


**Figure 6.1** Schematic illustration of the novel 1D LLTO nanofiber enhanced composite CNF/S-PEO/LLTO cathode structure design: the top thin PEO/LLTO solid polymer electrolyte layer acts as the Li ion conductor that ensures the fast facial ion transport between cathode and anode while the incorporation of ceramic LLTO also improves the interfacial stability; the bottom PEO filled 3D CNF/S layer with intimate triple-phase contact of electrical conductive current collector (CNF), active material (S) and solid polymer electrolyte (PEO) provides a balanced dual-conductive architecture for continuous electron/ion transfer. The entire bi-layer structure can be placed on the

top of the anode surface to form a full Li-S cell without the use of additional electrolyte or separator layer.

Figure 6.2a shows the scanning electron microscopy (SEM) image of a CNF mat with randomly arranged nanofibers forming a network structure. The average fiber diameter of CNFs was 224 nm (Figure 6.2b) and the diameter slightly increased to 237 nm after incorporation of S as indicated in Figure 6.2c. The BET measurement result indicates that the CNFs have a large surface area of  $1375 \text{ m}^2 \text{ g}^{-1}$  with abundant micro- and meso-pores (Figure 6.3). It is worth to mention that the small fiber diameter as well as the large surface area of CNFs was beneficial for the uniform distribution of S as the nanofiber surface could provide sufficient conductive sites and further promote the surface reactions.<sup>149</sup>

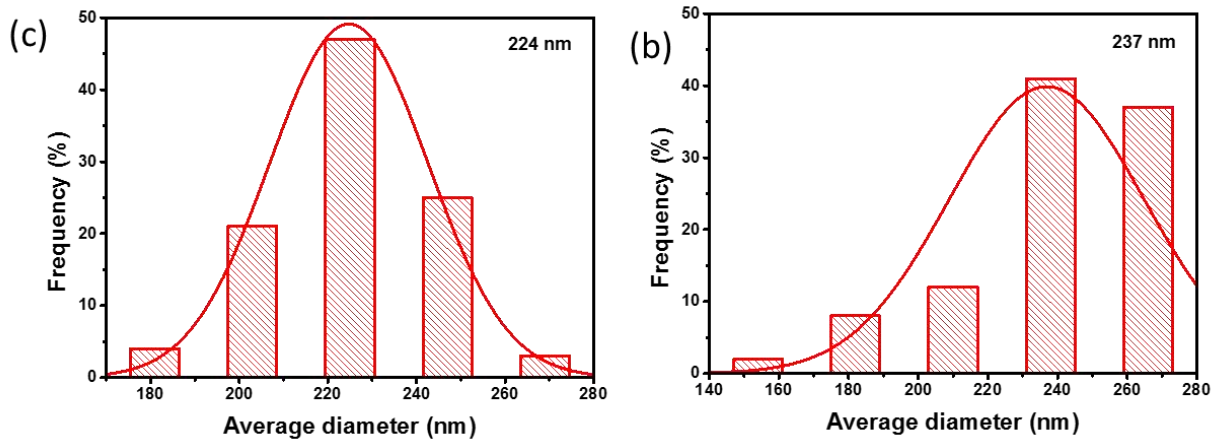
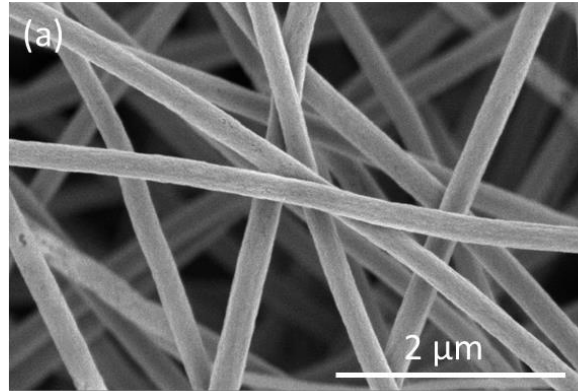


**Figure 6.2** (a) SEM image of CNFs. Diameter distributions and average fiber diameters of (b) CNFs and (c) CNF/S.

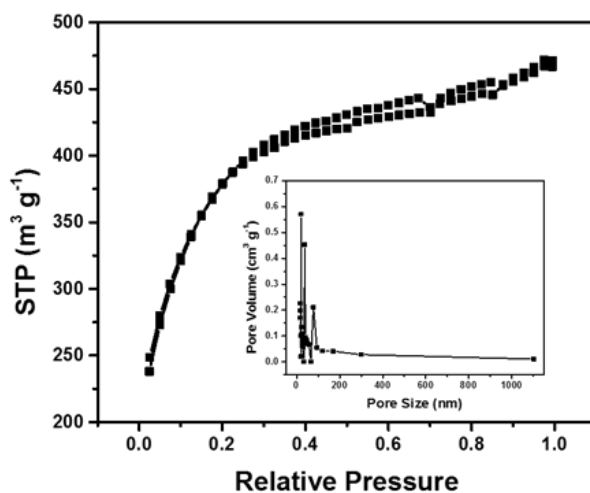


**Figure 6.3** N<sub>2</sub> isothermal adsorption curves of CNF (inserted: corresponding pore size distribution curve).

Figure 6.4a indicates the surface morphology of the as-prepared CNF/S electrode. As expected, no obvious morphology change could be observed after incorporation of S, indicating the uniform distribution of S along the fiber axis. The CNF/S electrode was prepared by dropping a mixed liquid solution of S/carbon disulfide (S/CS<sub>2</sub>) onto the CNF mat (as it has been reported in our previous study<sup>149</sup>), ensuring the intimate contact between the active material (S) and the current collector (CNF mat). The interconnected CNF network structure was also beneficial for the long-range electron transfer through the electrode. Figure 6.4b shows the surface morphology of the as-prepared PEO/LLTO solid polymer electrolyte. LLTO nanofibers were prepared by electrospinning of the precursor polymer/salt solution and followed by high-temperature calcination.<sup>150</sup> It is seen that the 1D LLTO nanofibers were randomly distributed within the PEO polymer matrix. Typical LLTO nanofiber morphology with small grains arranged in the fiber axis

could be clearly seen in Figure 6.4c. The CNF/S-PEO/LLTO composite electrode was obtained by dropping PEOLLTO solution onto the CNF/S mat.

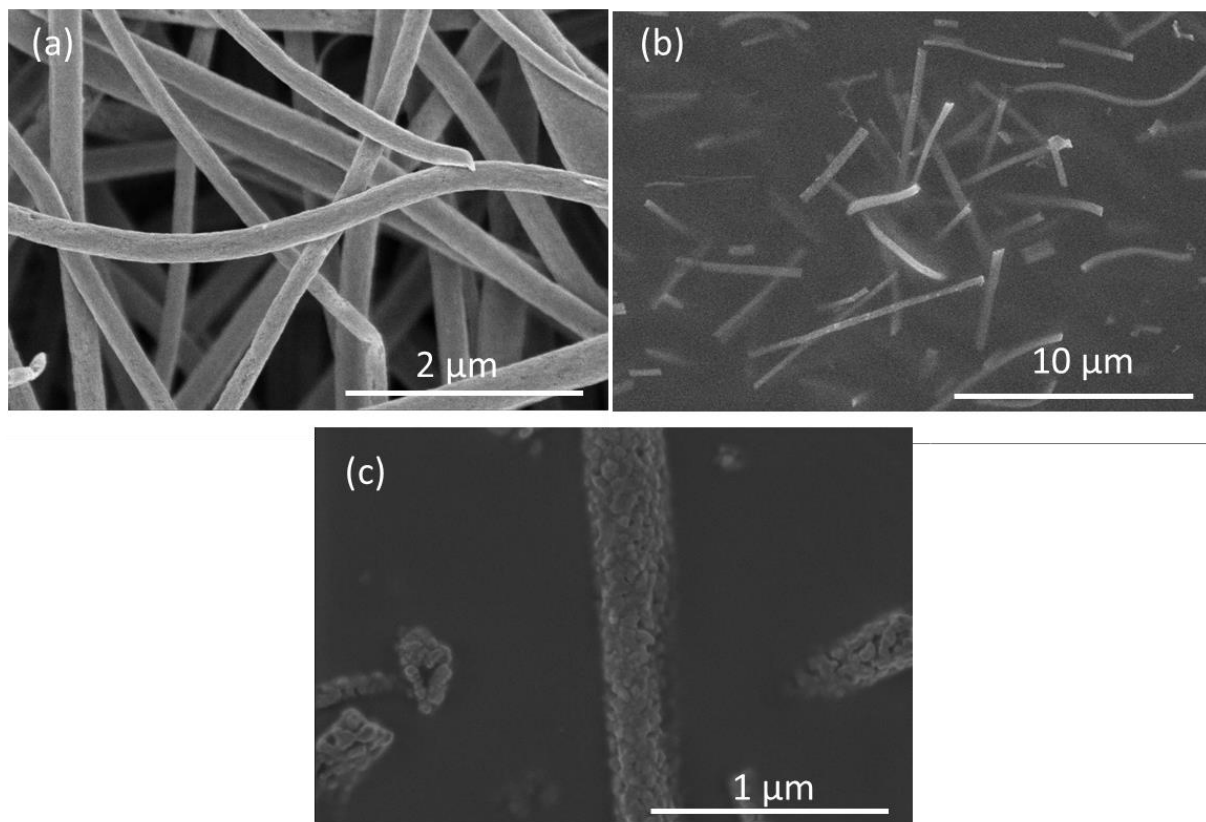


**Figure 6.4** SEM images of (a) CNF/S, (b) PEO/LLTO solid polymer electrolyte. (c) High resolution SEM image of PEO/LLTO solid polymer electrolyte with clearly seen LLTO structure.

Figure 6.5a shows the cross-sectional SEM image of the framework structure, containing a composite electrode with a thin PEO/LLTO solid polymer electrolyte layer on the top. In a high-magnification SEM image (Figure 6.5b), it is seen that the thickness of the solid composite electrolyte was  $15 \pm 5 \mu\text{m}$ . The relatively small thickness of PEO/LLTO solid electrolyte yields smaller impedance while the LLTO nanofibers could enhance the facial ion transport with high interfacial stability between electrode/electrolyte interfaces.<sup>141, 143</sup> The mechanical strength of the

as-prepared electrodes was revealed by the stress-strain curves obtained from tensile tests (Figure 6.5c). CNFs has a weak strength of 0.028 MPa with an average Young's module of 1.4 MPa and the strength increased to 0.107 MPa with almost the same Young's module after PEO was added into the CNFs. It is worth to mention that after incorporation of LLTO nanofibers, the average Young's module of CNF-PEO/LLTO increased to 2.0 MPa with the highest strength of 0.12 MPa and the composite electrode can be easily bended, which demonstrates the effective role of the ceramic LLTO nanofibers and PEO polymer in maintaining the structural integrity of the flexible electrode and this is quite beneficial for the long cycling performance of RT-ASSLSBs. Moreover, the corresponding EDS mapping of carbon (C), S, oxygen (O), titanium (Ti) and lanthanum (La) within the composite electrode (cross-sectional view) (Figure 6.5d) further proves the achievement of the proposed 3D architecture, i.e., a bilayer structure with thin LLTO-incorporated solid electrolyte layer on the top and PEO filled CNF/S layer at the bottom. The uniform distribution of elemental C, S and O in the bottom layer further reveals the co-existence and intimate contact of active S material, conductive CNF and solid electrolyte.

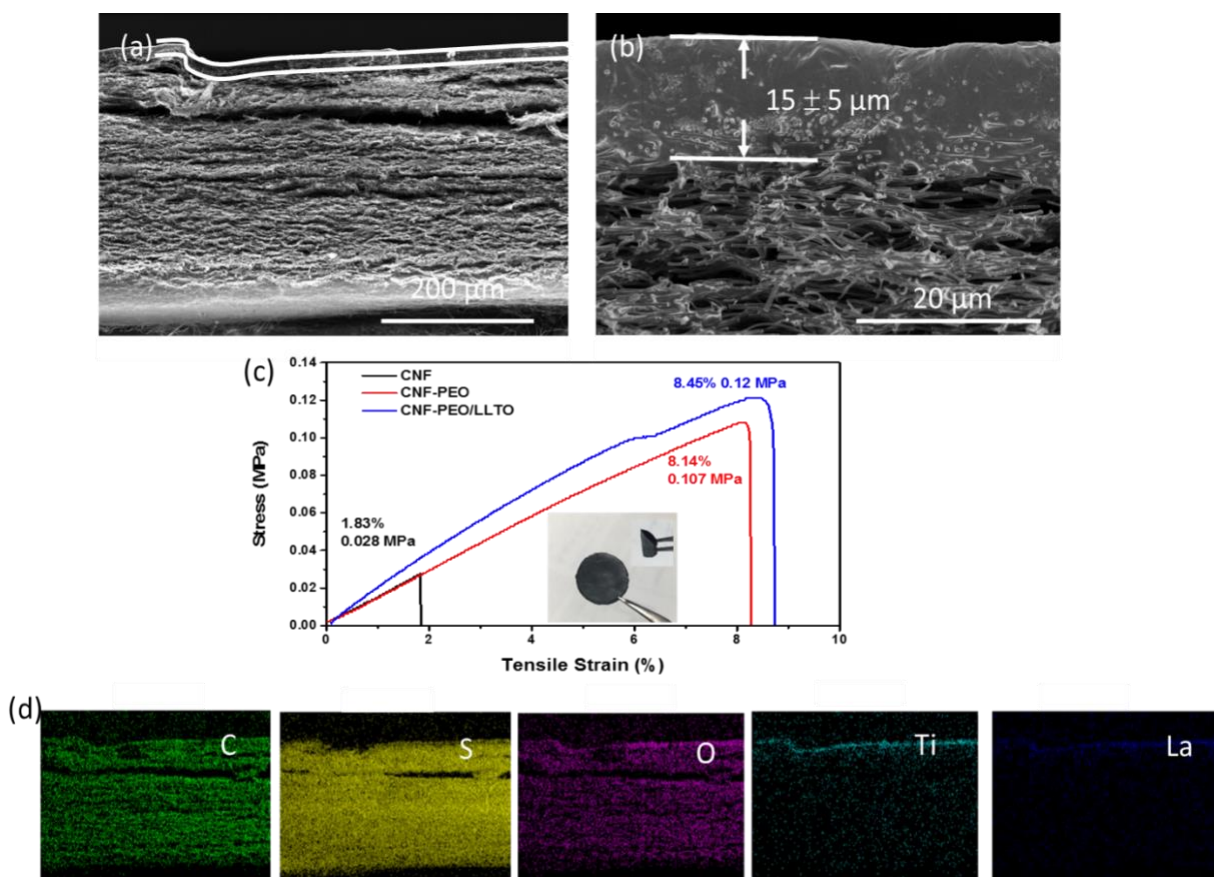


**Figure 6.5** Cross-sectional SEM images of (d) CNF/S-PEO/LLTO bilayer framework and (e) high magnification bilayer framework with clearly seen PEO/LLTO solid polymer electrolyte (thickness of  $15 \pm 5 \mu\text{m}$ ). (f) Stress-strain curves of CNF, CNF-PEO and CNF-PEO/LLTO (inserted: a photographic image of CNF/S-PEO/LLTO electrode with banded structure, showing good flexibility). (g) EDS mapping of the cross-section of CNF/S-PEO/LLTO bi-layer framework (e).

Figure 6.5a indicates the surface morphology of one individual CNF nanofiber with turbostratic structure and rough surface. After addition of S, the CNF surface was conformally coated by a thin S layer as showed in Figure 6.5b. Figure 6.5c indicates the morphology of CNF/S-PEO/LLTO. Typical features of LLTO ceramic structure with small grains arranged along the fiber axis could

be clearly observed.<sup>150</sup> The lattice spacing of the nano-crystallite LLTO, as shown in the HRTEM image (Figure 6.5d), is determined to be 0.27 nm, which could be ascribed to the (110) plane of LLTO and is identical with our previous study.<sup>150</sup>

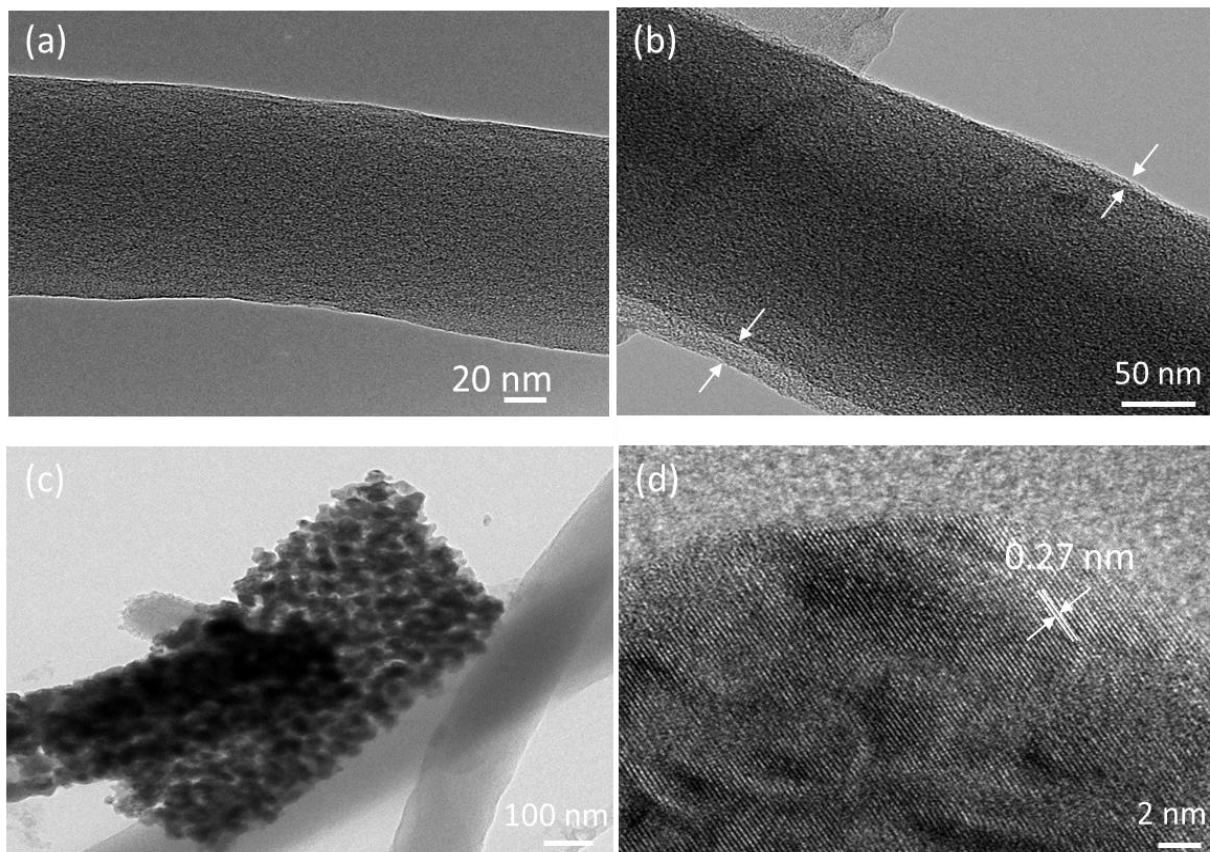


**Figure 6.6** (a) HRTEM image of single CNF, (b) CNF/S, (c) CNF/S-PEO/LLTO (LLTO nanofiber attached on PEO coated CNF/S) and (d) LLTO nanofibers with a lattice spacing of 0.27 nm.

Figure 6.7 show the scanning transmission electron microscopy (STEM) images of one representative CNF/S-PEO/LLTO structure. As expected, strong C, S, O, Ti and La signals were detected on CNF/S-PEO/LLTO. It is seen that the S was uniformly distributed along the fiber axis

with conformally coated PEO electrolyte as the C-containing region (232 nm) was larger than the S-containing region (205 nm), implying that S was distributed under the PEO electrolyte.

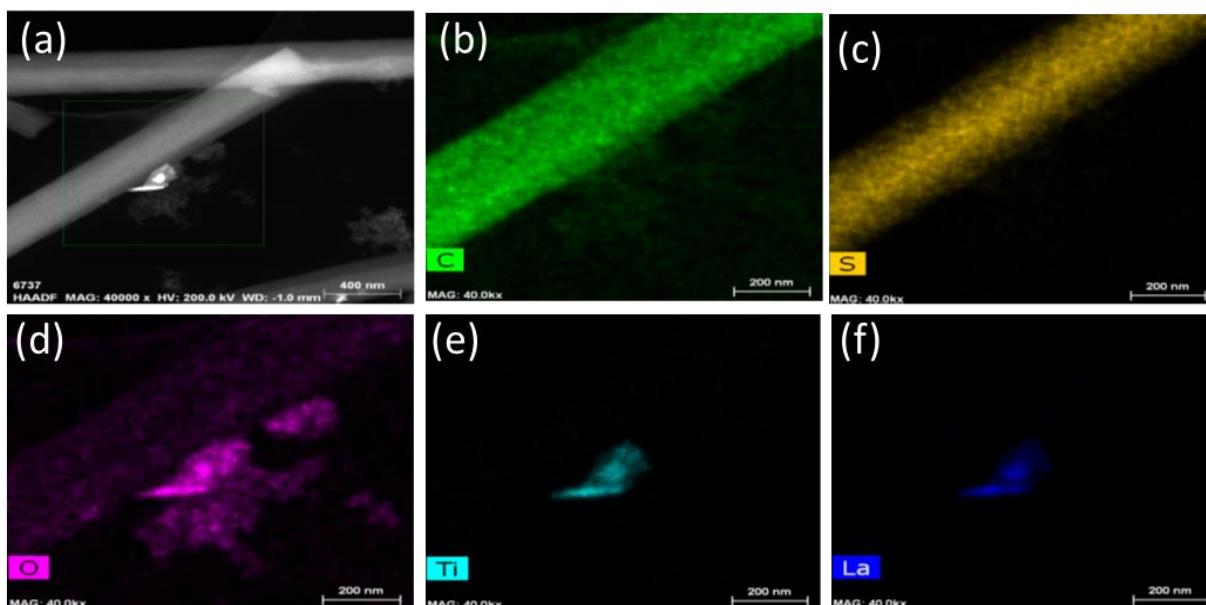


**Figure 6.7** (a) STEM images of one representative CNF/S-PEO/LLTO nanofiber and corresponding elemental mapping of (b) C, (c) S, (d) O, (e) Ti and (f) La.

Figure 6.8a shows the XRD patterns of CNF, CNF/S and CNF/S-PEO/LLTO. The XRD pattern of CNF mat exhibited one broad peak at  $24.5^\circ$ , corresponding to the (002) plane, which is the typical characteristic of graphite carbon materials.<sup>149</sup> After incorporation of S, some sharp and strong peaks appeared at within the diffraction range in CNF/S, indicating the existence of crystalline S (JCPDS card NO. 042-1278) on the CNF surface. The CNF/S-PEO/LLTO structure exhibited additional diffraction peaks corresponding to ceramic LLTO structure (JCPDS NO. 042-1278). Those findings are identical with the SEM and TEM results, indicating the co-existence of

C, S, O, Ti and La elements and successful formation of sufficient triple-phase contact between CNFs, S and PEO in the CNF/S-PEO/LLTO bilayer structure.

The working temperature of the solid polymer electrolytes (SPEs) largely depends on the melting temperature ( $T_m$ ) of SPEs as it reflects the transition point of crystalline to amorphous and the level of segmental mobility, which are crucial for the ion conduction.<sup>146</sup> In order to analyze the influence of adding LLTO nanofibers on the  $T_m$  of PEO polymer, differential scanning calorimetry (DSC) was carried out and the results are shown in Figure 6.8b. The  $T_m$  of pure PEO was high up to 69 °C with a large melting enthalpy, which implied that the segmental mobility of PEO polymer chains was restricted because of the high-level crystallinity at RT. When ceramic LLTO nanofibers were added, the  $T_m$  of PEOLLTO decreased to 35 °C with significantly decreased enthalpy, indicating the creation of more amorphous regions in PEO polymer matrix at RT.

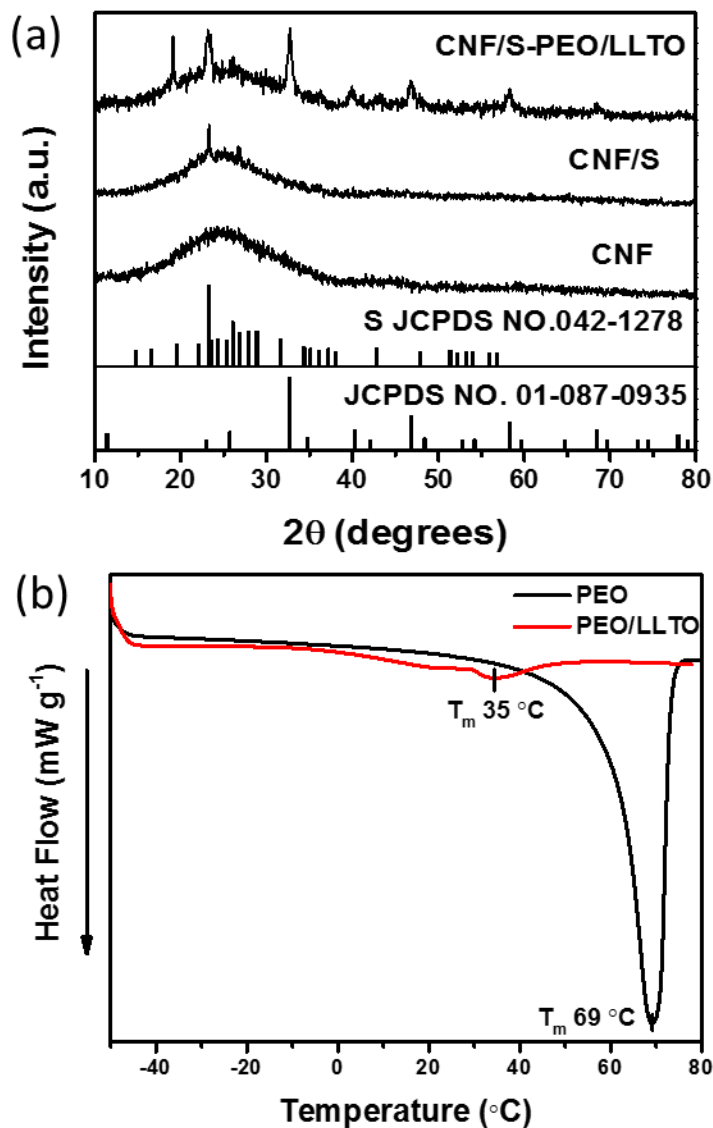


**Figure 6.8** (a) XRD patterns of CNFs, CNF/S and CNF/S-PEO/LLTO. (b) DSC curves of PEO and PEO/LLTO solid electrolytes.

The improved segmental mobility with high ion conduction in PEO/LLTO at RT was further revealed by electrochemical impedance analysis (EIS) test (Figure 6.7a), where the impedance value of PEO/LLTO electrolyte was decreased to 23 Ω (332 Ω for PEO electrolyte), corresponding

to a high ionic conductivity of  $2.3 \times 10^{-4} \text{ S cm}^{-1}$  ( $1.6 \times 10^{-5}$  for PEO) at RT. Figure 6.7b indicates the logarithmic ionic conductivity of PEO and PEO/LLTO solid electrolytes versus temperature. This result also demonstrated that the improved segmental motion in PEO/LLTO matrix lead to an increase in the Li ion migration, thus enabling the facial ion transport between the cathode and the anode. Figure 6.7c indicates the electrochemical stability window of PEOLLTO solid polymer electrolyte. The PEO/LLTO solid polymer electrolyte exhibits a high decomposition potential of around 4.5 V versus  $\text{Li}^+/\text{Li}$  and is suitable for application in ASSLSBs.

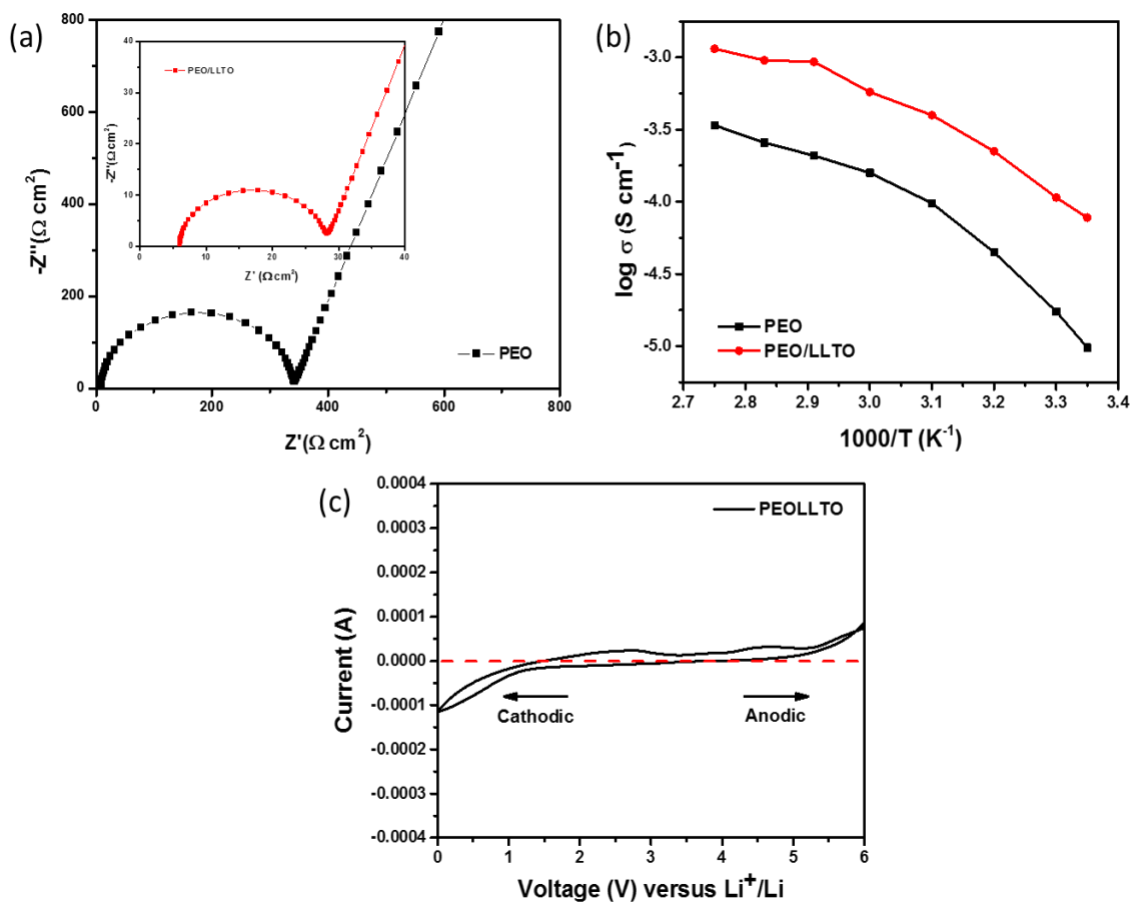


**Figure 6.9** (a) EIS results of PEO and PEO/LLTO solid polymer electrolytes tested at room temperature. (b) Arrhenius plots of PEO and PEO/LLTO solid electrolytes. (c) Electrochemical stability window of PEO/LLTO solid electrolyte.

### 6.3.2 Interfacial Stability of PEO/LLTO Solid Polymer Electrolyte/Li Metal

Since the instable electrolyte-electrode interface has been regarded as one of the main challenges that counter the realization of RT-ASSLSBs, the interfacial stability of PEO/LLTO solid polymer electrolyte was measured by applying a constant current to galvanostatically strip and plate Li in symmetric Li/electrolyte/Li cells. Figure 6.10a compares the voltage profiles of the symmetric

Li/PEO/Li and Li/(PEO/LLTO)/Li cells tested under a current density of  $0.5 \text{ mA cm}^{-2}$  with 0.5 h for each cycle at RT, where the positive/negative voltage indicates the Li stripping/plating, respectively. The cell exhibited a voltage of around 200 mV in initial cycles. After 8 h, a relatively stable voltage window of around 118 mV was maintained. The inserted figure on the left indicates the cycling of PEO and PEO/LLTO cells at 201-203 cycles. Large impedance with high polarization could be observed for symmetric Li/PEO/Li cell with a voltage window of  $\pm 415 \text{ mV}$ . In contrast, the Li/(PEO/LLTO)/Li cell demonstrated excellent stability over 1000 h with small impedance, indicating excellent electrochemical stability and high lithium plating/stripping efficiency across the electrolyte/lithium surface. The improved electrochemical stability and Li ion transfer efficiency across the electrode/electrolyte interface could be ascribed to the following advantages of the introduced CNF/S-PEO/LLTO bilayer framework: *i*) compared with pure PEO electrolyte, where the Li ions can only move with the loosed polymer chains, the addition of perovskite-type LLTO with abundant vacancies on the surface provide a second fast/continuous ionic conductive pathways for the Li ion hopping along the fiber axis;<sup>33, 150</sup> *ii*) based on the Lewis acid-base theory, LLTO is a typical Li-conductive ceramic that can restrict the delocalized anion, thus the Li ion mobility could be largely increased,<sup>33</sup> *iii*) the blocked anion transport can also reduce the double-layer electric field at electrolyte/lithium interface, thus the electrochemical decomposition of the polymer electrolyte is minimized.<sup>151-152</sup>

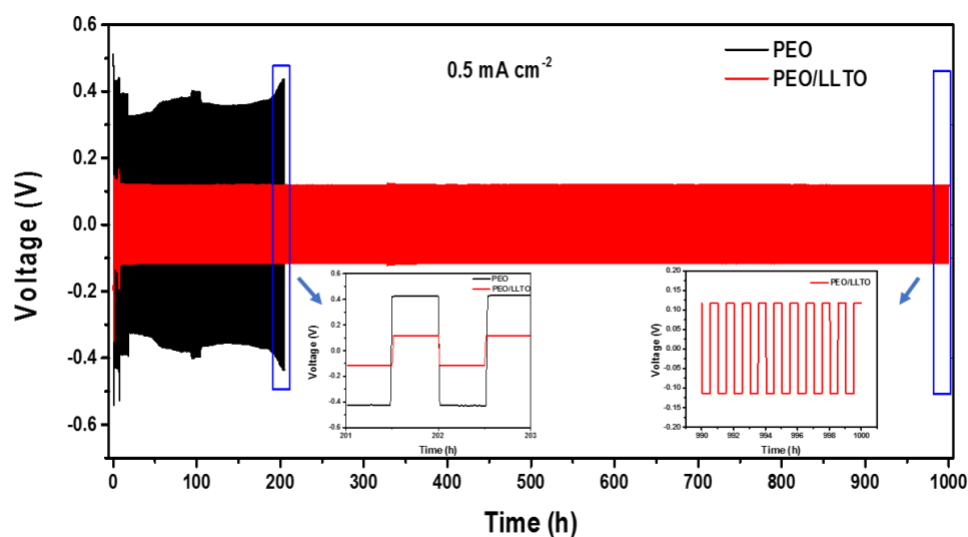


**Figure 6.10** Voltage profiles of Li plating/stripping cycling with a current density of  $0.5 \text{ mA cm}^{-2}$  at RT (inserted: voltage profiles of PEO and PEO/LLTO tested at 201-203 cycles - left; voltage profile of PEO/LLTO at 990-1000 cycles - right).

Furthermore, the stable long cycling performance of the Li/(PEO/LLTO)/Li also illustrates good Li dendrite suppression ability during continuous Li plating/stripping process as the cell would be short-circuited if the dendrite penetrated through the PEO/LLTO layer. The SEM image of Li metal after 1000 h cycling in Li/(PEO/LLTO)/Li cell does not show any obvious Li dendrite formation while the Li metal from Li/PEO/Li cell indicates obvious Li dendrites (Figure 6.11), which can be ascribed to the construction of homogeneous interfaces of PEO/LLTO guarantees a uniform Li ion flux at the electrolyte/lithium interfaces, which fundamentally suppresses the lithium dendrite nucleation.<sup>143, 152</sup> The high ionic conductivity, small interfacial resistance, good interfacial stability and excellent Li dendrite suppression of PEO/LLTO solid polymer electrolyte, along with the achieved dual-conductive cathode matrix, make the CNF/S-PEO/LLTO structure a promising candidate for the realization of RT-ASSLSBs.

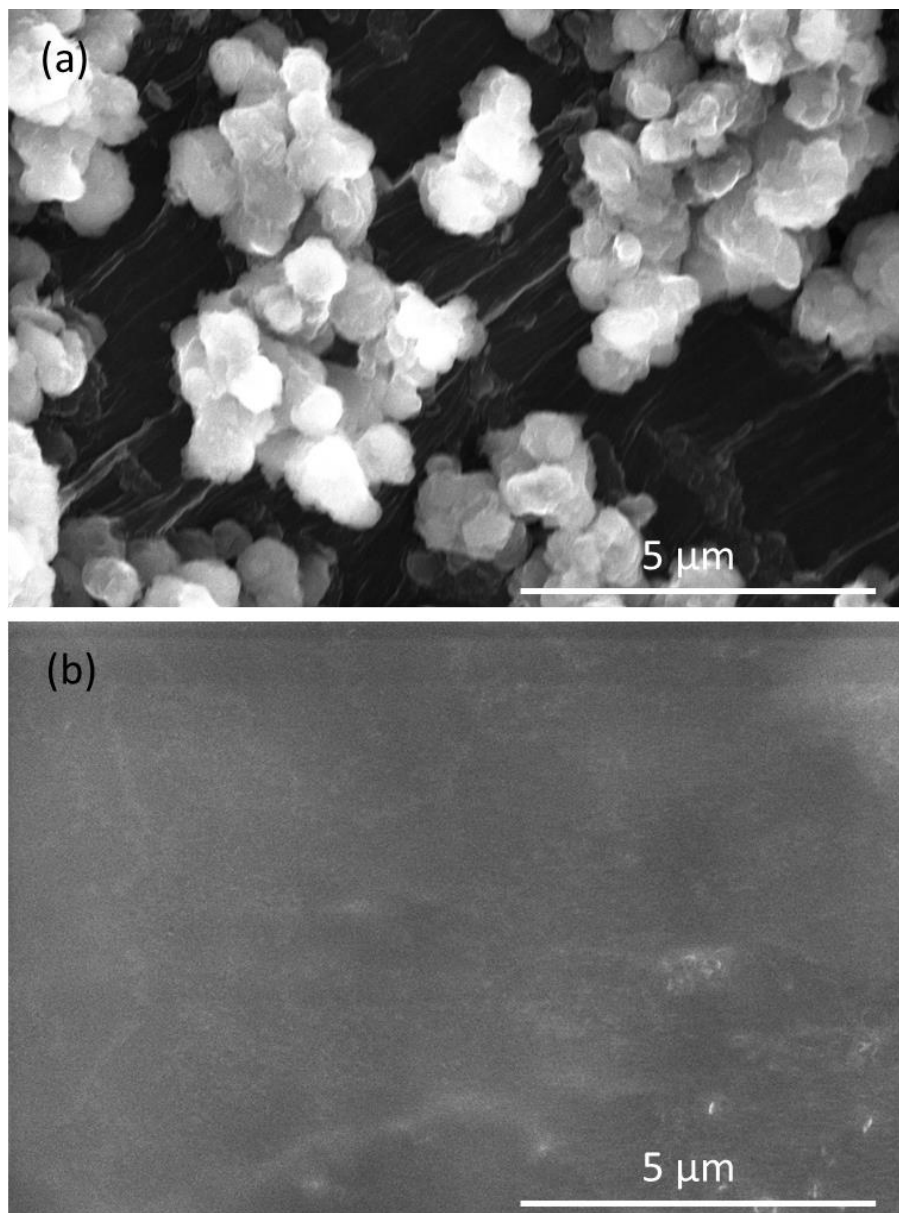


**Figure 6.11** SEM images of the surface of Li anodes from symmetric Li cells, (a) Li/PEO/Li and (b) Li/(PEO/LLTO)/Li, after 1000 h testing at a current density of  $0.5 \text{ mA cm}^{-2}$  at room temperature.

### 6.3.3 Electrochemical Performance of ASSLSBs with CNF/S-PEO/LLTO

The electrochemical performance of RT-ASSLSBs are measured by using CNF/S-PEO/LLTO as both cathode and solid electrolyte, while the commercial Li metal foil was directly used as the anode material. Figure 6.12a indicates the cycling performance of Li-S cells with CNF/S-PEO/LLTO measured at a current density of 0.05 C. The S loading in the cathode side of CNF/S-PEO/LLTO was  $1.27 \text{ mg cm}^{-2}$ , which is comparable with the recently reported loading amount in liquid electrolyte Li-S cells.<sup>24, 149</sup> No sudden capacity drop was observed in the initial few cycles, which was a symbolic phenomenon of the restricted polysulfide shuttle.<sup>141, 143</sup> Besides, the Li-S cell shows a stable cycling performance with a capacity retention of  $415 \text{ mAh g}^{-1}$  after 50 cycles. The good cycling stability could be ascribed to the formed dual-conductive matrix with fast transfer of electrons and ions. It is worth to mention that the Coulombic efficiency remained over 98% after 8 cycles and remained over 99% after 50 cycles. The high coulombic efficiency further confirms the blocking of polysulfide shuttle in Li-S cells with this novel bilayer cathode architecture.<sup>143, 148</sup> Figure 6.12b indicates the charge/discharge curves of the Li-S cell tested at different current densities in the first cycle. Typical shapes with S reduction and oxidation reaction could be seen, which is consistent with the reported literature.<sup>153-154</sup> Those electrochemical results reveal that the bilayer framework of CNF/S-PEO/LLTO electrode is able to charge/discharge at higher current densities up to 0.2 C at RT and reversible capacities of 384, 358 and  $262 \text{ mAh g}^{-1}$  could be achieved at current densities of 0.05 C, 0.1 C and 0.2 C, respectively, demonstrating favorable rate performance of CNF/S-PEO/LLTO electrode (Figure 6.12c). In addition, the relatively flat and long voltage plateaus of the solid cell at 0.05 C and 0.1 C implies the uncompromised polarization between the charge/discharge curves, which is a result of the increased number of reaction sites of S, as well as the benefits from the long-range conductive

CNF network with high surface area and the effective suppression of polysulfides by the PEO/LLTO layer.

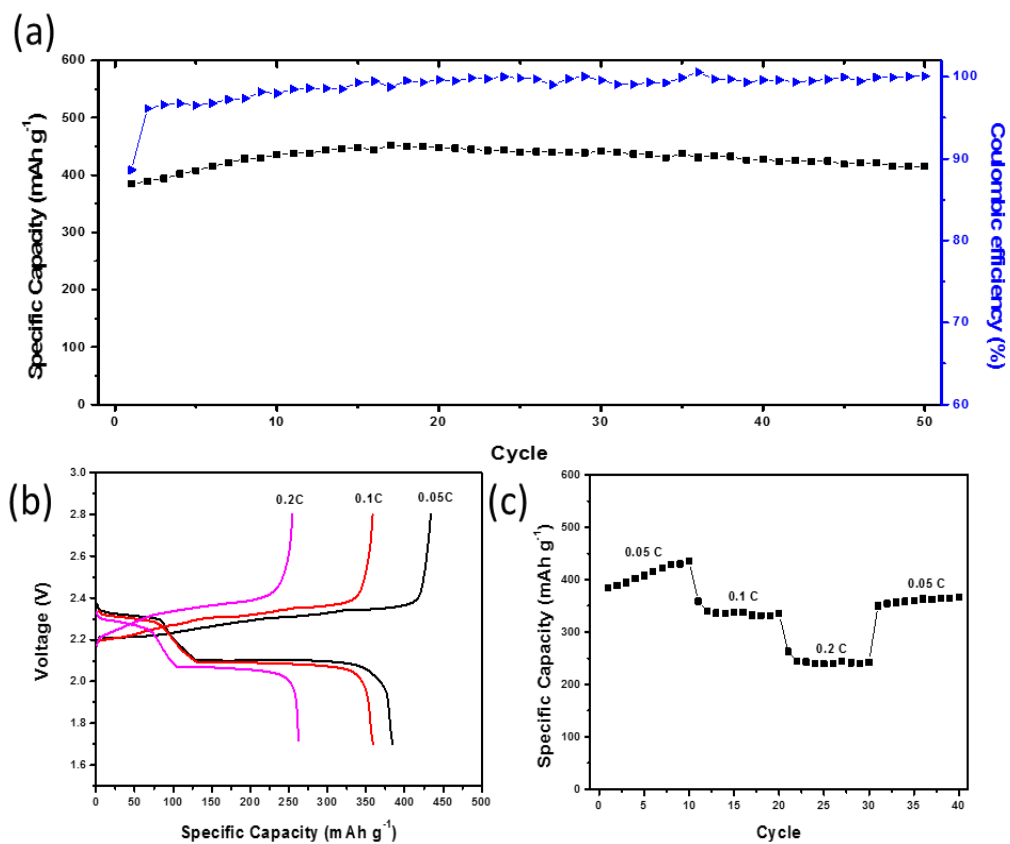


**Figure 6.12** (a) Cycling performance of ASSLSBs with CNF/S-PEO/LLTO electrode tested at 0.05 C with a sulfur loading of 1.27 mg cm<sup>-2</sup>. (b) Charge/discharge curves and (c) rate capabilities of cell with CNF/S-PEO/LLTO tested at various current densities.

As has been claimed before, this novel design of bi-layer cathode/electrolyte structure has dual-functionalities: *on one hand, for the bottom layer*, the intimate and sufficient triple-phase contact of conductive matrix, active material (S) and solid polymer electrolyte ensures a balanced electrical and ionic conductive matrix for the rapid transfer of electrons and ions, while the 3D

architecture of CNF/S-PEO/LLTO helps accommodate the large volume change during cycling and maintains the structure integrity; *on the other hand, for the top layer*, the uniform distribution of 1D LLTO nanofibers in the PEO electrolyte with high ionic conductivity at RT could not only facilitate the facial ion transport between the solid electrode/electrolyte interfaces but also help improve the interfacial stability and restrict the diffusion of polysulfides. In addition, the mechanically strong PEO/LLTO membrane with high strength also contributes to lithium dendrite inhabitation, thus the ASSLSBs with CNF/S-PEO/LLTO could be operated at RT with stable cycling performance and high Coulombic efficiency over 99%.

## 6.4 Conclusion

In summary, a novel 1D LLTO ceramic nanofiber incorporated PEO electrolyte enhanced 3D-flexible CNF/S composite was designed for RT-ASSLSBs. Benefiting from the novel bi-layer electrolyte/cathode architecture with the advantages of reduced interfacial resistance and enhanced interfacial stability between electrode/electrolyte interfaces, the formed fast-continuous long-range electron/ion transportation pathways within the 3D structure, as well as the excellent ability in polysulfide and lithium dendrite inhabitation, the ASSLSBs could be tested at RT without any liquid electrolyte addition and exhibited stable cycling performance with high Coulombic efficiency over 99% after 50 cycles. Overall, it is demonstrated that this novel structure design opens an alternative avenue for RT-ASSLSBs in dealing with the multiple challenges.

## CHAPTER 7            RECOMMENDED FUTURE WORK

The scope of this dissertation was advancement in the structural designs of separators and electrolytes for liquid and solid Li-S batteries to address the fundamental problems of shuttle effect and safety issues. With this purpose, we explored a series of materials and designed novel separator/electrolyte structures for both liquid and solid Li-S batteries, which are essential for the rapid development of Li-S batteries in the field of research and industrialization. Future studies should still focus on the development of all-solid-state Li-S batteries as they represent the future of Li-S cell industry in terms of fabrication benefits and potential safety. Nevertheless, the understanding on the cell architecture, cell performance and the interfaces (SSE/SSE, SSE/Li anode, and SSE/S cathode) are still in the early stage. Hence, multiplex efforts are still needed in the field of novel SSE/electrode methodologies to achieve desirable electrochemical performance of all-solid-state Li-S cells with state-of-the-art interfaces. The recommended future work can include but not limited to designing and selecting highly ionic conductive solid electrolytes, stabilizing solid-solid interfaces, as well as improving S cathode structure designs of all-solid-state batteries. Here, we propose three possible approaches as listed below.

For the SSEs, as another category of solid electrolytes, gel electrolyte processes high ionic conductivity at room temperature (almost the same order as liquid electrolyte) and it also has excellent contact with S cathode with stable electrolyte/electrode interface. However, the problem of gel electrolyte lies in its low mechanical strength that it cannot suppress the formation of lithium dendrites. Our study in Chapters 5 and 6 has demonstrated that the adding of 1D ceramic LLTO can effectively improve the mechanical strength of solid electrolytes, leading to good lithium

dendrite inhabitation. Hence, designing a unique gel polymer composite with ceramic LLTO fillers may help achieve good mechanical property and high ionic conductivity *simultaneously*, which will lead to better electrochemical performance with excellent lithium dendrite suppression capability.

In addition, to stabilize and improve the interfacial contact between the solid-solid electrolyte/electrode interfaces, some surface modification techniques, like atomic layer deposition (ALD), can be considered and applied to the Li anode part. It has been reported that apply a thin ALD aluminium oxide ( $\text{Al}_2\text{O}_3$ ) coating on the surface of fresh Li foil in liquid cells could enhance the wettability of Li surface towards liquid electrolytes, which contributes to the uniform and dense solid electrolyte interface (SEI) formation with excellent Li dendrite inhabitation.<sup>155</sup> In this view, combining the advantages of our mechanically strong 1D ceramic LLTO nanofibers incorporated solid composite electrolyte with ALD  $\text{Al}_2\text{O}_3$  protected Li metal, a more stabilized solid-solid interface with intimate electrolyte/electrode contact could be achieved.

Finally, for the S cathode structure design for all-solid-state batteries, even though the polysulfides could be mostly trapped by the solid electrolytes, the reutilization of those blocked polysulfides remains to be a big problem. Our previous study on separators in liquid electrolyte Li-S batteries proved that the existence of additional conductive layer could serve as the second current collector that the non-conductive polysulfides were reutilized and contributed to better electrochemical performance. Hence, it's promising for the all-solid-state Li-S batteries that if a thin conductive layer composed of conductive carbon materials, e.g. carbon nanotube (CNT), graphene and etc., and solid polymer electrolyte could be developed and applied on the surface of S cathode.

## REFERENCES

1. Manthiram, A.; Fu, Y.; Chung, S.-H.; Zu, C.; Su, Y.-S., Rechargeable lithium–sulfur batteries. *Chemical reviews* **2014**, *114* (23), 11751-11787.
2. Choi, N. S.; Chen, Z.; Freunberger, S. A.; Ji, X.; Sun, Y. K.; Amine, K.; Yushin, G.; Nazar, L. F.; Cho, J.; Bruce, P. G., Challenges facing lithium batteries and electrical double - layer capacitors. *Angewandte Chemie International Edition* **2012**, *51* (40), 9994-10024.
3. Lin, D.; Liu, Y.; Cui, Y., Reviving the lithium metal anode for high-energy batteries. *Nature nanotechnology* **2017**, *12* (3), 194.
4. Lu, L.; Han, X.; Li, J.; Hua, J.; Ouyang, M., A review on the key issues for lithium-ion battery management in electric vehicles. *Journal of power sources* **2013**, *226*, 272-288.
5. Bruce, P. G.; Freunberger, S. A.; Hardwick, L. J.; Tarascon, J.-M., Li–O<sub>2</sub> and Li–S batteries with high energy storage. *Nature materials* **2012**, *11* (1), 19.
6. Zhu, J.; Ge, Y.; Kim, D.; Lu, Y.; Chen, C.; Jiang, M.; Zhang, X., A novel separator coated by carbon for achieving exceptional high performance lithium-sulfur batteries. *Nano Energy* **2016**, *20*, 176-184.
7. Jayaprakash, N.; Shen, J.; Moganty, S. S.; Corona, A.; Archer, L. A., Porous hollow carbon@ sulfur composites for high - power lithium - sulfur batteries. *Angewandte Chemie* **2011**, *123* (26), 6026-6030.
8. Ji, X.; Lee, K. T.; Nazar, L. F., A highly ordered nanostructured carbon–sulphur cathode for lithium–sulphur batteries. *Nature materials* **2009**, *8* (6), 500.

9. Yang, Y.; Yu, G.; Cha, J. J.; Wu, H.; Vosgueritchian, M.; Yao, Y.; Bao, Z.; Cui, Y., Improving the performance of lithium–sulfur batteries by conductive polymer coating. *ACS nano* **2011**, *5* (11), 9187-9193.
10. Xiao, L.; Cao, Y.; Xiao, J.; Schwenzer, B.; Engelhard, M. H.; Saraf, L. V.; Nie, Z.; Exarhos, G. J.; Liu, J., A soft approach to encapsulate sulfur: polyaniline nanotubes for lithium - sulfur batteries with long cycle life. *Advanced materials* **2012**, *24* (9), 1176-1181.
11. Lin, Z.; Liang, C., Lithium–sulfur batteries: from liquid to solid cells. *Journal of Materials Chemistry A* **2015**, *3* (3), 936-958.
12. Zhang, Z.; Kong, L. L.; Liu, S.; Li, G. R.; Gao, X. P., A High - Efficiency Sulfur/Carbon Composite Based on 3D Graphene Nanosheet@ Carbon Nanotube Matrix as Cathode for Lithium - Sulfur Battery. *Advanced Energy Materials* **2017**, *7* (11).
13. Tao, X.; Liu, Y.; Liu, W.; Zhou, G.; Zhao, J.; Lin, D.; Zu, C.; Sheng, O.; Zhang, W.; Lee, H.-W., Solid-State Lithium–Sulfur Batteries Operated at 37° C with Composites of Nanostructured Li<sub>7</sub>La<sub>3</sub>Zr<sub>2</sub>O<sub>12</sub>/Carbon Foam and Polymer. *Nano letters* **2017**, *17* (5), 2967-2972.
14. Yao, H.; Yan, K.; Li, W.; Zheng, G.; Kong, D.; Seh, Z. W.; Narasimhan, V. K.; Liang, Z.; Cui, Y., Improved lithium–sulfur batteries with a conductive coating on the separator to prevent the accumulation of inactive S-related species at the cathode–separator interface. *Energy & Environmental Science* **2014**, *7* (10), 3381-3390.
15. Deng, N.; Kang, W.; Liu, Y.; Ju, J.; Wu, D.; Li, L.; Hassan, B. S.; Cheng, B., A review on separators for lithiumsulfur battery: Progress and prospects. *Journal of Power Sources* **2016**, *331*, 132-155.

16. Huang, J.-Q.; Zhang, Q.; Peng, H.-J.; Liu, X.-Y.; Qian, W.-Z.; Wei, F., Ionic shield for polysulfides towards highly-stable lithium–sulfur batteries. *Energy & environmental science* **2014**, *7* (1), 347-353.
17. Jiang, W.; Liu, Z.; Kong, Q.; Yao, J.; Zhang, C.; Han, P.; Cui, G., A high temperature operating nanofibrous polyimide separator in Li-ion battery. *Solid State Ionics* **2013**, *232*, 44-48.
18. Wang, L.; Liu, J.; Haller, S.; Wang, Y.; Xia, Y., A scalable hybrid separator for a high performance lithium–sulfur battery. *Chemical Communications* **2015**, *51* (32), 6996-6999.
19. Zhu, J.; Yanilmaz, M.; Fu, K.; Chen, C.; Lu, Y.; Ge, Y.; Kim, D.; Zhang, X., Understanding glass fiber membrane used as a novel separator for lithium–sulfur batteries. *Journal of Membrane Science* **2016**, *504*, 89-96.
20. Zhang, X.; Ji, L.; Toprakci, O.; Liang, Y.; Alcoutlabi, M., Electrospun nanofiber-based anodes, cathodes, and separators for advanced lithium-ion batteries. *Polymer Reviews* **2011**, *51* (3), 239-264.
21. Lee, H.; Alcoutlabi, M.; Watson, J. V.; Zhang, X., Electrospun nanofiber - coated separator membranes for lithium - ion rechargeable batteries. *Journal of Applied Polymer Science* **2013**, *129* (4), 1939-1951.
22. Jung, J.-W.; Lee, C.-L.; Yu, S.; Kim, I.-D., Electrospun nanofibers as a platform for advanced secondary batteries: a comprehensive review. *Journal of materials chemistry A* **2016**, *4* (3), 703-750.
23. Yanilmaz, M.; Lu, Y.; Dirican, M.; Fu, K.; Zhang, X., Nanoparticle-on-nanofiber hybrid membrane separators for lithium-ion batteries via combining electrospraying and electrospinning techniques. *Journal of Membrane Science* **2014**, *456*, 57-65.

24. Zhu, J.; Chen, C.; Lu, Y.; Zang, J.; Jiang, M.; Kim, D.; Zhang, X., Highly porous polyacrylonitrile/graphene oxide membrane separator exhibiting excellent anti-self-discharge feature for high-performance lithium–sulfur batteries. *Carbon* **2016**, *101*, 272-280.
25. Hao, X.; Zhu, J.; Jiang, X.; Wu, H.; Qiao, J.; Sun, W.; Wang, Z.; Sun, K., Ultrastrong polyoxazole nanofiber membranes for dendrite-proof and heat-resistant battery separators. *Nano letters* **2016**, *16* (5), 2981-2987.
26. Li, Z.; Zhang, J.; Lou, X. W. D., Hollow carbon nanofibers filled with MnO<sub>2</sub> nanosheets as efficient sulfur hosts for lithium–sulfur batteries. *Angewandte Chemie International Edition* **2015**, *54* (44), 12886-12890.
27. Han, F.; Yue, J.; Fan, X.; Gao, T.; Luo, C.; Ma, Z.; Suo, L.; Wang, C., High-performance all-solid-state lithium–sulfur battery enabled by a mixed-conductive Li<sub>2</sub>S nanocomposite. *Nano letters* **2016**, *16* (7), 4521-4527.
28. Kato, Y.; Hori, S.; Saito, T.; Suzuki, K.; Hirayama, M.; Mitsui, A.; Yonemura, M.; Iba, H.; Kanno, R., High-power all-solid-state batteries using sulfide superionic conductors. *Nature Energy* **2016**, *1* (4), 16030.
29. Hu, Y.-S., Batteries: getting solid. *Nature Energy* **2016**, *1* (4), 16042.
30. Manthiram, A.; Yu, X.; Wang, S., Lithium battery chemistries enabled by solid-state electrolytes. *Nature Reviews Materials* **2017**, *2* (4), 16103.
31. Judez, X.; Zhang, H.; Li, C.; Eshetu, G. G.; González-Marcos, J. A.; Armand, M.; Rodríguez-Martínez, L. M., Solid Electrolytes for Safe and High Energy Density Lithium-Sulfur Batteries: Promises and Challenges. *Journal of The Electrochemical Society* **2018**, *165* (1), A6008-A6016.

32. Fu, K. K.; Gong, Y.; Dai, J.; Gong, A.; Han, X.; Yao, Y.; Wang, C.; Wang, Y.; Chen, Y.; Yan, C., Flexible, solid-state, ion-conducting membrane with 3D garnet nanofiber networks for lithium batteries. *Proceedings of the National Academy of Sciences* **2016**, *113* (26), 7094-7099.
33. Liu, W.; Liu, N.; Sun, J.; Hsu, P.-C.; Li, Y.; Lee, H.-W.; Cui, Y., Ionic conductivity enhancement of polymer electrolytes with ceramic nanowire fillers. *Nano letters* **2015**, *15* (4), 2740-2745.
34. Li, Y.; Wong, K. W.; Dou, Q.; Zhang, W.; Wang, L.; Ng, K. M., A highly elastic and flexible solid-state polymer electrolyte based on ionic liquid-decorated PMMA nanoparticles for lithium batteries. *New Journal of Chemistry* **2017**, *41* (21), 13096-13103.
35. Zhang, M.; Li, M.; Chang, Z.; Wang, Y.; Gao, J.; Zhu, Y.; Wu, Y.; Huang, W., A sandwich PVDF/HEC/PVDF gel polymer electrolyte for lithium ion battery. *Electrochimica Acta* **2017**, *245*, 752-759.
36. Zhou, W.; Gao, H.; Goodenough, J. B., Low - cost hollow mesoporous polymer spheres and all - solid - state lithium, sodium batteries. *Advanced Energy Materials* **2016**, *6* (1).
37. Tan, R.; Gao, R.; Zhao, Y.; Zhang, M.; Xu, J.; Yang, J.; Pan, F., Novel organic–inorganic hybrid electrolyte to enable LiFePO<sub>4</sub> quasi-solid-state Li-ion batteries performed highly around room temperature. *ACS applied materials & interfaces* **2016**, *8* (45), 31273-31280.
38. Stephan, A. M., Review on gel polymer electrolytes for lithium batteries. *European polymer journal* **2006**, *42* (1), 21-42.
39. Peppas, N. A.; Keys, K. B.; Torres-Lugo, M.; Lowman, A. M., Poly (ethylene glycol)-containing hydrogels in drug delivery. *Journal of controlled release* **1999**, *62* (1-2), 81-87.

40. Ito, Y.; Kanehori, K.; Miyauchi, K.; Kudo, T., Ionic conductivity of electrolytes formed from PEO-LiCF<sub>3</sub>SO<sub>3</sub> complex low molecular weight poly (ethylene glycol). *Journal of materials science* **1987**, 22 (5), 1845-1849.
41. Egashira, M.; Todo, H.; Yoshimoto, N.; Morita, M., Lithium ion conduction in ionic liquid-based gel polymer electrolyte. *Journal of Power Sources* **2008**, 178 (2), 729-735.
42. Bouchet, R.; Maria, S.; Meziane, R.; Aboulaich, A.; Lienafa, L.; Bonnet, J.-P.; Phan, T. N.; Bertin, D.; Gimes, D.; Devaux, D., Single-ion BAB triblock copolymers as highly efficient electrolytes for lithium-metal batteries. *Nature materials* **2013**, 12 (5), 452.
43. Khurana, R.; Schaefer, J. L.; Archer, L. A.; Coates, G. W., Suppression of lithium dendrite growth using cross-linked polyethylene/poly (ethylene oxide) electrolytes: a new approach for practical lithium-metal polymer batteries. *Journal of the American Chemical Society* **2014**, 136 (20), 7395-7402.
44. Croce, F.; Appetecchi, G.; Persi, L.; Scrosati, B., Nanocomposite polymer electrolytes for lithium batteries. *Nature* **1998**, 394 (6692), 456.
45. Damen, L.; Hassoun, J.; Mastragostino, M.; Scrosati, B., Solid-state, rechargeable Li/LiFePO<sub>4</sub> polymer battery for electric vehicle application. *Journal of Power Sources* **2010**, 195 (19), 6902-6904.
46. Liu, S.; Imanishi, N.; Zhang, T.; Hirano, A.; Takeda, Y.; Yamamoto, O.; Yang, J., Effect of nano-silica filler in polymer electrolyte on Li dendrite formation in Li/poly (ethylene oxide)-Li (CF<sub>3</sub>SO<sub>2</sub>)<sub>2</sub>N/Li. *Journal of Power Sources* **2010**, 195 (19), 6847-6853.
47. Gurevitch, I.; Buonsanti, R.; Teran, A. A.; Gludovatz, B.; Ritchie, R. O.; Cabana, J.; Balsara, N. P., Nanocomposites of titanium dioxide and polystyrene-poly (ethylene oxide) block

- copolymer as solid-state electrolytes for lithium metal batteries. *Journal of The Electrochemical Society* **2013**, *160* (9), A1611-A1617.
48. Yu, X.; Bi, Z.; Zhao, F.; Manthiram, A., Polysulfide - Shuttle Control in Lithium - Sulfur Batteries with a Chemically/Electrochemically Compatible NaSICON - Type Solid Electrolyte. *Advanced Energy Materials* **2016**, *6* (24).
49. Das, S.; Ghosh, A., Ion conduction and relaxation in PEO-LiTFSI-Al<sub>2</sub>O<sub>3</sub> polymer nanocomposite electrolytes. *Journal of Applied Physics* **2015**, *117* (17), 174103.
50. Lin, D.; Liu, W.; Liu, Y.; Lee, H. R.; Hsu, P.-C.; Liu, K.; Cui, Y., High ionic conductivity of composite solid polymer electrolyte via in situ synthesis of monodispersed SiO<sub>2</sub> nanospheres in poly (ethylene oxide). *Nano letters* **2015**, *16* (1), 459-465.
51. Kobayashi, T.; Imade, Y.; Shishihara, D.; Homma, K.; Nagao, M.; Watanabe, R.; Yokoi, T.; Yamada, A.; Kanno, R.; Tatsumi, T., All solid-state battery with sulfur electrode and thio-LISICON electrolyte. *Journal of Power Sources* **2008**, *182* (2), 621-625.
52. Yamada, T.; Ito, S.; Omoda, R.; Watanabe, T.; Aihara, Y.; Agostini, M.; Ulissi, U.; Hassoun, J.; Scrosati, B., All Solid-State Lithium-Sulfur Battery Using a Glass-Type P<sub>2</sub>S<sub>5</sub>-Li<sub>2</sub>S Electrolyte: Benefits on Anode Kinetics. *Journal of The Electrochemical Society* **2015**, *162* (4), A646-A651.
53. Yao, X.; Huang, N.; Han, F.; Zhang, Q.; Wan, H.; Mwizerwa, J. P.; Wang, C.; Xu, X., High - Performance All - Solid - State Lithium - Sulfur Batteries Enabled by Amorphous Sulfur - Coated Reduced Graphene Oxide Cathodes. *Advanced Energy Materials* **2017**, *7* (17).
54. Nagao, M.; Imade, Y.; Narisawa, H.; Watanabe, R.; Yokoi, T.; Tatsumi, T.; Kanno, R., Reaction mechanism of all-solid-state lithium-sulfur battery with two-dimensional mesoporous carbon electrodes. *Journal of Power Sources* **2013**, *243*, 60-64.

55. Bruce, P. G.; Hardwick, L. J.; Abraham, K., Lithium-air and lithium-sulfur batteries. *MRS bulletin* **2011**, *36* (7), 506-512.
56. Yin, Y. X.; Xin, S.; Guo, Y. G.; Wan, L. J., Lithium–sulfur batteries: electrochemistry, materials, and prospects. *Angewandte Chemie International Edition* **2013**, *52* (50), 13186-13200.
57. Zhang, S. S., Liquid electrolyte lithium/sulfur battery: fundamental chemistry, problems, and solutions. *Journal of Power Sources* **2013**, *231*, 153-162.
58. Pang, Q.; Nazar, L. F., Long-life and high-areal-capacity Li–S batteries enabled by a light-weight polar host with intrinsic polysulfide adsorption. *ACS nano* **2016**, *10* (4), 4111-4118.
59. Fotouhi, A.; Auger, D. J.; Propp, K.; Longo, S.; Wild, M., A review on electric vehicle battery modelling: From Lithium-ion toward Lithium–Sulphur. *Renewable and Sustainable Energy Reviews* **2016**, *56*, 1008-1021.
60. Peng, H. J.; Xu, W. T.; Zhu, L.; Wang, D. W.; Huang, J. Q.; Cheng, X. B.; Yuan, Z.; Wei, F.; Zhang, Q., 3D Carbonaceous Current Collectors: The Origin of Enhanced Cycling Stability for High - Sulfur - Loading Lithium - Sulfur Batteries. *Advanced Functional Materials* **2016**, *26* (35), 6351-6358.
61. Wang, H.; Zhang, W.; Liu, H.; Guo, Z., A Strategy for Configuration of an Integrated Flexible Sulfur Cathode for High - Performance Lithium - Sulfur Batteries. *Angewandte Chemie International Edition* **2016**, *55* (12), 3992-3996.
62. Li, Z.; Zhang, J.; Guan, B.; Wang, D.; Liu, L.-M.; Lou, X. W. D., A sulfur host based on titanium monoxide@ carbon hollow spheres for advanced lithium–sulfur batteries. *Nature communications* **2016**, *7*, 13065.

63. Fang, R.; Zhao, S.; Hou, P.; Cheng, M.; Wang, S.; Cheng, H. M.; Liu, C.; Li, F., 3D interconnected electrode materials with ultrahigh areal sulfur loading for Li-S batteries. *Advanced materials* **2016**, *28* (17), 3374-3382.
64. Hu, G.; Xu, C.; Sun, Z.; Wang, S.; Cheng, H. M.; Li, F.; Ren, W., 3D Graphene - Foam - Reduced - Graphene - Oxide Hybrid Nested Hierarchical Networks for High - Performance Li - S Batteries. *Advanced materials* **2016**, *28* (8), 1603-1609.
65. Li, L.; Zhou, G.; Yin, L.; Koratkar, N.; Li, F.; Cheng, H.-M., Stabilizing sulfur cathodes using nitrogen-doped graphene as a chemical immobilizer for Li S batteries. *Carbon* **2016**, *108*, 120-126.
66. Lee, H.; Yanilmaz, M.; Toprakci, O.; Fu, K.; Zhang, X., A review of recent developments in membrane separators for rechargeable lithium-ion batteries. *Energy & Environmental Science* **2014**, *7* (12), 3857-3886.
67. Zhou, G.; Li, L.; Wang, D. W.; Shan, X. y.; Pei, S.; Li, F.; Cheng, H. M., A flexible sulfur - graphene - polypropylene separator integrated electrode for advanced Li - S batteries. *Advanced Materials* **2015**, *27* (4), 641-647.
68. Chung, S.-H.; Manthiram, A., High-performance Li-S batteries with an ultra-lightweight MWCNT-coated separator. *The journal of physical chemistry letters* **2014**, *5* (11), 1978-1983.
69. Huang, J.-Q.; Zhuang, T.-Z.; Zhang, Q.; Peng, H.-J.; Chen, C.-M.; Wei, F., Permselective graphene oxide membrane for highly stable and anti-self-discharge lithium-sulfur batteries. *Acs Nano* **2015**, *9* (3), 3002-3011.
70. Zhang, Y.; Miao, L.; Ning, J.; Xiao, Z.; Hao, L.; Wang, B.; Zhi, L., A graphene-oxide-based thin coating on the separator: an efficient barrier towards high-stable lithium-sulfur batteries. *2D Materials* **2015**, *2* (2), 024013.

71. Huang, J.-Q.; Xu, Z.-L.; Abouali, S.; Garakani, M. A.; Kim, J.-K., Porous graphene oxide/carbon nanotube hybrid films as interlayer for lithium-sulfur batteries. *Carbon* **2016**, *99*, 624-632.
72. Shaibani, M.; Akbari, A.; Sheath, P.; Easton, C. D.; Banerjee, P. C.; Konstas, K.; Fakhfour, A.; Barghamadi, M.; Musameh, M. M.; Best, A. S., Suppressed polysulfide crossover in Li-S batteries through a high-flux graphene oxide membrane supported on a sulfur cathode. *ACS nano* **2016**, *10* (8), 7768-7779.
73. Zhou, G.; Pei, S.; Li, L.; Wang, D. W.; Wang, S.; Huang, K.; Yin, L. C.; Li, F.; Cheng, H. M., A graphene - pure - sulfur sandwich structure for ultrafast, long - life lithium - sulfur batteries. *Advanced materials* **2014**, *26* (4), 625-631.
74. Xu, C.; Shi, X.; Ji, A.; Shi, L.; Zhou, C.; Cui, Y., Fabrication and characteristics of reduced graphene oxide produced with different green reductants. *PLoS One* **2015**, *10* (12), e0144842.
75. Wang, Z.; Dong, Y.; Li, H.; Zhao, Z.; Wu, H. B.; Hao, C.; Liu, S.; Qiu, J.; Lou, X. W. D., Enhancing lithium-sulphur battery performance by strongly binding the discharge products on amino-functionalized reduced graphene oxide. *Nature communications* **2014**, *5*, 5002.
76. Wang, H.; Yang, Y.; Liang, Y.; Robinson, J. T.; Li, Y.; Jackson, A.; Cui, Y.; Dai, H., Graphene-wrapped sulfur particles as a rechargeable lithium-sulfur battery cathode material with high capacity and cycling stability. *Nano letters* **2011**, *11* (7), 2644-2647.
77. Wang, X.; Wang, Z.; Chen, L., Reduced graphene oxide film as a shuttle-inhibiting interlayer in a lithium-sulfur battery. *Journal of Power Sources* **2013**, *242*, 65-69.
78. Pan, Q.; Tong, N.; He, N.; Liu, Y.; Shim, E.; Pourdeyhimi, B.; Gao, W., Electrospun Mat of Poly (vinyl alcohol)/Graphene Oxide for Superior Electrolyte Performance. *ACS applied materials & interfaces* **2018**.

79. Gao, W.; Alemany, L. B.; Ci, L.; Ajayan, P. M., New insights into the structure and reduction of graphite oxide. *Nature chemistry* **2009**, *1* (5), 403-408.
80. Shin, H. J.; Kim, K. K.; Benayad, A.; Yoon, S. M.; Park, H. K.; Jung, I. S.; Jin, M. H.; Jeong, H. K.; Kim, J. M.; Choi, J. Y., Efficient reduction of graphite oxide by sodium borohydride and its effect on electrical conductance. *Advanced Functional Materials* **2009**, *19* (12), 1987-1992.
81. Wang, Y.-X.; Chou, S.-L.; Liu, H.-K.; Dou, S.-X., Reduced graphene oxide with superior cycling stability and rate capability for sodium storage. *Carbon* **2013**, *57*, 202-208.
82. Kim, S.; Park, G.; Sennu, P.; Lee, S.; Choi, K.; Oh, J.; Lee, Y.-S.; Park, S., Effect of degree of reduction on the anode performance of reduced graphene oxide in Li-ion batteries. *RSC Advances* **2015**, *5* (105), 86237-86241.
83. Zhou, X.; Xie, J.; Yang, J.; Zou, Y.; Tang, J.; Wang, S.; Ma, L.; Liao, Q., Improving the performance of lithium–sulfur batteries by graphene coating. *Journal of Power Sources* **2013**, *243*, 993-1000.
84. Wang, D.-W.; Zhou, G.; Li, F.; Wu, K.-H.; Lu, G. Q. M.; Cheng, H.-M.; Gentle, I. R., A microporous–mesoporous carbon with graphitic structure for a high-rate stable sulfur cathode in carbonate solvent-based Li–S batteries. *Physical Chemistry Chemical Physics* **2012**, *14* (24), 8703-8710.
85. Luo, L.; Chung, S.-H.; Chang, C.-H.; Manthiram, A., A nickel-foam@ carbon-shell with a pie-like architecture as an efficient polysulfide trap for high-energy Li–S batteries. *Journal of Materials Chemistry A* **2017**, *5* (29), 15002-15007.
86. Zhang, S. S., Role of LiNO<sub>3</sub> in rechargeable lithium/sulfur battery. *Electrochimica Acta* **2012**, *70*, 344-348.

87. Suk, J. W.; Piner, R. D.; An, J.; Ruoff, R. S., Mechanical properties of monolayer graphene oxide. *ACS nano* **2010**, *4* (11), 6557-6564.
88. Zhao, C.; Gao, H.; Chen, C.; Wu, H., Reduction of graphene oxide in Li-ion batteries. *Journal of Materials Chemistry A* **2015**, *3* (36), 18360-18364.
89. Fei, H.; An, Y.; Feng, J.; Ci, L.; Xiong, S., Enhancing the safety and electrochemical performance of ether based lithium sulfur batteries by introducing an efficient flame retarding additive. *RSC Advances* **2016**, *6* (58), 53560-53565.
90. Evers, S.; Nazar, L. F., New approaches for high energy density lithium–sulfur battery cathodes. *Accounts of chemical research* **2012**, *46* (5), 1135-1143.
91. Zhang, B.; Qin, X.; Li, G.; Gao, X., Enhancement of long stability of sulfur cathode by encapsulating sulfur into micropores of carbon spheres. *Energy & Environmental Science* **2010**, *3* (10), 1531-1537.
92. Xu, G.; Ding, B.; Nie, P.; Shen, L.; Dou, H.; Zhang, X., Hierarchically porous carbon encapsulating sulfur as a superior cathode material for high performance lithium–sulfur batteries. *ACS applied materials & interfaces* **2013**, *6* (1), 194-199.
93. Wang, C.; Wang, X.; Wang, Y.; Chen, J.; Zhou, H.; Huang, Y., Macroporous free-standing nano-sulfur/reduced graphene oxide paper as stable cathode for lithium-sulfur battery. *Nano Energy* **2015**, *11*, 678-686.
94. Ji, L.; Rao, M.; Zheng, H.; Zhang, L.; Li, Y.; Duan, W.; Guo, J.; Cairns, E. J.; Zhang, Y., Graphene oxide as a sulfur immobilizer in high performance lithium/sulfur cells. *Journal of the American Chemical Society* **2011**, *133* (46), 18522-18525.
95. Cao, J.; Chen, C.; Zhao, Q.; Zhang, N.; Lu, Q.; Wang, X.; Niu, Z.; Chen, J., A Flexible Nanostructured Paper of a Reduced Graphene Oxide – Sulfur Composite for High -

- Performance Lithium – Sulfur Batteries with Unconventional Configurations. *Advanced Materials* **2016**, 28 (43), 9629-9636.
96. Zheng, G.; Yang, Y.; Cha, J. J.; Hong, S. S.; Cui, Y., Hollow carbon nanofiber-encapsulated sulfur cathodes for high specific capacity rechargeable lithium batteries. *Nano letters* **2011**, 11 (10), 4462-4467.
97. Su, Y.-S.; Manthiram, A., Lithium–sulphur batteries with a microporous carbon paper as a bifunctional interlayer. *Nature communications* **2012**, 3, 1166.
98. Manthiram, A.; Fu, Y.; Su, Y.-S., Challenges and prospects of lithium–sulfur batteries. *Accounts of chemical research* **2012**, 46 (5), 1125-1134.
99. Barré, A.; Deguilhem, B.; Grolleau, S.; Gérard, M.; Suard, F.; Riu, D., A review on lithium-ion battery ageing mechanisms and estimations for automotive applications. *Journal of Power Sources* **2013**, 241, 680-689.
100. Li, X.; Lushington, A.; Sun, Q.; Xiao, W.; Liu, J.; Wang, B.; Ye, Y.; Nie, K.; Hu, Y.; Xiao, Q., Safe and durable high-temperature lithium–sulfur batteries via molecular layer deposited coating. *Nano letters* **2016**, 16 (6), 3545-3549.
101. Zhu, J.; Yildirim, E.; Aly, K.; Shen, J.; Chen, C.; Lu, Y.; Jiang, M.; Kim, D.; Tonelli, A. E.; Pasquinelli, M. A., Hierarchical multi-component nanofiber separators for lithium polysulfide capture in lithium–sulfur batteries: an experimental and molecular modeling study. *Journal of Materials Chemistry A* **2016**, 4 (35), 13572-13581.
102. Cho, T.-H.; Tanaka, M.; Onishi, H.; Kondo, Y.; Nakamura, T.; Yamazaki, H.; Tanase, S.; Sakai, T., Battery performances and thermal stability of polyacrylonitrile nano-fiber-based nonwoven separators for Li-ion battery. *Journal of Power Sources* **2008**, 181 (1), 155-160.

103. Mi, K.; Chen, S.; Xi, B.; Kai, S.; Jiang, Y.; Feng, J.; Qian, Y.; Xiong, S., Sole Chemical Confinement of Polysulfides on Nonporous Nitrogen/Oxygen Dual - Doped Carbon at the Kilogram Scale for Lithium - Sulfur Batteries. *Advanced Functional Materials* **2017**, *27* (1).
104. Abbas, M.; Zou, Q.; Li, S.; Yan, X., Self - Assembled Peptide - and Protein - Based Nanomaterials for Antitumor Photodynamic and Photothermal Therapy. *Advanced materials* **2017**, *29* (12).
105. Xu, G.; Yan, Q.-b.; Kushima, A.; Zhang, X.; Pan, J.; Li, J., Conductive graphene oxide-polyacrylic acid (GOPAA) binder for lithium-sulfur battery. *Nano Energy* **2017**, *31*, 568-574.
106. Singhal, R.; Chung, S.-H.; Manthiram, A.; Kalra, V., A free-standing carbon nanofiber interlayer for high-performance lithium-sulfur batteries. *Journal of Materials Chemistry A* **2015**, *3* (8), 4530-4538.
107. Xiao, Z.; Yang, Z.; Wang, L.; Nie, H.; Zhong, M. e.; Lai, Q.; Xu, X.; Zhang, L.; Huang, S., A lightweight TiO<sub>2</sub>/graphene interlayer, applied as a highly effective polysulfide absorbent for fast, long - life lithium - sulfur batteries. *Advanced materials* **2015**, *27* (18), 2891-2898.
108. Angulakshmi, N.; Stephan, A. M., Electrospun trilayer polymeric membranes as separator for lithium-ion batteries. *Electrochimica Acta* **2014**, *127*, 167-172.
109. Choi, S.-S.; Lee, Y. S.; Joo, C. W.; Lee, S. G.; Park, J. K.; Han, K.-S., Electrospun PVDF nanofiber web as polymer electrolyte or separator. *Electrochimica Acta* **2004**, *50* (2-3), 339-343.
110. Zhu, Y.; Wang, F.; Liu, L.; Xiao, S.; Chang, Z.; Wu, Y., Composite of a nonwoven fabric with poly (vinylidene fluoride) as a gel membrane of high safety for lithium ion battery. *Energy & Environmental Science* **2013**, *6* (2), 618-624.

111. Pan, Q.; Chung, C.-C.; He, N.; Jones, J. L.; Gao, W., Accelerated thermal decomposition of graphene oxide films in air via in situ X-ray diffraction analysis. *The Journal of Physical Chemistry C* **2016**, *120* (27), 14984-14990.
112. Xue, J.; Wu, L.; Hu, N.; Qiu, J.; Chang, C.; Atobe, S.; Fukunaga, H.; Watanabe, T.; Liu, Y.; Ning, H., Evaluation of piezoelectric property of reduced graphene oxide (rGO)–poly (vinylidene fluoride) nanocomposites. *Nanoscale* **2012**, *4* (22), 7250-7255.
113. Zhang, H.; Zhang, P.; Li, Z.; Sun, M.; Wu, Y.; Wu, H., A novel sandwiched membrane as polymer electrolyte for lithium ion battery. *Electrochemistry communications* **2007**, *9* (7), 1700-1703.
114. Madaeni, S.; Zinadini, S.; Vatanpour, V., A new approach to improve antifouling property of PVDF membrane using in situ polymerization of PAA functionalized TiO<sub>2</sub> nanoparticles. *Journal of membrane science* **2011**, *380* (1-2), 155-162.
115. Yang, G.; Zhang, G.; Sheng, P.; Sun, F.; Xu, W.; Zhang, D., A new approach to reduced graphite oxide with tetrathiafulvalene in the presence of metal ions. *Journal of Materials Chemistry* **2012**, *22* (10), 4391-4395.
116. Zong, M.; Huang, Y.; Zhao, Y.; Sun, X.; Qu, C.; Luo, D.; Zheng, J., Facile preparation, high microwave absorption and microwave absorbing mechanism of RGO–Fe<sub>3</sub>O<sub>4</sub> composites. *RSC Advances* **2013**, *3* (45), 23638-23648.
117. Tao, X.; Wang, J.; Liu, C.; Wang, H.; Yao, H.; Zheng, G.; Seh, Z. W.; Cai, Q.; Li, W.; Zhou, G., Balancing surface adsorption and diffusion of lithium-polysulfides on nonconductive oxides for lithium–sulfur battery design. *Nature communications* **2016**, *7*, 11203.

118. Xu, N.; Qian, T.; Liu, X.; Liu, J.; Chen, Y.; Yan, C., Greatly suppressed shuttle effect for improved lithium sulfur battery performance through short chain intermediates. *Nano letters* **2016**, *17* (1), 538-543.
119. Seh, Z. W.; Zhang, Q.; Li, W.; Zheng, G.; Yao, H.; Cui, Y., Stable cycling of lithium sulfide cathodes through strong affinity with a bifunctional binder. *Chemical Science* **2013**, *4* (9), 3673-3677.
120. Jiang, M.; Zhu, J.; Chen, C.; Lu, Y.; Ge, Y.; Zhang, X., Poly (vinyl Alcohol) Borate Gel Polymer Electrolytes Prepared by Electrodeposition and Their Application in Electrochemical Supercapacitors. *ACS applied materials & interfaces* **2016**, *8* (5), 3473-3481.
121. Yim, T.; Han, S. H.; Park, N. H.; Park, M. S.; Lee, J. H.; Shin, J.; Choi, J. W.; Jung, Y.; Jo, Y. N.; Yu, J. S., Effective Polysulfide Rejection by Dipole - Aligned BaTiO<sub>3</sub> Coated Separator in Lithium - Sulfur Batteries. *Advanced Functional Materials* **2016**, *26* (43), 7817-7823.
122. Dunn, B.; Kamath, H.; Tarascon, J.-M., Electrical energy storage for the grid: a battery of choices. *Science* **2011**, *334* (6058), 928-935.
123. Goodenough, J. B.; Park, K.-S., The Li-ion rechargeable battery: a perspective. *Journal of the American Chemical Society* **2013**, *135* (4), 1167-1176.
124. Luo, W.; Gong, Y.; Zhu, Y.; Li, Y.; Yao, Y.; Zhang, Y.; Fu, K. K.; Pastel, G.; Lin, C. F.; Mo, Y., Reducing Interfacial Resistance between Garnet - Structured Solid - State Electrolyte and Li - Metal Anode by a Germanium Layer. *Advanced Materials* **2017**, *29* (22).
125. Sun, J.; Lv, C.; Lv, F.; Chen, S.; Li, D.; Guo, Z.; Han, W.; Yang, D.; Guo, S., Tuning the shell number of multishelled metal oxide hollow fibers for optimized lithium-ion storage. *ACS nano* **2017**, *11* (6), 6186-6193.

126. Xu, K., Electrolytes and interphases in Li-ion batteries and beyond. *Chemical reviews* **2014**, *114* (23), 11503-11618.
127. Yang, C.; Fu, K.; Zhang, Y.; Hitz, E.; Hu, L., Protected Lithium - Metal Anodes in Batteries: From Liquid to Solid. *Advanced Materials* **2017**.
128. Sun, C.; Liu, J.; Gong, Y.; Wilkinson, D. P.; Zhang, J., Recent advances in all-solid-state rechargeable lithium batteries. *Nano Energy* **2017**, *33*, 363-386.
129. Sharma, A., Structural, electrical properties and dielectric relaxations in Na<sup>+</sup> ion conducting solid polymer electrolyte. *Journal of Physics: Condensed Matter* **2018**.
130. Wang, C.; Zhang, X.-W.; Appleby, A. J., Solvent-free composite PEO-ceramic fiber/mat electrolytes for lithium secondary cells. *Journal of The Electrochemical Society* **2005**, *152* (1), A205-A209.
131. Choi, J.-H.; Lee, C.-H.; Yu, J.-H.; Doh, C.-H.; Lee, S.-M., Enhancement of ionic conductivity of composite membranes for all-solid-state lithium rechargeable batteries incorporating tetragonal Li<sub>7</sub>La<sub>3</sub>Zr<sub>2</sub>O<sub>12</sub> into a polyethylene oxide matrix. *Journal of Power Sources* **2015**, *274*, 458-463.
132. Maitra, P.; Ding, J.; Liu, B.; Wunder, S.; Lin, H.-P.; Chua, D.; Salomon, M., Solid State Electrolytes Prepared from PEO (360) Silanated Silica. **2002**.
133. Armand, M., Polymer solid electrolytes-an overview. *Solid State Ionics* **1983**, *9*, 745-754.
134. Wright, P. V., Electrical conductivity in ionic complexes of poly (ethylene oxide). *Polymer International* **1975**, *7* (5), 319-327.
135. Chopade, S. A.; Au, J. G.; Li, Z.; Schmidt, P. W.; Hillmyer, M. A.; Lodge, T. P., Robust Polymer Electrolyte Membranes with High Ambient-Temperature Lithium-Ion Conductivity

- via Polymerization-Induced Microphase Separation. *ACS applied materials & interfaces* **2017**, 9 (17), 14561-14565.
136. Pan, Q.; Barbash, D.; Smith, D. M.; Qi, H.; Gleeson, S. E.; Li, C. Y., Correlating Electrode– Electrolyte Interface and Battery Performance in Hybrid Solid Polymer Electrolyte - Based Lithium Metal Batteries. *Advanced Energy Materials* **2017**, 7 (22).
137. Inaguma, Y.; Liquan, C.; Itoh, M.; Nakamura, T.; Uchida, T.; Ikuta, H.; Wakihara, M., High ionic conductivity in lithium lanthanum titanate. *Solid State Communications* **1993**, 86 (10), 689-693.
138. Yang, T.; Zheng, J.; Cheng, Q.; Hu, Y.-Y.; Chan, C. K., Composite Polymer Electrolytes with Li<sub>7</sub>La<sub>3</sub>Zr<sub>2</sub>O<sub>12</sub> Garnet-Type Nanowires as Ceramic Fillers: Mechanism of Conductivity Enhancement and Role of Doping and Morphology. *ACS applied materials & interfaces* **2017**, 9 (26), 21773-21780.
139. Du, J.; Bai, Y.; Chu, W.; Qiao, L., Synthesis and performance of proton conducting chitosan/NH<sub>4</sub>Cl electrolyte. *Journal of Polymer Science Part B: Polymer Physics* **2010**, 48 (3), 260-266.
140. Qian, X.; Gu, N.; Cheng, Z.; Yang, X.; Wang, E.; Dong, S., Impedance study of (PEO) 10LiClO<sub>4</sub>–Al<sub>2</sub>O<sub>3</sub> composite polymer electrolyte with blocking electrodes. *Electrochimica acta* **2001**, 46 (12), 1829-1836.
141. Lei, D.; Shi, K.; Ye, H.; Wan, Z.; Wang, Y.; Shen, L.; Li, B.; Yang, Q. H.; Kang, F.; He, Y. B., Progress and Perspective of Solid - State Lithium - Sulfur Batteries. *Advanced Functional Materials* **2018**.

142. Du, H.; Li, S.; Qu, H.; Lu, B.; Wang, X.; Chai, J.; Zhang, H.; Ma, J.; Zhang, Z.; Cui, G., Stable Cycling of Lithium-Sulfur Battery Enabled by a Reliable Gel Polymer Electrolyte Rich in Ester Groups. *Journal of Membrane Science* **2018**.
143. Fu, K. K.; Gong, Y.; Hitz, G. T.; McOwen, D. W.; Li, Y.; Xu, S.; Wen, Y.; Zhang, L.; Wang, C.; Pastel, G., Three-dimensional bilayer garnet solid electrolyte based high energy density lithium metal-sulfur batteries. *Energy & Environmental Science* **2017**, *10* (7), 1568-1575.
144. Hakari, T.; Hayashi, A.; Tatsumisago, M., Highly utilized lithium sulfide active material by enhancing conductivity in all-solid-state batteries. *Chemistry Letters* **2015**, *44* (12), 1664-1666.
145. Lin, Z.; Liu, Z.; Dudney, N. J.; Liang, C., Lithium superionic sulfide cathode for all-solid lithium-sulfur batteries. *Acs Nano* **2013**, *7* (3), 2829-2833.
146. Lin, Z.; Liu, Z.; Fu, W.; Dudney, N. J.; Liang, C., Lithium Polysulfidophosphates: A Family of Lithium - Conducting Sulfur - Rich Compounds for Lithium - Sulfur Batteries. *Angewandte Chemie* **2013**, *125* (29), 7608-7611.
147. Oh, D. Y.; Kim, D. H.; Jung, S. H.; Han, J.-G.; Choi, N.-S.; Jung, Y. S., Single-step wet-chemical fabrication of sheet-type electrodes from solid-electrolyte precursors for all-solid-state lithium-ion batteries. *Journal of Materials Chemistry A* **2017**, *5* (39), 20771-20779.
148. Xu, R.-c.; Xia, X.-h.; Wang, X.-l.; Xia, Y.; Tu, J.-p., Tailored Li<sub>2</sub>S-P<sub>2</sub>S<sub>5</sub> glass-ceramic electrolyte by MoS<sub>2</sub> doping, possessing high ionic conductivity for all-solid-state lithium-sulfur batteries. *Journal of Materials Chemistry A* **2017**, *5* (6), 2829-2834.
149. Zhu, P.; Zhu, J.; Yan, C.; Dirican, M.; Zang, J.; Jia, H.; Li, Y.; Kiyak, Y.; Tan, H.; Zhang, X., In Situ Polymerization of Nanostructured Conductive Polymer on 3D Sulfur/Carbon Nanofiber Composite Network as Cathode for High - Performance Lithium-Sulfur Batteries. *Advanced Materials Interfaces* **2018**.

150. Zhu, P.; Yan, C.; Dirican, M.; Zhu, J.; Zang, J.; Selvan, R. K.; Chung, C.-C.; Jia, H.; Li, Y.; Kiyak, Y., Li<sub>0.33</sub>La<sub>0.557</sub>TiO<sub>3</sub> ceramic nanofiber-enhanced polyethylene oxide-based composite polymer electrolytes for all-solid-state lithium batteries. *Journal of Materials Chemistry A* **2018**, *6* (10), 4279-4285.
151. Ding, F.; Xu, W.; Graff, G. L.; Zhang, J.; Sushko, M. L.; Chen, X.; Shao, Y.; Engelhard, M. H.; Nie, Z.; Xiao, J., Dendrite-free lithium deposition via self-healing electrostatic shield mechanism. *Journal of the American Chemical Society* **2013**, *135* (11), 4450-4456.
152. Zeng, X.-X.; Yin, Y.-X.; Li, N.-W.; Du, W.-C.; Guo, Y.-G.; Wan, L.-J., Reshaping lithium plating/stripping behavior via bifunctional polymer electrolyte for room-temperature solid Li metal batteries. *Journal of the American Chemical Society* **2016**, *138* (49), 15825-15828.
153. Judez, X.; Zhang, H.; Li, C.; Eshetu, G. G.; Zhang, Y.; González-Marcos, J. A.; Armand, M.; Rodriguez-Martinez, L. M., Polymer-Rich Composite Electrolytes for All-Solid-State Li-S Cells. *The Journal of Physical Chemistry Letters* **2017**, *8* (15), 3473-3477.
154. Zhu, Y.; Li, J.; Liu, J., A bifunctional ion-electron conducting interlayer for high energy density all-solid-state lithium-sulfur battery. *Journal of Power Sources* **2017**, *351*, 17-25.
155. Chen, L.; Connell, J. G.; Nie, A.; Huang, Z.; Zavadil, K. R.; Klavetter, K. C.; Yuan, Y.; Sharifi-Asl, S.; Shahbazian-Yassar, R.; Libera, J. A., Lithium metal protected by atomic layer deposition metal oxide for high performance anodes. *Journal of Materials Chemistry A* **2017**, *5* (24), 12297-12309.